ADDITIVE MANUFACTURING OF GREEN SYNTHESIZED NANOPARTICLES FOR BIOLOGICAL AND ELECTROCHEMICAL APPLICATIONS

by

SERRA ERSOY

Submitted to the Graduate School of Engineering and Natural Sciences

in partial fulfillment of the requirements for the degree of Master of Science

Sabanci University

December 2024

© Serra Ersoy 2024

All Rights Reserved

ABSTRACT

ADDITIVE MANUFACTURING OF GREEN SYNTHESIZED NANOPARTICLES FOR BIOLOGICAL AND ELECTROCHEMICAL APPLICATIONS

SERRA ERSOY

MATERIALS SCIENCE AND NANO ENGINEERING, MSC. THESIS, DECEMBER 2024

Thesis Supervisor: Prof. Dr. Bahattin KOÇ

Co-Advisor: Prof. Dr. Cengiz KAYA

Keywords: Green Synthesis, Hyperthermia, Micro-supercapacitor, 3D Printing, Sustainable Productions

Green synthesis has become quite widespread in recent years due to its sustainability, cost-effectiveness, and environmental friendliness compared to traditional physical and chemical production methods. Previous studies have focused on the antibacterial and antitoxic properties of nanoparticles produced from plant extracts, but their integration into biological and electrochemical applications through controlled material manufacturing has never been investigated. For this reason, this thesis study aimed to produce controlled nanoparticles and materials for specific applications using two sustainable methods like green synthesis and

additive manufacturing. First, silver, gold, titanium dioxide, zinc oxide, and iron oxide nanoparticles were produced from waste broccoli extracts using the green synthesis method. Secondly, the hyperthermia application of kirigami meta-structured hydrogels additively manufactured from N-isopropylacrylamide, polyethylene glycol, gold nanoflowers, polydopamine, and rose bengal photo-initiators using a micro-stereolithography process for photothermal therapy. The developed structures were demonstrated, and the physicochemical, thermal, morphological, and biological behaviors of hydrogels were examined. Lastly, a sustainable, flexible, quasi-solid-state micro-supercapacitor was developed using a direct ink-writing process. The conductive ink was made from zinc oxide nanoparticles and calcined broccoli waste, with polyvinyl alcohol/potassium hydroxide serving as the electrolyte. In this thesis, it has been shown that nanoparticles produced by green synthesis using two different additive manufacturing processes can provide environmentally friendly and sustainable results not only for biological but also thermal and electrical applications, compared to traditional methods.

ÖZET

BİYOLOJİK VE ELEKTROKİMYASAL UYGULAMALAR İÇİN YEŞİL SENTEZLENEN NANOPARTİKÜLLERİN KATMANLI ÜRETİMİ

SERRA ERSOY

MALZEME BİLİMİ VE NANO MÜHENDİSLİK, YÜKSEK LİSANS TEZİ, ARALIK 2024

Tez Danışmanı: Prof. Dr. Bahattin KOÇ

Eş-Danışman: Prof. Dr. Cengiz KAYA

Anahtar Kelimeler: Yeşil Sentez, Hipertermi, Mikro-süperkapasitör, 3 Boyutlu Basım, Sürdürülebilir Üretimler

Yeşil sentez; geleneksel fiziksel ve kimyasal nanopartikül üretim yöntemlerine kıyasla sürdürülebilirliği, maliyet etkinliği ve çevre dostu olması nedeniyle son yıllarda oldukça yaygınlaşmıştır. Önceki çalışmalar bitki özlerinden üretilen nanopartiküllerin antibakteriyel ve antitoksik özelliklerine odaklanmış, ancak kontrollü malzeme üretimi yoluyla biyolojik ve elektrokimyasal uygulamalara entegrasyonu araştırılmamıştır. Bu nedenle, bu tez çalışması yeşil sentez ve eklemeli imalat gibi iki sürdürülebilir yöntemle belirtilen uygulamalar için kontrollü nanopartiküller ve malzemeler üretmeyi amaçlamıştır. İlk olarak; atık brokoli özütüyle yeşil sentez yöntemi kullanılarak gümüş, altın, titanyum dioksit, çinko oksit ve demir oksit nanopartiküllerinin üretimi ve karakterizasyonları

geliştirilmiştir. İkinci olarak; fototermal terapi için N-izopropilakrilamid, polietilen glikol, altın nanoçiçekler, polidopamin ve rose bengal foto-başlatıcılarından yapılan kirigami meta-yapılı hidrojellerin hipertermi uygulaması, bir mikro-stereolitografi üç boyutlu (3B) yazıcı kullanılarak gösterilmiş ve beş farklı bileşime sahip hidrojellerin fizikokimyasal, termal, morfolojik ve biyolojik davranışları incelenmiştir. Son olarak; polivinil alkol/potasyum hidroksit elektrolit ve bir pamuklu kumaş alt tabaka kullanılarak çinko oksit nanopartiküllerinden ve kalsine edilmiş atık brokoliden elde edilen sürdürülebilir elektrot, ekstrüzyon tabanlı bir 3B yazıcı ile simetrik, esnek, yarı katı hal mikro süperkapasitöre dönüştürülmüştür. Bu tezde, iki farklı eklemeli imalat yöntemleri kullanılarak yeşil sentezle üretilen nanopartiküllerin yalnızca biyolojik değil aynı zamanda termal ve elektriksel uygulamalar için de geleneksel yöntemlere kıyasla daha çevre dostu ve sürdürülebilir sonuçlar sağlayabileceği gösterilmiştir.

ACKNOWLEDGEMENTS

I consider myself incredibly fortunate to have graduated from this university, where I was able to stretch my boundaries both personally and academically.

First of all, I would like to thank my supervisor and co-advisor, Prof. Dr. Bahattin Koç and Prof. Dr. Cengiz Kaya, for always supporting me and allowing me to improve myself. I am appreciative of Prof. Dr. Metin Sitti and his team, especially Dr. Erdost Yıldız for sharing his academic experiences and spending time on my thesis (Chapter 2 and 3) at Max Planck Institute for Intelligent Systems in Stuttgart, Germany. I am grateful to Dr. Simon Fleischmann and his team at Helmholtz Institute Ulm (HIU), where I learned how to interpret electrochemical analyses and prepare a slurry for my thesis (Chapter 4). Additionally, I would want to thank Koç Lab team members and YTU Nanolab team members which are Prof. Dr. Figen Kaya, Assoc. Prof. Suna Avcıoğlu, Assoc. Prof. Ali Can Zaman, Dr. Mücahid Özcan and Vecihe Elif Imamoğlu for teaching me what they know about the subject I am working on. Moreover, I am grateful to my jury members, Prof. Dr. Yusuf Ziya Menceloğlu, Prof. Dr. Emre Erdem and Asst. Prof. Dr. Hakan Yılmazer for their interest in my thesis and valuable comments.

Last but not least, I would like to thank my lovely family, who have always believed in me and supported me on this long academic journey. I am especially grateful to my mother, Seray Ersoy, for constantly drying the kilos of broccoli I used in the experiments. I extend my heartfelt appreciation to my lovely friends Gülşen Zal, Rabia Mercimek, Gökmen Tamer Şanlı, Zobia Batool, Ayça Aydurmuş and Seba Nur Alhasan for all unforgettable, precious memories and always being there for me. Thank you to all people who motivated me and helped me get back on track when I was psychologically tired and gave up.

I am pleased to TUBITAK for the scholarship and research partially funding they have extended to me. (Project No: 221M539)

Her zaman beni destekleyen

sevgili annem, babam ve kız kardeşime…

TABLE OF CONTENTS

LIST OF FIGURES xiv

LIST OF TABLES xviii

LIST OF ABBREVIATIONS xix

LIST OF SYMBOLS xxi

1. CHAPTER 1: INTRODUCTION.....24

1.1. Aim and Novelty of Thesis 24

2. CHAPTER 2: GREEN SYNTHESIS OF NANOPARTICLES 26

2.1. Introduction.....26

2.1.1. Nanomaterials.....27

2.1.2. Production Techniques of Nanomaterials 28

2.1.2.1. Top-down approach 29

2.1.2.2. Bottom-up approach.....29

2.1.3. Green Synthesis 30

2.1.3.1. Silver nanoparticles.....33

2.1.3.2. Gold nanoparticles 34

2.1.3.3. Zinc oxide nanoparticles 34

2.1.3.4. Titanium dioxide nanoparticles.....35

2.1.3.5. Iron oxide nanoparticles.....36

2.2. Materials and Method 38

2.2.1. Materials.....38

2.2.2. Green Synthesis of Transition Metal/Metal Oxide Nanoparticles 39

2.2.3. Characterizations of Nanoparticles.....43

2.3. Results and Discussion 46

2.4. Conclusions and Future Works 60

3. CHAPTER 3: 3D PRINTING OF GREEN SYNTHESIZED NANOPARTICLES FOR HYPERTHERMIA APPLICATIONS.....62

3.1. Introduction 62
3.1.1. Cancer Treatments 63
3.1.2. Photothermal Therapy 64
3.1.3. Hyperthermia Ink Components 65
3.1.3.1. Gold nanoflowers 65
3.1.3.2. Polydopamine 66
3.1.3.3. Rose Bengal 67
3.1.3.4. NIPAM 67
3.1.4. 3D Printing of Hydrogels 69
3.1.4.1. Types of 3D printer 69
3.1.4.2. Microstereolithography (μSLA) printer 70
3.1.4.3. Photopolymerization 70
3.1.4.4. Design of hydrogels 71
3.2. Materials and Method 73
3.2.1. Materials 73
3.2.2. Synthesis of LIHAM 73
3.2.3. Conjugated of Gold Nanoflowers@Polydopamine with Rose Bengal 74
3.2.4. Printing of LIHAM 75
3.2.5. Characterization of Kirigami Meta Structure Hydrogels 78
3.3. Results and Discussion 83
3.3.1. Physicochemical Characterizations 83
3.3.1.1. Rheological measurements 84
3.3.1.2. Osmotic swelling response 89
3.3.1.3. FTIR 90
3.3.1.4. Enzymatic degradation 93
3.3.2. Structural/Morphological Characterizations 95
3.3.2.1. SEM and TEM 95

3.3.3. Thermal Characterizations....96
3.3.3.1. DSC....96
3.3.3.2. Hyperthermia analysis....98
3.3.4. In Vitro Characterization....101
3.3.4.1. Luciferase-based cytotoxicity assay....101
3.4. Conclusions and Future Works....106
4. CHAPTER 4: 3D DIRECT-INK WRITING OF GREEN SYNTHESIZED NANOPARTICLES FOR MICRO-SUPERCAPACITORS....108
4.1. Introduction....108
4.1.1. Micro-Supercapacitors....109
4.1.2. Mechanism of Micro-Supercapacitor....109
4.1.3. Types and Materials of Micro-Supecapacitors....110
4.1.3.1. Electrodes....111
4.1.3.2. Electrolytes....113
4.1.3.3. Current collectors....114
4.1.4. Additive Manufacturing for Micro-Supercapacitors....115
4.1.4.1. Extrusion based 3D printing....116
4.1.4.2. 3D Printing parameters....117
4.1.4.3. Post-treatments....118
4.1.5. Micro-Supercapacitor Ink Ingredients....119
4.1.5.1. Green synthesized ZnO nanoparticles as an active material....119
4.1.5.2. Broccoli extract and dried broccoli as a carbon content....120
4.1.5.3. Carboxylmethyl cellulose (CMC) as a natural binder....120
4.1.5.4. PDMS for encapsulation....121
4.2. Materials and Method....122
4.2.1. Materials....122
4.2.2. Producing extracts from broccoli....122

4.2.3. Synthesis of ZnO NPs with the help of Broccoli Extract 123
4.2.4. Calcination of Dried Broccoli 123
4.2.5. Electrode Preparation 124
4.2.6. Preparation of Electrolyte 126
4.2.7. Symmetric Micro-Supercapacitor Architecture 127
4.2.8. Printing of Flexible Micro-Supercapacitor Wearable Devices and Post-treatments 128
4.2.9. Characterizations 129
4.3. Results and Discussion 134
4.3.1. Characterizations of ZnO Nanoparticles 134
4.3.2. Characterizations of Broccoli Extract and Biowaste Calcinated Broccoli 138
4.3.3. Characterizations of Inks 147
4.3.4. Characterizations of Flexible Micro-Supercapacitor Devices 149
4.4. Conclusions and Future Works 153
5. CHAPTER 5: CONCLUSIONS 156
5.1. Conclusions of Thesis 156
6. REFERENCES 160

LIST OF FIGURES

Figure 1: Schematic representation of biological and electrochemical applications developed with green synthesis and additive manufacturing in the thesis [BioRender]. 25
Figure 2: Classifications of nanomaterials (Ahire et al., 2022) [BioRender]. 28
Figure 3: Approaches and methods of nanoparticles (Ahire et al., 2022, Galstyan et al., 2018) [BioRender]. 29
Figure 4: Synthesis steps of broccoli extract (Ersoy et al., 2024) [BioRender]. ..39
Figure 5: Diagrammatic illustration of the synthesis of metal/metal oxide nanoparticles [BioRender]. 42
Figure 6: Conjugation steps of all synthesized nanoparticles with PDA (Ersoy et al., 2024) [BioRender]. 43
Figure 7: Bioreduction and characterizations of various NPs [BioRender]. 46
Figure 8: Characterizations of AgNPs: **a** XRD analysis; **b** SEM analysis at 10 and 1 micrometers with an EDS analysis table; **c** FTIR graph between 4000 and 500 cm^{-1}; **d** UV-visible spectrophotometer graph between 250 and 600 nm; **e** TEM image at 50 nm scale and particles size are approximately 37 nm; **f** VSM analysis data from magnetization (emu)/ H (Oe) graph; **g** luciferase-based cytotoxicity assay results according to the concentration; and **h** hyperthermia analysis results at 470 nm (blue-violet) light for AgNPs and AgNPs@PDA after 20 min [BioRender]. 47
Figure 9: Characterizastions of AuNPs: **a** XRD analysis; **b** SEM analysis at 10 and 1 micrometer with EDS analysis table; **c** FTIR graph between 4000 and 500 cm^{-1}; **d** UV-visible spectrophotometer graph between 250 and 600 nm for 4 and 1 mM gold nanoparticles; **e** TEM image at 50 nm scale and particles size are approximately 100 nm; **f** VSM analysis data from magnetization (emu)/ H (Oe) graph; **g** luciferase-based cytotoxicity assay results according to the concentration of gold nanoparticles with non-coated PDA; and **h** hyperthermia analysis results at 470 nm for 1 and 4 mM Au NPs and (4 mM) AuNPs@PDA (blue-violet) light after 20 min (Ersoy et al., 2024) [BioRender]. 49
Figure 10: Charahterizations of ZnO NPs: **a** XRD analysis; **b** SEM analysis of zinc nitrate (0.1M) NPs; zinc acetate (0.1M) NPs; and zinc acetate (1M) NPs at 10 and 1 micrometer with EDS analysis table respectively; **c** FTIR graph between 4000 and 500 cm^{-1}; **d** UV-visible spectrophotometer graph between 300 and 600 nm for 0.1, 1 M Zinc acetate and 0.1 M Zinc Nitrate NPs; **e** TEM image at 50 nm scale and particles size are approximately 25 nm; **f** VSM analysis data from magnetization (emu)/ H (Oe) graph; **g** luciferase-based cytotoxicity assay results according to the concentration of ZnO NPs with non-coated PDA; and **h** hyperthermia analysis results at 470 nm for ZnO NPs and NPs@PDA (blue-violet) light after 20 min [BioRender]. 52
Figure 11: Characterizations of TiO_2 NPs: **a** XRD analysis; **b** SEM analysis of TiO_2 NPs at 10 and 1 micrometer with EDS analysis table; **c** FTIR graph between 4000 and 500 cm^{-1}; **d** UV-visible spectrophotometer graph between 250 and 600 nm; **e** TEM image at 50 nm scale and particles size are approximately 13 nm; **f** VSM analysis data from magnetization (emu)/ H (Oe) graph; **g** luciferase-based cytotoxicity assay results according to the concentration of titanium dioxide nanoparticles with non-coated PDA; and **h** hyperthermia analysis results at 470 nm (blue-violet) light for TiO_2 NPs and TiO_2NPs@PDA after 20 min [BioRender]. 54

Figure 12: Characterizations of FeO NPs. **a** XRD analysis; **b** SEM analysis of iron oxide NPs at 10 and 1 micrometer with EDS analysis table; **c** FTIR graph between 4000 and 500 cm^{-1}, **d** UV-visible spectrophotometer graph between 250 and 600 nm; **e** TEM image at 500 nm scale and particles size are approximately 3.5 micrometer; **f** VSM analysis data from magnetization (emu)/ H (Oe) graph; **g** luciferase-based cytotoxicity assay results according to the concentration of iron oxide nanoparticles with non-coated PDA; and **h** hyperthermia analysis results at 470 nm (blue-violet) light for iron oxide NPs and iron NPs@PDA after 20 min [BioRender]. 56
Figure 13: Printing stage of kirigami meta-structure design with PμSL 3D printer (Ersoy et al., 2024) [BioRender].....72
Figure 14: a Synthesis steps of LIHAM solutions and **b** Experimental steps of conjugated AuNPs@PDA with RB [BioRender] (Ersoy et al., 2024).....75
Figure 15: Photo-polymerization steps of hydrogels [BioRender] (Ersoy et al., 2024).....75
Figure 16: LIHAM kirigami hydrogels according to the printer time and intensity parameters for Exp.2 **a**, Exp.3 **b**, Exp.4 **c**, and Exp.5 **d** at RT. Furthermore, LIHAM hydrogels images according to the solution parameters after printing with CELLINK and Volumetric introduce Lumen X 3D bioprinter to Exp.a for 10 seconds **e**, Exp.a for 20 seconds **f,** Exp.b for 20 seconds **g**, Exp.c for 20 seconds **h**, Exp.d for 20 seconds **i**, and Exp.e for 20 seconds **j** at RT [BioRender]. 76
Figure 17: Five different hydrogels according to the photoinitiators [BioRender] (Ersoy et al., 2024).....78
Figure 18: Rheology analyses for compression test [BioRender] (Ersoy et al., 2024).....79
Figure 19: Oscillation strain values of the hydrogels before examining the viscoelastic behaviors [BioRender] (Ersoy et al., 2024). 80
Figure 20: Stress/Strain curve for five different hydrogels (Ersoy et al., 2024)...84
Figure 21: Young's modulus curves for five different hydrogels stress/strain curve diagrams with blue lines (datas from the analysis) and orange lines (linear fits) (Ersoy et al., 2024).....85
Figure 22: Angular frequency sweep of hydrogels **a** LIHAM, **b** LIHAM@AuNPs, **c** LIHAM@AuNPs@PDA, **d** LIHAM@AuNPs@RB, **e** LIHAM@AuNPs@PDA@RB, and **f** table of storage modulus (G′) of different hydrogels at 10^1 (rad/s) (Ersoy et al., 2024). 87
Figure 23: Temperature sweep analysis of hydrogels **a** LIHAM, **b** LIHAM@AuNPs, **c** LIHAM@AuNPs@PDA, **d** LIHAM@AuNPs@RB, **e** LIHAM@AuNPs@PDA@RB, and **f** table of storage modulus (G1) of different hydrogels at 20° C (Ersoy et al., 2024). 88
Figure 24: Osmotic swelling response of five different LIHAM hydrogels after inside DW for five days and calculations of $M_{swelling}$, M_{dried}, and Q_w values (Ersoy et al., 2024) [BioRender]. 89
Figure 25: Graphic of swelling degree for each hydrogel according to the additives (Ersoy et al., 2024). 90
Figure 26: FTIR analysis of hydrogels between 500-4000 cm^{-1} (Ersoy et al., 2024).....91
Figure 27: FTIR peaks for chemicals which used for producing LIHAM solution in the band range of 4000-500 cm^{-1} (Ersoy et al., 2024) [BioRender]. 93
Figure 28: Enzymatic degradation analysis for each hydrogel [BioRender].....93

Figure 29: Enzymatic degradation rate percentage of hydrogels for 260 minutes [BioRender]. 94
Figure 30: SEM of LIHAM hydrogel image at 10 μm and TEM of LIHAM hydrogel image at 1 μm, SEM of LIHAM@AuNPs hydrogel image at 10 μm and TEM of LIHAM@AuNPs hydrogel image at 0.5 μm, SEM of LIHAM@AuNPs@RB hydrogel image at 10 μm and TEM of LIHAM@AuNPs@RB hydrogel image at 1 μm, SEM of LIHAM@AuNPs@PDA hydrogel image at 10 μm and TEM of LIHAM@AuNPs@PDA hydrogel image at 1 μm, SEM of LIHAM@AuNPs@PDA@RB hydrogel image at 10 μm and SEM of kirigami shape of LIHAM hydrogel image at 100 μm (Ersoy et al., 2024) [BioRender]. 95
Figure 31: DSC analysis of five different hydrogels and Tg values of these hydrogels: **a** LIHAM, **b** LIHAM@AuNPs, **c** LIHAM@AuNPs@RB, **d** LIHAM@AuNPs@PDA, and **e** LIHAM@AuNPs@PDA@RB (Ersoy et al., 2024) [BioRender]. 97
Figure 32: a Hyperthermia analysis of five different hydrogels at a 565 nm (yellow laser) light source which is the best light for AuNPs, RB, and PDA to increase the temperature and cm scale of length of hydrogels at the beginning, after 565 nm light for 20 minutes and after heater for 20 minutes respectively. **b** Temperature degrees of AuNPs, RB, and PDA photosensitizer after 20 minutes at three different visible light sources (470 nm (blue), 565 nm (yellowish green) and 625 nm (red)). **c** Length of five different hydrogels at the beginning, at 565 nm and heater respectively (Ersoy et al., 2024) [BioRender]. 99
Figure 33: Cell viability percentage graph of hydrogels as a result of luciferase-based cytotoxicity assay (Ersoy et al., 2024). 101
Figure 34: Microscopic images of the hydrogels after they were printed and kept in the refrigerator at +4° C for 3 weeks (Ersoy et al., 2024) [BioRender]. 106
Figure 35: Briefly, the results of the second part and the inspiring LIHAM@AuNPs@PDA@RB hydrogel that can be used in future studies (Ersoy et al., 2024) [BioRender]. 107
Figure 36: Supercapacitor types and required materials: **a** Sandwich type supercapacitor and, **b** in-plane supercapacitors (Vandeginste, 2022) [BioRender]. 111
Figure 37: Production of ZnO NPs and broccoli carbon powders [BioRender]. 124
Figure 38: Three-electrode system analysis, ink preparation and ink printing steps: **a** Preparation of slurry using PVDF and NMP to coat ZnO NPs and B400 powders onto nickel foams and electrochemical analysis in the three-electrode system, **b** preparation of electrode ink using ZnO NPs, B400 and CMC for printing and preparation of gel polymer electrolyte, and **c** printing of the ink prepared with an extrusion-based 3D printer on 100% cotton fabric according to the design [BioRender]. 127
Figure 39: Micro-supercapacitor designs and steps to convert the file into G-code in a suitable format for Aerotech CNC based 3D printer [BioRender]. 128
Figure 40: ZnO NPs characterizations: **a** SEM, TEM and EDS analyses at different magnifications, **b** XRD analysis in the (20-80) 2θ range, **c** FTIR analysis in the 4000-600 cm^{-1} band gap and **d** TG/DTA analysis showing mass loss with temperature [BioRender].. 134

Figure 41: Electrochemical analysis of ZnO NPs powder in a three-electrode system: **a** EIS, **b** CV at different scan rates in the 0-0.6 voltage range, **c** GCD plots at 0.5, 1, 2, and 4 A/g current density values, and **d** specific capacitance values calculated from the CV plot [BioRender]. 136
Figure 42: Morphological and chemical analyses of broccoli powders and BE calcined at different temperatures: **a** SEM and EDS analysis for four different powders, **b** XRD analysis of dried broccoli, B300, B375 and B400 powders in the 2θ: 20-80 range, **c** FTIR analysis of BE in the 4000-600 cm^{-1} band range, **d** FTIR analysis of calcined and non-calcined broccoli powders, **e** Raman analyses of powders, and **f** TG/DTA analysis of dried and non-calcined broccoli powder [BioRender]. 139
Figure 43: Electrochemical analysis of B400 powder in a three-electrode system: **a** EIS, **b** CV analysis at different scan rates in the voltage range of 0-0.6, **c** CV analysis at different scan rates in the voltage range of -0.6-0, **d** comparison of CV graphs at 10 mV/s scan rate in the positive and negative regions, **e** specific capacitance values calculated from CV graphs in different regions, and **f** GCD graphs at current densities of 0.5, 1, 2, and 4 A/g [BioRender]. 142
Figure 44: Electrochemical analysis results of nickel foams prepared and coated by adding B400 powder instead of conductive carbon black during the slurry preparation of ZnO NPs powder in the three-electrode system: **a** EIS comparison of ZnO and ZnO/B400 powders, **b** CV analysis of ZnO/B400 powder in the 0-0.6 voltage range at different scan rates, **c** CV comparison of ZnO and ZnO/B400 powders at 10 mV/s scan rate, **d** comparison of specific capacitance values of ZnO and ZnO/B400 powder, **e** GCD analysis at different current density values, and **f** calculation of efficiency according to specific capacitance values between 50-500 cycles [BioRender]. 143
Figure 45: Electrochemical analyses of symmetric and asymmetric devices with ZnO NPs in two-electrode system: **a** EIS analyses of asymmetric devices made with B300, B375 and B400 powders, **b** %capacity retention values of asymmetric devices with ZnO NPs in broccoli powder calcined at different temperatures, and **c** CV analysis of ZnO/B400 asymmetric device at different scan rate values and comparison of CV analysis of three different devices at 10 mV/s scan rate [BioRender]. 145
Figure 46: Concentration adjustment and characterization of the inks used in 3D printing: **a** FTIR analysis of three different inks prepared with 0.16 g of B400 and ZnO NPs powders in CMC solution at 4000-600 cm^{-1}, **b** FTIR analysis of inks prepared by adding the same amount of B400 and ZnO NPs powders in 0.16, 0.20 and 0.24 g of CMC solutions, **c** FTIR analysis of CMC concentration difference, **d** FTIR analysis of PVA/KOH electrolyte, **e** viscosity and rheological analysis of B400 and ZnO NPs powders, and **f** hydrophobic/hydrophilic properties of inks dropped onto different substrates and flexibility and dimensional analysis of printed micro-supercapacitors [BioRender]. 148
Figure 47: Electrochemical measurement trials of the MSC device: **a** taking the measurement of the printed MSC device in the two-electrode system, **b** EIS analysis result for the MSC device and circuit drawing with fitting of the result, **c** CV analysis between 0-1 V at different scan rates, and **d** GCD analysis between 0-0.6 V at different current density values [BioRender]. 150

LIST OF TABLES

Table 1: Printer exposure times and intensity of light changing of printing parameters for finding the best meta structure. 76
Table 2: Changing solution ingredients like photo-initiator and monomers for finding the best ratio to the printing of hydrogels (X= times). 77
Table 3: Comparison of electrochemical advantages and disadvantages of carbon, metal oxide and composite electrodes (Kamal K. Kar, 2023). 112
Table 4: Ink contents and material codes at six different concentrations for rheological analysis. 125
Table 5: BET analysis results for B300, B375 and B400 powders. 138
Table 6: Specific capacitance, energy and power density values calculated from GCD graphs according to current density values for powders. 146

LIST OF ABBREVIATIONS

µSLA	Micro Stereolithography
0D	Zero Dimensional
1D	One Dimensional
2D	Two Dimensional
3D	Three Dimensional
3DP	Three Dimensional Printing
AgNPs	Silver Nanoparticles
AM	Additive Manufacturing
AuNPs	Gold Nanoparticles
BE	Broccoli Extract
CAD	Computer Aided Design
CE	Counter Electrode
CMC	Carboxymethyl Cellulose
CNC	Computer Numerical Control
Csp	Specific Capacitance
CV	Cyclic Voltammetry
DIW	Direct Ink Writing
DLP	Digital light processing
DW	Distilled Water
Ed	Energy Density
EDLC	Electric Double Layer Capacitor
EIS	Electrochemical Impedance Spectroscopy
EP	Extrusion Printing
FDM	Fused Deposition Modeling
FeO NPs	Iron Oxide Nanoparticles
FFM	Fused Filament Fabrication
GCD	Galvanostatic Charge/Discharge
Hg/HgO	Mercury/Mercury Oxide
iR drop	Ohmic Resistance
KOH	Potassium Hydroxide

LCST	Lower Critical Solution Temperature
LIHAM	Hydrogel
MSCs	Micro-supercapacitors
NIPAM	N-isopropylacrylamide
NIR	Near-Infrared
NMP	N-Methyl-2-pyrrolidone
NPs	Nanoparticles
PμSL	Projection Micro Stereolithography
PC	Pseudocapacitor
Pd	Power Density
PDA	Polydopamine
PDMS	Poly(dimethylsiloxane)
PDT	Photodynamic Therapy
PEG	Polyethylene Glycol
pNIPAM	Poly(N-isopropylacrylamide)
PTT	Photothermal Therapy
PVA	Poly-Vinyl Alcohol
PVDF	Polyvinylidene Difluoride
RB	Rose Bengal
Rct	Charge Transfer Resistance
RE	Reference Electrode
Rs	Electrochemical Resistance
RT	Room Temperature
Rw	Warburg Resistance
SLS	Selective Laser Sintering
STL	Stereolithography
TiO_2 NPs	Titanium Dioxide Nanoparticles
UCST	Upper Critical Solution Temperature
UV	Ultraviolet
WE	Working Electrode
ZnO NPs	Zinc Oxide Nanoparticles

LIST OF SYMBOLS

µl	Microliter
µm	Micrometer
A	Ampere
Å	Angstrom
A/g	Current Density
cm	Centimeter
F	Farad
F/g	Capacitance
g	Gram
h	Hour
J	Joule
kPa	Kilopascal
kV	Kilovolt
kW	Kilowatt
kW/kg	Power Density
M	Molar
mA	Milliampere
meV	Millielectronvolt
mg	Milligram
min	Minute
ml	Milliliter
mm	Millimeter
mM	Millimolar
mmHg	Millimetre of Mercury
mPa	Millipascal
mV	Millivolt
nm	Nanometer
Ø	Diameter
rad	Radius
rpm	Revolutions Per Minute

s	Second
t	Time
V	Volt
W	Watt
Wh/kg	Energy Density
ΔV	Voltage range
η	Coulomb Efficiency
θ	Theta
ω	Angular Frequency
Ω	Ohm

Thesis Structure

This thesis consists of three main chapters. While Chapter 1 highlights the thesis's objective, motivation, and hypothesis, Chapter 5 interprets the thesis's overall conclusions. Chapter 2 includes synthesis and characterizations of different transition metal/metal oxide nanoparticles by the green method with the help of broccoli extract (unpublished work), Chapter 3 contain works of published articles (S. Ersoy *Et Al.* , "Fabrication of Gold Nanoflower-Coated Photosensitive Meta-Structures Using PμSL 3D Printing for Hyperthermia Applications," *ACS Applied Polymer Materials* , vol.6, no.17, pp.10807-10823, 2024. https://pubs.acs.org/doi/10.1021/acsapm.4c01951). Lastly, Chapter 4 involves 3D direct-ink writing of flexible, symmetric, solid-state micro-supercapacitors consisting of zinc oxide nanoparticles synthesized using broccoli extract and calcinated broccoli from waste electrodes with natural binder (preparing for publication).

1. CHAPTER 1: INTRODUCTION

1.1.Aim and Novelty of Thesis

The thesis was motivated by the need to demonstrate that nanoparticles can be employed in biothermal and electrochemical applications while remaining sustainable, waste-recyclable, environmentally benign, and human health-friendly. As an alternative to production methods that use harmful chemicals, consume high amounts of energy, and have toxic effects on the environment and human health, it is aimed to use sustainable production methods such as green synthesis and additive manufacturing methods together. The green synthesis process has received little attention in the literature, and aside from biological analyses, its thermal and electrical properties have never been investigated using additive manufacturing with aqueous broccoli extract solution and waste broccoli. In this thesis, five distinct transition metal nanoparticles were produced utilizing green synthesis, a biological process that uses broccoli (Brassica oleracea var. italica) extract instead of typical physical and chemical toxic and expensive procedures. Chapter 2 provided a detailed characterizations of the produced nanoparticles and optimal nanoparticles were identified for the applications in Chapters 3 and 4. In Chapter 3, gold nanoparticles with the most favorable outcomes from biological and thermal evaluations, as well as photo-thermo-responsive hydrogels, were produced for hyperthermia treatment using additive manufacturing method. In Chapter 4, flexible, symmetric, quasi-solid-state micro-supercapacitor printing was

investigated utilizing direct-ink writing process suing synthesized zinc oxide nanoparticles, and carbon sources derived from biowaste broccoli. Because of its advantages, 3D printers are expected to become more widely used in future studies, such as sustainable, complicated constructions and small-sized device printing. In addition, broccoli extract and waste broccoli has been employed in the green synthesis process because it is easily accessible, has a pH when synthesized, can synthesize nanometer-sized particles, and yields a large amount of last product after drying.

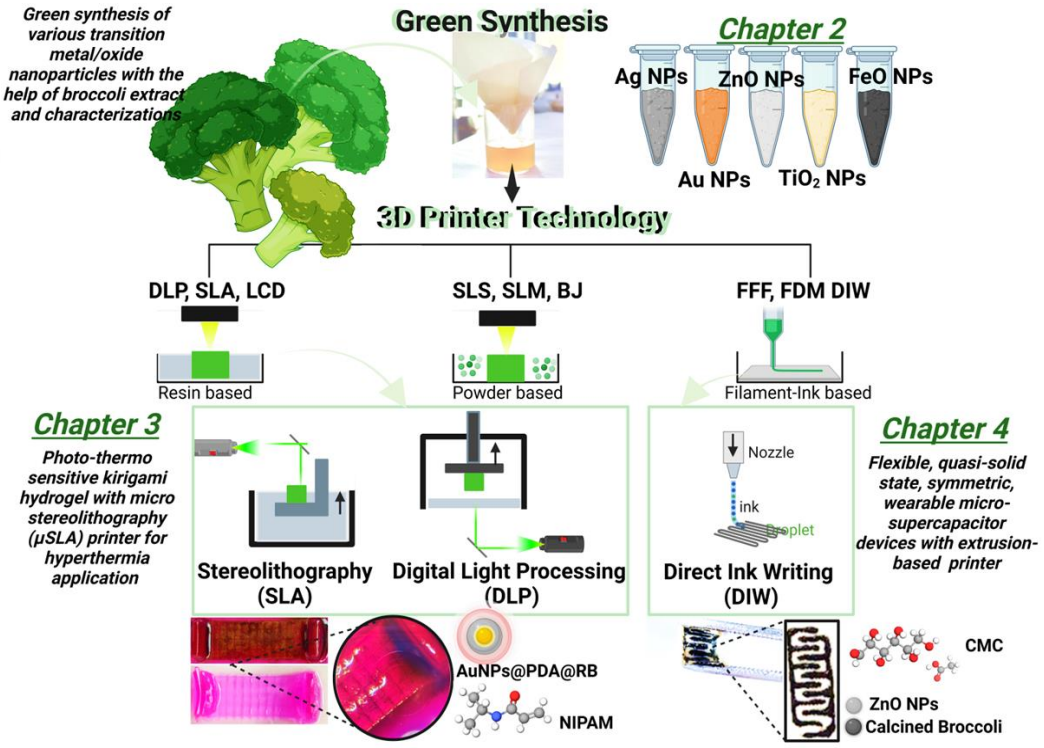


Figure 1: Schematic representation of biological and electrochemical applications developed with green synthesis and additive manufacturing in the thesis [BioRender].

In summary, the purpose of this work is to show that green synthesis is promising, and that additive manufacturing of green synthesized nanoparticles (NPs) for both thermal and electrical applications offer improved properties with low toxicity to the environment and human health. It is believed that particle creation, particularly in nanoscale sizes, can provide advantages in applications by having a high surface to volume ratio. The aim of the thesis, motivation and the studies carried out are explained in detail in *Figure 1*.

2. CHAPTER 2: GREEN SYNTHESIS OF NANOPARTICLES

2.1.Introduction

"Nanotechnology," which started via Richard Feynman with the sentence ‘There's Plenty of Room at the Bottom’ and is now described as the new industrial revolution, has become increasingly widespread due to its innovative and intelligent features in the fields of medicine, pharmacy, electricity, automotive, food, cosmetics, computer, optics, and defense industries (Ahire et al., 2022, H. Levent Keskin, 2011). This field of study looks at how matter that is between 1 and 100 nm in size behaves mechanically, thermally, electrically, optically, and magnetically in technology at a billionth of a meter scale (Ramani et al., 2024). Thanks to nanotechnology, it has become possible to understand analyses and behaviors at the nanoscale, obtain materials with superior properties and production processes, and develop more durable and lightweight materials (H. Levent Keskin, 2011). Because of quantum effects, materials at the nanoscale have entirely distinct properties from those at the macroworld, which is what makes nanomaterials more intriguing than conventional materials (H. Levent Keskin, 2011). Furthermore, a lot of research has been initiated in application areas like targeted drug delivery, health nanorobots, energy storage systems, micro-supercapacitors, environmental remediation, sports equipment, and sensors because of the benefits of being able to place atoms in desired locations, producing nearly anything at the atomic level, and having production costs that are lower than those of raw materials. (Baig et al., 2021, H. Levent Keskin, 2011, Ramani et al., 2024). This thesis discusses the

synthesis of various NPs as well as their use in electrical and biothermal applications. When conducting research using this technology, it is essential to first know nanomaterials.

2.1.1. Nanomaterials

Nanomaterials are materials that have one or more external and internal dimensions or surface structures on the scale of 1-100 nm (Baig et al., 2021). In addition, non-nanoscale groups such as 0D (quantum dots, NPs), 1D (nanofibers, nanotubes, and nanorods), 2D (nanodisks, nanolayers, nanofilms and nanocoating) and 3D (solid materials) are also included in the nanomaterial class (Baig et al., 2021, Bhushan, 2006, Michael F. Ashby, Paulo J. Ferreira and Daniel L. Schodek, 2009). Nanomaterials can be produced from metallic materials, ceramics, polymers and composites (Bhushan, 2006). Nanomaterials can dramatically change their properties below 100 nm due to changes in the surface area/volume ratio (Bhushan, 2006). Considering the bulk and NPs with the same volume, it is known that nanomaterials have a higher surface area to volume ratio due to their high surface area. As the particle size decreases, the surface area to volume ratio increases, and the tendency to enter into chemical reactions also increases (Ahire et al., 2022). As a result, the dangling bonds on the surface provide the nanomaterial with a high surface energy, which causes agglomeration (Ahire et al., 2022). Moreover, aspect ratio is also an important term in the classification of nanomaterials (*Figure 2*). The length of the major axis divided by the width of the minor axis is known as the aspect ratio of a nano-object (Ahire et al., 2022). According to the morphological structure and aspect ratio, materials can also be classified as nanospheres, nanorods, nanofibers, nanowires, nanotubes and nanoflowers (Ahire et al., 2022). Production methods are quite effective in the morphological structures of nanomaterials.

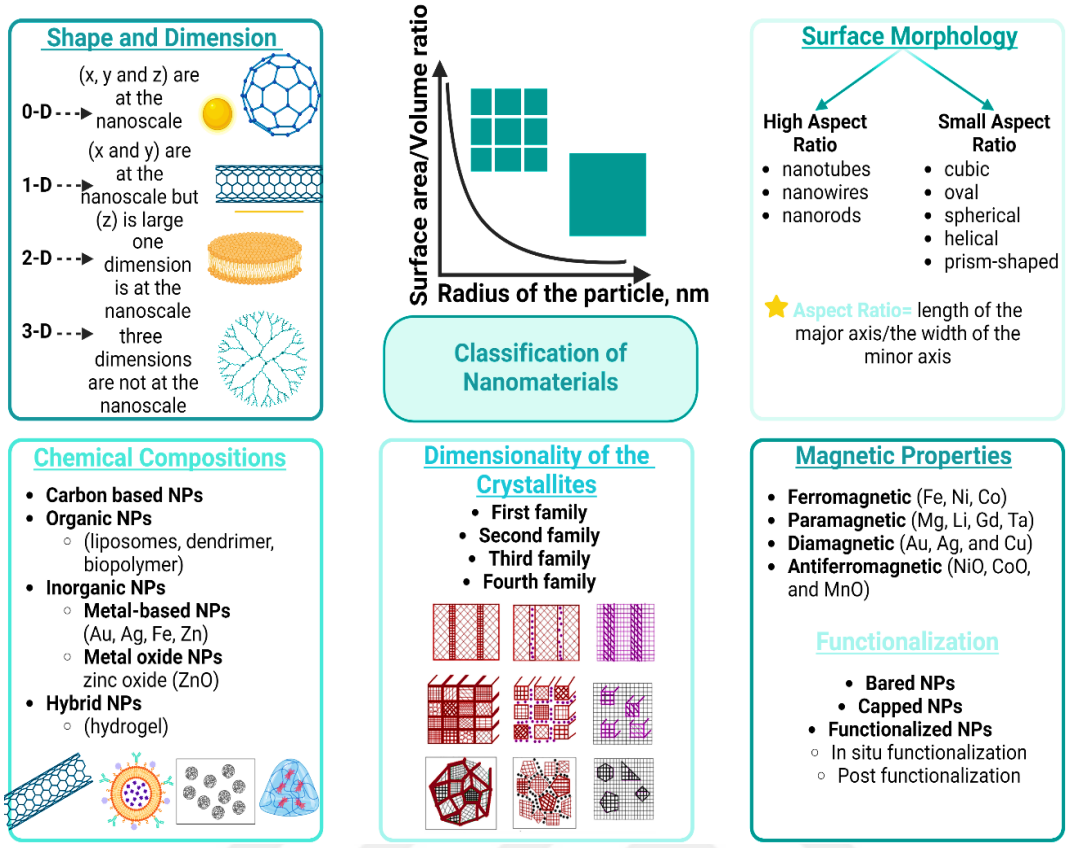


Figure 2: Classifications of nanomaterials (Ahire et al., 2022) [BioRender].

2.1.2. Production Techniques of Nanomaterials

Despite not requiring complicated procedures, the creation of NPs is crucial due to their crucial size, shape, and dimensions. The synthesis, assembly, and sculpting of materials at the nanoscale is known as nanofabrication, and it involves several important prerequisites. For instance, it is preferable to use techniques that are inexpensive, safe for the environment and human health, produce morphologically homogeneous nanomaterials, use minimal energy, and yield a large number of products from a small number of raw ingredients. These manufacturing approaches have both benefits and drawbacks. The two processes for creating nanomaterials are top-down and bottom-up (*Figure 3*) (Ahire et al., 2022, Charitidis et al., 2014, Jamkhande et al., 2019).

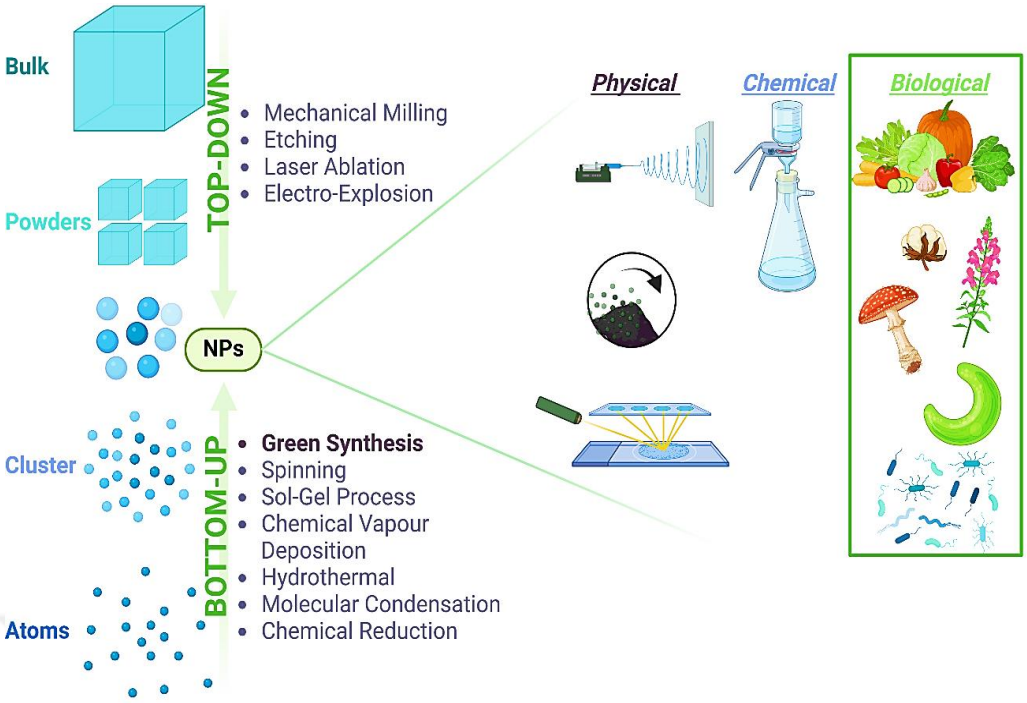


Figure 3: Approaches and methods of nanoparticles (Ahire et al., 2022, Galstyan et al., 2018) [BioRender].

2.1.2.1.Top-down approach

The process is referred to as top-down when the bulk substance breaks down into smaller powders and then breaks down even more to generate NPs. Top-down techniques include lithography, arc discharge, etching, sputtering, laser ablation, electro-explosion, mechanical milling, and physical vapor deposition (Ahire et al., 2022, Baig et al., 2021).

2.1.2.2.Bottom-up approach

Another name for it is the constructive method and this process turns a simpler material into NPs. It is based on the clustering of particles starting from the atom and forming NPs as agglomerations. Bottom-up techniques include chemical vapor deposition, solvothermal and hydrothermal techniques, sol-gel, electrospinning, spray pyrolysis, and green synthesis (Ahire et al., 2022).

Physical, chemical, and biological synthesis are also included in these two approaches. Chemical methods require more chemistry knowledge, such as sol-gel, hydrothermal, chemical-vapor, and micro-emulsion synthesis whereas, physical methods include processes that can be explained by physical approach, such as ball milling, electrospinning, electrospraying, inert gas condensation, melt mixing, and laser pyrolysis (Ahire et al., 2022). Furthermore, utilizing microorganisms like yeast, bacteria, algae, fungi, as well as plant tissues like plant extract, peel, stem, leaves, flowers, vegetables are examples of biological production methods (*Figure 3*) (Ahire et al., 2022). Physical and chemical methods have been used as traditional methods for many years. However, biological methods have become more preferred in recent years due to their advantages (Singh et al., 2016). For instance, because biological approaches are safe, easy, affordable, sustainable, and convenient in terms of energy efficiency, the environment, and the well-being of humans, they are starting to be favored over traditional methods (Ahire et al., 2022). Additionally, the components of plants and microorganisms themselves serve as capping and stabilizing agents, negating the need for additional stabilizing agents (Singh et al., 2016). Green synthesis method is also a type of biological synthesis and the synthesis of all NPs used in this thesis was carried out by this method.

2.1.3. Green Synthesis

The approach of green synthesis mainly encompasses clean chemistry, atom economy, and environmental benign chemistry (Jamkhande et al., 2019). In addition, since no pressure, high temperature, energy or hazardous chemicals are used during the biological process, it is a very economical, environmentally friendly, easy and large-scale production method when was compared with traditional methods (Jamkhande et al., 2019). The environmental contamination brought on by heavy metals limits the utilization of several physiochemical techniques for manufacturing of NPs. Therefore, a new trend in nanoparticle manufacturing is the synthesis of NPs using biological methods with microorganisms and plants (Singh et al., 2016).

The NPs of metal can be synthesized from biological sources through bioreduction and biosorption methods. The *biosorption* is a novel method of NPs production in which metal cations in aqueous media attach to organism cell walls (Jamkhande et al., 2019). On the other hand, *bioreduction* is also the method of creating NPs by chemically reducing metal ions using microorganisms and enzymes (Jamkhande et al., 2019). The plant-mediated production of NPs could be intra- or extracellular. The intracellular approach involves growing the plant in metal-rich organic solutions to synthesize NPs, whereas the extracellular method uses plant extract derived by boiling and crushing the plant in a solvent or aqueous medium (Osuntokun et al., 2019). In this work, the extracellular approach was used to generate NPs from plant extract (Osuntokun et al., 2019).

Despite being monodisperse, bacteria create nanomaterials at a slower rate than plants. Moreover, metallic NPs can be produced using plant extracts, which is a simpler, more cost-effective, environmentally friendly, and reproducible method (Kumar et al., 2023). Also, a comparison study revealed that plants create more stable metal NPs than microorganisms, making them a superior contender for quick and large-scale green synthesis (Kumar et al., 2023). There is a high demand for the use of NPs produced using plants and the universal solvent water with the help of extracts obtained from different parts of plants in the biomedical and energy applications (Singh et al., 2016). Proteins, amino acids, organic acids, vitamins, and secondary metabolites like flavonoids, alkaloids, polyphenols, terpenoids, heterocyclic compounds, and polysaccharides are all play important roles in the reduction of metal salts and serve as capping and stabilizing agents for synthesized NPs when the mechanism of the nanoparticle is investigated using the green synthesis method (Singh et al., 2016). Additionally, plant extracts contain several hydroxyl groups (-OH), biomolecules (carboxy, hydroxy, ortho-dihydroxy, amino, and catechol) (Yontar et al., 2022) and because of these molecules, metal ions are reduced during green synthesis, a metabolic process that requires minimal activation energy (Dhanraj, Rajeshkumar, 2021, Golli et al., 2023, Suppiah et al., 2023). In this way, plants or vegetables that can mediate precursor redox processes, generate metal/metal oxide NPs, and stabilize the resultant NPs (Yontar et al., 2022). Metal ions (M^{+}) are stabilized and reduced to (M^{0}) by plant extract biomolecules like secondary metabolites. In most situations, these metabolites

serve as both stabilizers and reductants (Yontar et al., 2022) which can act as reducing agents to lower the valence of metal ions under optimal conditions (Ying et al., 2022). In summary, the bioreduction of metal NPs from plant extracts consists of three stages. The initial phase involves metal ion reduction and nucleation (Yontar et al., 2022). Small nuclei assemble in the second stage as NPs become more thermodynamically stable (Yontar et al., 2022). Following the growing period, NPs develop their unique shape and centrifugation separates NPs from the solution as a precipitate after their active metabolites reduce the metal ions (Yontar et al., 2022). Moreover, optimization of homogeneous size and morphology can be controlled by parameters such as solution pH, concentration of plant extract, temperature, and mixing ratio during the green synthesis stages (Singh et al., 2016). Changes in pH cause natural phytochemicals in plants to vary in charge, which further impacts their capacity to bind and reduce metal ions during the creation of NPs (Singh et al., 2016). This could therefore have an impact on the yield and shape of the NPs. Plant main and secondary metabolites are continuously involved in redox reactions that occur along plant metabolic pathways (Jamkhande et al., 2019). Several spontaneous reactions occur at normal temperature, resulting in nanosized particles (Jamkhande et al., 2019). In overall, the techniques and processes for green synthesis for different nanoscale metals can be summed up in this order: obtain extract from the plant, mix extract with metal salt solution under specific conditions, reduce metal particles, filter, and proceed to obtain the target nanoscale metal (Ying et al., 2022).

In this thesis study, broccoli was preferred as the plant source for green synthesis. It belongs to the family Brassicaceae (Cruciferae), which has six species, one of which is Brassica oleracea (Golli et al., 2023). It is full of health-promoting nutrients and phytochemicals, such as vitamin C, minerals, soluble sugars, fiber, carotenoids, phenolic compounds which contain hydroxyl groups and flavonoids in broccoli which are rutin, kaempferol, and quercetin (Ganeshpurkar, Saluja, 2017). They have a reputation for being superior free-radical scavengers and metal chelators (Ganeshpurkar, Saluja, 2017). Broccoli has gained a lot of attention in green chemistry for its health-promoting phytochemicals, the capacity of its constituent metabolites to protect the body from damaging free radicals, and its usage as a capping agent in nanoparticle synthesis (Osuntokun et al., 2019). BE is

used quite frequently in biological applications due to its rutin chemical while being used in the green synthesis method (Golli et al., 2023). Moreover, in a study, it was seen that the temperature, pH, time and solvent used while obtaining the extract were effective. According to the results, it was shown that the extract was obtained in 90 minutes, 60% methanol and at a pH value of approximately 8 (V T et al., 2023). Broccoli was also selected for this study because it is readily available, produces a large amount of product when dried during the extraction process, and is used for biomedical applications as well. In this thesis, only the broccoli's waste water was used during NP production. As a result, sustainable products were created by recycling waste food and reusing its water.

2.1.3.1.Silver nanoparticles

Among the most significant noble metal NPs are silver nanoparticles (AgNPs), which have unique structural, plasmonic, and physical features such as surface remodeling as well as selective release of drugs (Golli et al., 2023). The most popular green production method for AgNPs involves combining silver nitrate solution with plant-derived reducing chemicals (Ying et al., 2022). Plant extracts are collected and combined with a solution of silver nitrate and the solution turns brownish as it generates AgNPs (Ying et al., 2022). AgNPs have been studied for their antibacterial capabilities. Furthermore, it has been demonstrated in the literature that different sections of the same plant have distinct effects (Ying et al., 2022). Green-synthesized AgNPs vary in shape and size, with the most prevalent shapes being spherical, triangular, and hexagonal (Ying et al., 2022). AgNPs have been used for many antimicrobial purposes, as well as in anticancer, anti-inflammatory, and wound treatment applications (Singh et al., 2016). Also, AgNPs are employed in a variety of sectors, including electronics, food, textiles, pharmaceuticals, cosmetics, packaging, and biomedicine (Golli et al., 2023). Earlier successes in green AgNP synthesis have involved plants from the apiaceae, asteraceae, solanaceae, zingiberaceae, and brassicaceae families (Golli et al., 2023, Pugazhendhi, 2020). In other research, using BE from silver nitrate raw material, AgNPs were shown to give successful results as an antifungal agent (Golli et al.,

2023). Although the production of AgNPs, especially using BE is quite common in the literature (Abdulazeem et al., 2023, Golli et al., 2023), those studies have focused only on their biological analysis and there is no detailed characterization.

2.1.3.2.Gold nanoparticles

Gold nanoparticles (AuNPs) have received a lot of attention because of their distinctive surface plasmon resonance features, ease of synthesis, variable sizes, adaptable, inert, biocompatible, generally stable, and multifunctional capabilities with well-defined attributes (Santhosh et al., 2022). AuNPs' well-defined surface chemistry allows them to easily conjugate with a variety of molecules, including proteins, dyes, medicines, antibodies, enzymes, and nucleic acids (Santhosh et al., 2022). The usual green synthesis of AuNPs involves reducing gold ions using reducing agents derived from plant extracts or microbes (Ying et al., 2022) and the extracts are then combined with a gold-ion solution, which produces AuNPs when it turns red. AuNPs are easily oxidized by air due to their huge surface area (Ying et al., 2022). Thus, the stability of AuNPs during synthesis and storage is a significant consideration (Ying et al., 2022). AuNPs are widely used especially in biomedical applications, cancer treatment and nanosensor studies (Singh et al., 2016). Additionally, AuNPs have been employed in photothermal therapy, photodynamic therapy, angiogenesis, tumor detection, genetic illness and condition identification, biosensors and photoimaging (Santhosh et al., 2022). In the literature, the production of AuNPs by green synthesis method from plant extract is quite common and its production is also possible with the help of BE (Piruthiviraj et al., 2016).

2.1.3.3.Zinc oxide nanoparticles

Zinc Oxide (ZnO) is a semiconductor and non-toxic material, and the nanoparticulates have a high surface-to-volume ratio (Osuntokun et al., 2019). The specific features of ZnO NPs, which are determined by their size and shape, could

explain their performance and commercial viability (Osuntokun et al., 2019). NPs have unique electrical, chemical, biological, and optical capabilities, which account for their widespread use in solar cells, light-emitting diodes, metal-insulator semiconductor diodes, photocatalytic degradation, wound healing, and drug delivery in biomedical applications. ZnO NPs have also been employed in various technologies, including micro-supercapacitors, acoustic waves, and optically transparent electrodes (Osuntokun et al., 2019). ZnO NPs are nanoparticles that can be created through physical, chemical, and biological processes. A few known examples include the manufacture of ZnO NPs utilizing aqueous leaf extracts of aloe vera, lemon, pisonia alba leaf, and broccoli in literature (Gayathri Devi et al., 2023, MuthuKathija et al., 2023, Osuntokun et al., 2019). In addition to the leaves, additional plant elements such as the stem and roots have been used in the green synthesis of ZnO NPs (Osuntokun et al., 2019). However, in many green synthesis productions, the biological properties of this nanoparticle have been examined, but thermal and magnetic analyses have not been included.

2.1.3.4.Titanium dioxide nanoparticles

Titanium dioxide (TiO_2) are well-known nanoparticles for their advantageous mechanical, electrical, optical, rheological, thermal, physicochemical, and biological characteristics (V T et al., 2023). TiO_2 NPs, which have antibacterial capabilities, are frequently employed in bandages, wound healing, and sunscreens, as well as to treat oral infections linked with tooth caries and periodontitis (V T et al., 2023). Furthermore, the significance of TiO_2 NPs stems from several of its features, such as being thermally stable, poorly soluble (hydrophobic), and not classed as a toxic or dangerous material (Santiago et al., 2023). At the microscopic level, TiO_2 NPs have a high volume/radious ratio, in addition to a wide bandwidth that absorbs electromagnetic radiation in the UV area, properties that are related to their photo-sensitivity and photocatalytic activities (Santiago et al., 2023). Although it is produced by many methods, the production of TiO_2 NPs by green synthesis method has been widely used in the literature, especially in biological applications from aloe vera, orange peel and hibiscus (Korde et al., 2023, Santiago et al., 2023,

Thakur et al., 2019). In one study, broad-spectrum antibacterial activity was demonstrated by synthetic TiO_2 NPs against a variety of diseases (Thakur et al., 2019).

2.1.3.5.Iron oxide nanoparticles

Iron, the most recent transition metal in the Earth's crust, serves as the foundation for today's infrastructure (Ali et al., 2016). In general, iron oxides are frequently employed due to their low cost and importance in a variety of biological applications (Ali et al., 2016). Ferromagnetic NPs with sizes of <10-20 nm show unique magnetism properties and magnetic iron oxide (Fe_3O_4 and γ-Fe_2O_3) NPs have gained popularity in biomedical applications due to their low toxicity, superparamagnetic properties, and easy separation methodology (Ali et al., 2016). Unsurprisingly, Fe_3O_4 NPs are biocompatible, biodegradable, and potentially safe for humans (Kiwumulo et al., 2022). These features increase the adaptability of Fe_3O_4 NPs and show tremendous promise in future biological applications like targeted drug delivery, antibacterial, tissue engineering, and so on (Kiwumulo et al., 2022). Especially due to its magnetic properties and non-toxicity, it is widely used in biomedical applications such as photothermal therapy, hyperthermia, cell labeling, immunoassays, targeting, detoxification of biological fluids, magnetic resonance imaging, and magnetically responsive drug delivery therapy, photodynamic therapy, and in cancer treatment (Singh et al., 2016). In the literature, iron oxide production has been achieved with many plants (Isik et al., 2023).

Overall, a review of the literature revealed that green synthesis was limited to biological applications and that the generated NPs lacked adequate characterization for each of the nanoparticles. Because of this, this thesis compared the in-depth characterization of several NPs made by green synthesis in order to investigate, for the first time, both the biological, thermal, electrical and magnetic applications. Thermal analysis was also performed to find the best nanoparticle to be used in the hyperthermia application that will be mentioned in the third part of the thesis. Optimization of the properties of the NPs was carried out so that they can be used in this application. For this, supplementation with other active substances such as

polydopamine (PDA) is a good option because of its excellent biocompatibility and biodegradability, good adhesion, photothermal conversion, oxidation resistance, luminescence, and multifunctional chemical reactivity properties (Wu et al., 2022). PDA has been widely applied to coating surface modification, and it is frequently utilized as a photothermal agent in cancer treatment (Li et al., 2023). Such photothermal agents readily stick to other materials and emit heat from near-infrared light (NIR), which kills cancer cells both in vitro and in vivo (Li et al., 2023). Through effective photothermal conversion, combining PDA and photothermal therapy (PTT) can lower toxicity, enhance biodegradability, and boost antitumor activity (Li et al., 2023). In previous studies, to improve bladder cancer immunotherapy, researchers have coupled photosensitizers and PDA composite NPs (Li et al., 2023). Additionally, other studies have combined PTT, chemotherapy, and tumor imaging with polymers, NPs, and PDA to control the proliferation of tumor cells in a synergistic manner (Ding et al., 2016). In this study, all nanoparticles were coated with PDA, and only their thermal properties were analyzed. Their ability to convert light energy into thermal energy was compared.

In current thesis chapter; Ag, Au, ZnO, TiO_2, and FeO NPs were synthesized using BE aqueous solution to compare the optical, physical, biological, morphological, and thermal properties of NPs and PDA coated NPs (NPs@PDA). Analyses were performed to identify the properties of these transition metal oxide NPs including X-ray diffraction (XRD), Scanning Electron Microscopy (SEM) with Energy Dispersive X-ray Spectroscopy (EDS), Fourier-transform Infrared Spectroscopy (FTIR), UV-visible spectrophotometry, Transmission Electron Microscopy (TEM), Vibrating Sample Magnetometer (VSM), Luciferase-based Cytotoxicity Assay and Hyperthermia analysis. This work makes it possible to characterize NPs in detail, evaluate their thermal properties for the first time unlike in previous literature, and synthesize them for specific applications which are hyperthermia for the third chapter and micro-supercapacitor for fourth chapter of the thesis.

2.2.Materials and Method

2.2.1. Materials

Broccoli (Brassica oleracea var. italica) was purchased from a commercial producer in Stuttgart, Germany. Iron (III) chloride ($FeCl_3$, anhydrous for synthesis, CAS Number:7705-08-0), silver nitrate ($AgNO_3$, Reagent Plus®, ≥99.0% (titration), CAS Number: 7761-88-8), gold (III) chloride trihydrate ($HAuCl_4.3H_2O$, ≥99.9% trace metals basis, CAS Number: 16961-25-4), zinc nitrate hexahydrate ($Zn(NO_3)_2.6H_2O$, reagent grade, 98%, CAS Number: 10196-18-6), zinc acetate dihydrate ($Zn(CH_3COO)_2 .2H_2O$, ACS reagent, ≥98%, CAS Number: 5970-45-6) and titanium (IV) isopropoxide ($Ti[OCH(CH_3)_2]_4$, 97%, CAS Number: 546-68-9) were used from Sigma-Aldrich. Isopropyl alcohol $(CH_3)_2CHOH$, CAS Number:67-63-0, Sigma-Aldrich) and distilled water (DW) were used as a solvent. For producing NPs@PDA, dopamine hydrochloride ($(HO)_2C_6H_3CH_2CH_2NH_2 \cdot HCl$, CAS Number: 62-31-7), dimethyl sulfoxide ($(CH_3)_2SO$, anhydrous, ≥99.9%, CAS Number: 67-68-5) and tris(hydroxymethyl)aminomethane ($NH_2C(CH_2OH)_3$, TRIS buffer, ACS reagent, ≥99.8%, CAS Number: 77-86-1) were also used from Sigma-Aldrich.

2.2.2. Green Synthesis of Transition Metal/Metal Oxide Nanoparticles

Preparation of Broccoli Extract

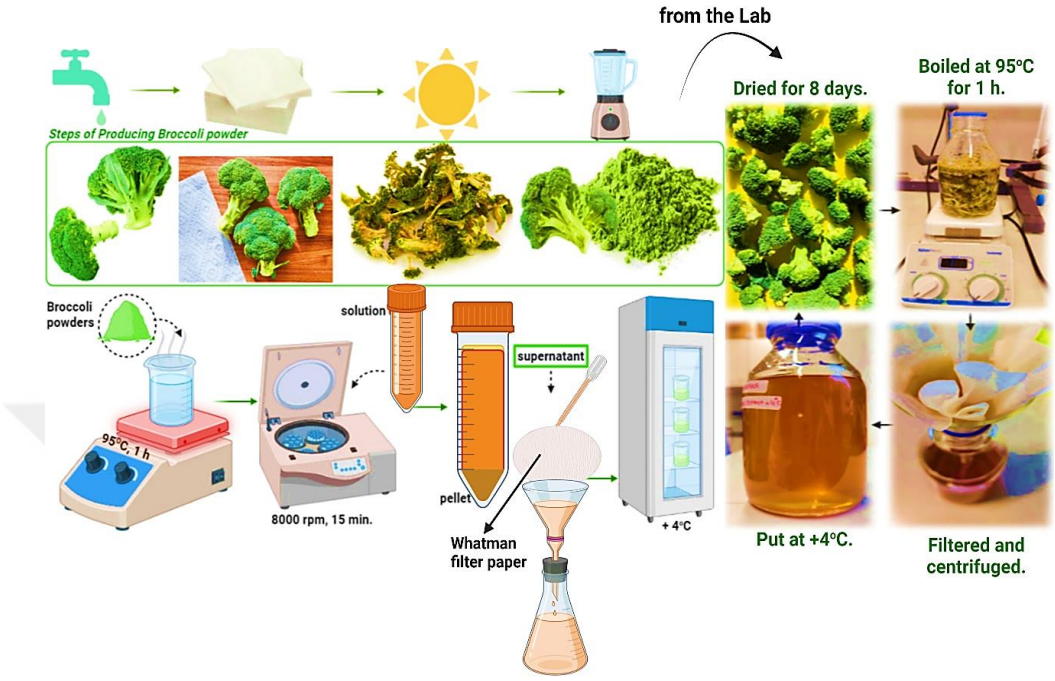


Figure 4: Synthesis steps of broccoli extract (Ersoy et al., 2024) [BioRender].

Broccoli was thoroughly cleaned with DW to remove dust and impurities. After washing, the rinsed broccoli was separated into pieces by hand and left at RT to dry for 7-8 days with sun light. Dried broccoli, which became powder, was weighed at 10 g to be made into the extract. Then, it was put into a beaker with 100 ml DW. The solution was mixed at 95° C in a magnetic stirrer for 1 hour. After that, the cooled solution was centrifuged at 8000 rpm for 15 minutes after filtering with Whatman filter papers. After centrifugation process, the supernatant was collected as broccoli aqueous extract, and it was filtered again. It had a pH of 5.8. BE solution was placed in the refrigerator at +4° C until it was used in the production of NPs (*Figure 4*) (Ersoy et al., 2024, Golli et al., 2023). The broccoli itself was not used; instead, the juice was removed. The recovered broccoli waste was not discarded; rather, it was stored as a carbon source for use in Chapter 4.

Synthesis of Silver Nanoparticles

0.1 M silver nitrate ($AgNO_3$) was weighed and added to 180 ml DW and embedded in a magnetic stirrer at RT for 5 minutes. Then, 20 ml BE was added to the solution and mixed at RT for 24 hours. The change of the solution came from light orange to dark brown at the end of 24 hours due to the bioreduction of silver nitrate into silver NPs and the reduction of Ag^+ to Ag^0 (Golli et al., 2023). Then, the solution was centrifuged at 6000 rpm for 10 minutes, the supernatant was removed, and the Ag NPs were washed twice with DW. The remaining sediment was calcined at 250° C for 2 hours and then ground into powder with the help of a mortar (Golli et al., 2023).

Synthesis of Gold Nanoparticles

180 ml of DW were weighed out, added to, and embedded in a magnetic stirrer for 5 minutes at RT with 4 mM of gold (III) chloride trihydrate ($HAuCl_4.3H_2O$), and 1 mM of gold (III) chloride trihydrate. After that, 20 ml of BE was added, and the mixtures were stirred for 25 hours at RT (Ersoy et al., 2024). The method of AuNP biosynthesis is a straightforward two-step process that does not necessitate a significant increase in temperature or pressure. The first stage involves mixing the biological extract (e.g., plant, bacterial, or fungal extract) with the $HAuCl_4$ salt solution, which reduces gold ions Au^{3+} to gold atoms Au^0 in the presence of H_2O molecules. In the second stage, growth and stability lead to the creation of AuNPs (Gurunathan et al., 2014, Santhosh et al., 2022). After 25 hours, the solution changed from pale yellow to dark orange. The supernatant was collected after the solution had been centrifuged at 6000 rpm for 10 minutes, and the Au NPs were then cleaned twice with DW. The leftover sediment was calcined at 250° C for 2 hours (Ersoy et al., 2024).

Synthesis of Zinc Oxide Nanoparticles

180 ml of DW were weighed out and mixed in a magnetic stirrer for 15 minutes at RT, and then each experiment was repeated with 0.1 M zinc acetate dihydrate, 1 M zinc acetate dihydrate and 0.1M zinc nitrate hexahydrate. Then 20 ml BE was added

to the solutions and mixed at 70° C for 2 hours. After that, the solutions were centrifuged at 6000 rpm for 10 minutes, the supernatant was removed, and the ZnO NPs were washed with DW. They were dried for 24 hours at 60° C. The remaining sediment was calcined at 500° C for 2 hours (Gayathri Devi et al., 2023).

Synthesis of Titanium Dioxide Nanoparticles

0.1 M titanium (IV) isopropoxide was weighed and added to 180 ml isopropyl alcohol and embedded in a magnetic stirrer at RT for 10 minutes. Then, 20 ml BE was added to the solution and mixed at 60° C for 5 hours. The color of the solution became cream-colored when BE was added, and a cream-colored solution with a gelled consistency was obtained at the end of 5 hours. Then, the solution was centrifuged at 6000 rpm for 10 minutes, and the supernatant was removed. They were dried for 24 hours at 60° C. The remaining sediment was calcined at 500° C for 2 hours (Anbumani et al., 2022, Shanavas et al., 2020).

Synthesis of Iron Oxide Nanoparticles

0.6 M iron (III) chloride ($FeCl_3$) was weighed and mixed at RT for 15 minutes in 180 ml DW (Niraimathee et al., 2016, Razack et al., 2020). The mixture went up to 29° C for 15 minutes and then cooled down. Then, 20 ml BE was added and mixed in a water bath at 60° C for 4 hours in the water bath beaker. It was centrifuged for 10 minutes at 6000 rpm, and the process was repeated three times with the DW. The supernatant solution was separated by putting a magnet bottom of the tubes, and the remaining product was dried at 60° C for 24 hours and calcined at 250° C for 2 hours. All experimental procedures of these NPs are also examined in *Figure 5*.

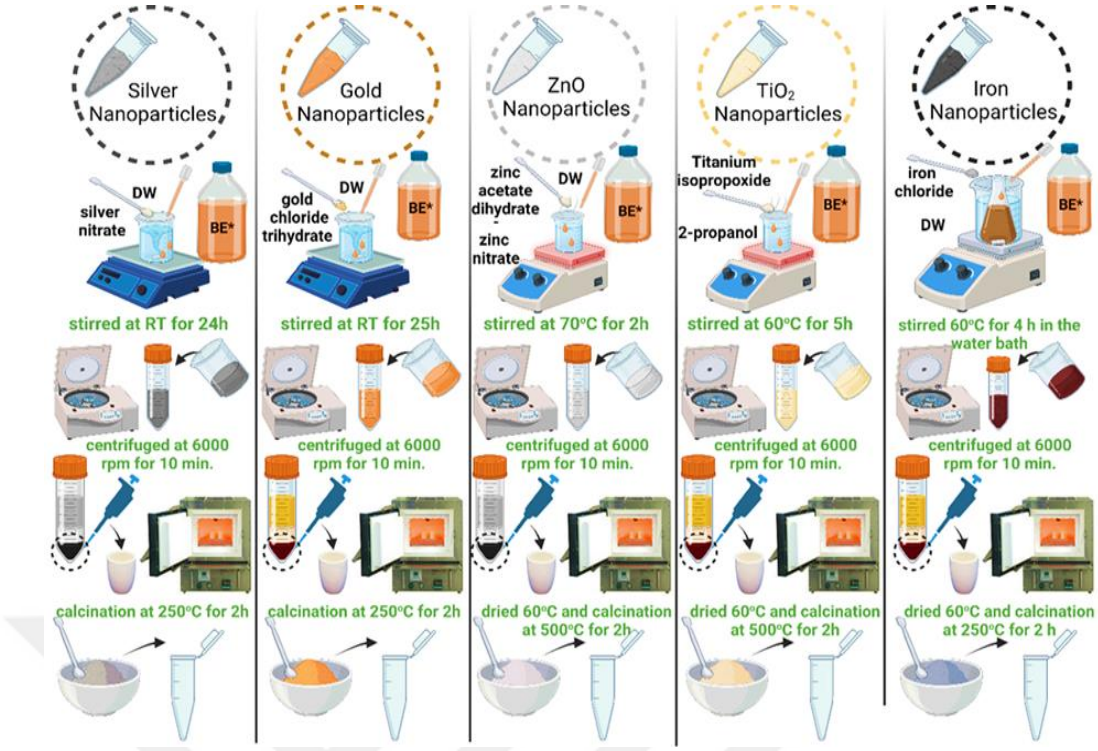


Figure 5: Diagrammatic illustration of the synthesis of metal/metal oxide nanoparticles [BioRender].

Since all NPs have different mechanisms at the same pH value, different process steps were applied when producing NPs.

Polydopamine Coating of Nanoparticles

All the prepared FeO, Au, Ag, ZnO, and TiO_2 NPs were coated with PDA. Its purpose is both to obtain more temperature in the analysis of hyperthermia (Ding et al., 2016, Li et al., 2023, Sridhar et al., 2023). For this purpose, hyperthermia analysis was performed for NPs@PDA and NPs samples. Firstly, NPs:DMSO was prepared at a ratio of 1:10 and sonicated under 150 W for 15 minutes into a beaker. Then, NPs:TRIS buffer was placed on it at a ratio of 1:19, and dopamine was added at a ratio of 1:1 for dopamine hydrochloride:NPs. After all the ingredients were added, they were mixed in a magnetic stirrer at 1000 rpm for 24 hours. The NPs@PDA solution obtained at the end of 24 hours was centrifuged at 8000 rpm for 10 minutes and washed with double DW three times to get rid of the excess unconjugated PDA. The same experimental steps were followed for all NPs (*Figure 6*). The morphological, thermal, optical, and biological characteristics of the

produced metal oxide NPs have been the subject of several analyses (Ersoy et al., 2024).

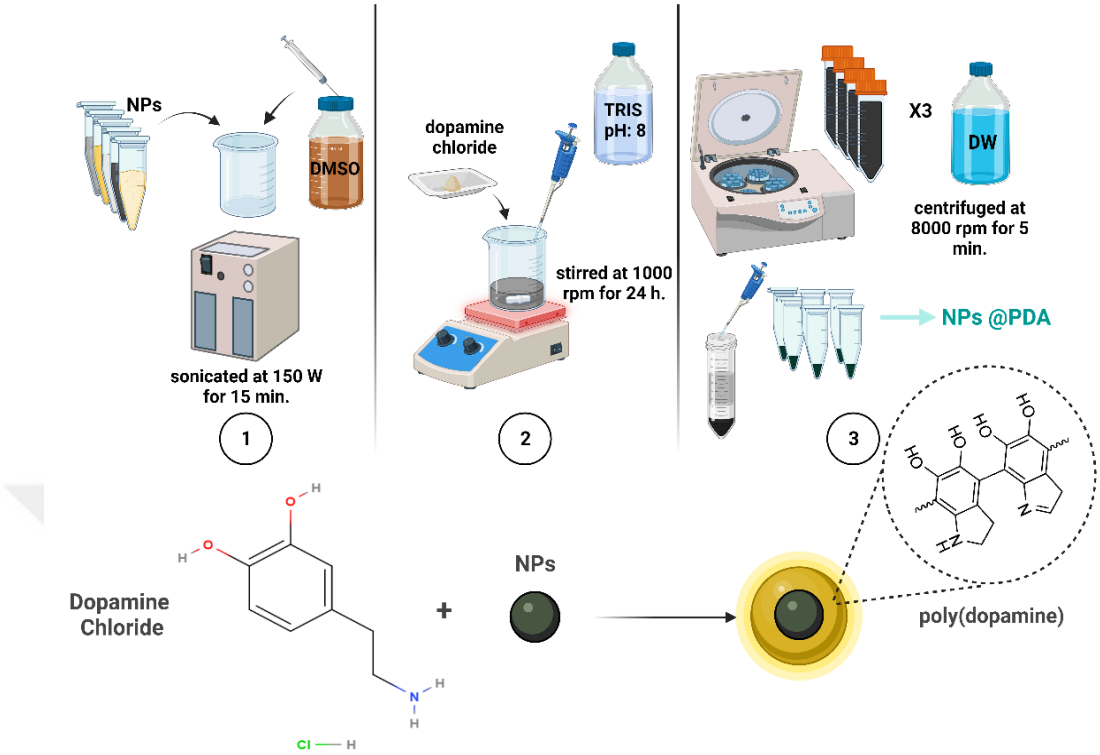


Figure 6: Conjugation steps of all synthesized nanoparticles with PDA (Ersoy et al., 2024) [BioRender].

2.2.3. Characterizations of Nanoparticles

Physical, chemical, biological and thermal analyses of the synthesized NPs were investigated (*Figure 7*).

X-ray diffraction (XRD)

The crystallographic structure and physical properties of a material can be precisely determined using a non-destructive technique called XRD. The samples were scanned using a ceramic X-ray tube and 2.2 kW copper anode radiation at 1.54 wavelength from a D8 Advance Bruker XRD (Mehmet ATEŞ, 2018) for 7 hours each of them.

Scanning electron microscopy (SEM) with energy dispersive X-ray ppectroscopy (EDS)

For SEM analysis, NPs were suspended in 1 ml of ethanol and air dried on silicon substrates (Reference Module in Chemistry, Molecular Sciences and Chemical Engineering, 2018) to understanding the morphological behaviors of NPs. The samples were then sputter coated with 10 nm of gold. The observation was carried out in Zeiss Ultra 55 Gemini SEM equipped with a nitrogen cooled EDAX detector. The samples were attached to aluminum stubs using carbon tape. Images were taken in secondary electron mode at working distances 15-36 mm, accelerating voltage 3-5 kV. The EDS method from Thermo Scientific was used to determine the elemental composition of the NPs. When the particles were 1 μm in size, the region where the particles were dense was selected, and EDS analysis was performed according to the kV value of each element. Moreover, according to the EDS data, the silicon (Si) ratio was high because the number of NPs was low.

Fourier-transform infrared spectroscopy (FTIR)

FTIR was used to confirm the functional groups like -NH_2, -OH, -COOH in molecules that vibrate when exposed to particular light wavelengths (NicDaéid, 2018) of the produced NPs. With the TENSOR II FTIR Platinum ATR Routine Spectrometer from Bruker Optics, the spectroscopic investigation was carried out over a wide wavenumber range of 500-4000 cm^{-1}.

UV-Visible spectrophotometry

Many substances have chromophores, which can be understood using a UV-visible spectrophotometer and can absorb specific visible or UV light wavelengths using the Beer-Lambert law (NicDaéid, 2018). Deuterium and tungsten lamps were used and UV-visible range between 200 and 1500 nm by adding 2 ml of ethanol to the NPs inside a quartz bathtub with Perkinelmer LAMBDA 1050+ UV/Vis/NIR Spectrophotometer.

Transmission Electron Microscopy (TEM)

TEM was performed with a Philips CM200 microscope. 1µl of nanoparticle suspension was deposited on a copper grid and slowly air dried. The samples were observed by TEM under 200kV accelerating voltages. Imaging was simple for materials with electron densities noticeably higher than formless carbon (Mehmet ATEŞ, 2018). TEM analyses of NPs were measured using the ImageJ program.

Vibrating Sample Magnetometer (VSM)

VSM was performed to study the magnetic properties of the NPs with a Microsense EZ7. 1 mg of nanoparticles were mixed with wax and loaded on the 8 mm transverse holder for the measurements. The findings of magnetizations (M)/ magnetic field (H) are shown as M-H hysteresis loops (Ali et al., 2019, Kanwal et al., 2019).

Luciferase-based cytotoxicity assay

For the cytotoxicity experiment, BJ cells, which are fibroblasts generated from skin, were employed. The base medium for this cell line is the ATCC-formulated Eagle's Minimum Essential media, Catalog No. 30-2003. To generate the complete growth medium, mix the fetal bovine serum with the basic medium until it reaches a final concentration of 10% (Soon et al., 2022, Sun et al., 2020). The cells multiplied for one week before they were prepared for cytotoxicity testing. Each sample had a concentration of 2 mg, 12.5, 25, 50, 100, 200, and 400, and an analysis was done to determine the minimal toxicity value, which was 800 mg/ml.

Hyperthermia analysis

For the thermal analysis, the degree of warming of the NPs was observed for 20 minutes using M470F3 nm (blue-violet) light at 470 nm and FLIR thermal camera with the led current of 1000 mA, according to the UV-visible spectrophotometer

data. 2 ml of ethanol was put into the nanoparticle powders in the capsules and sonicated for 1 minute with a sonicater before hyperthermia analysis. The NPs@PDA solution was left with its contents, and no ethanol was added. Every 5 minutes, the images on the camera were screen-shot, and the production of heat energy from light energy was observed for each nanoparticle for 20 minutes (Sun et al., 2020, Zhang et al., 2024).

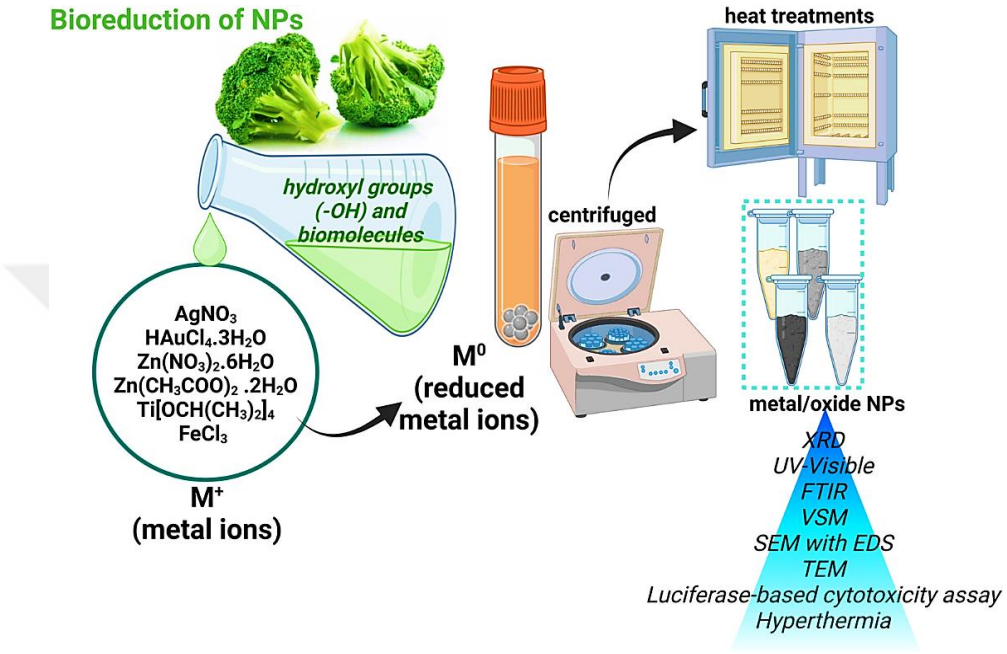


Figure 7: Bioreduction and characterizations of various NPs [BioRender].

2.3.Results and Discussion

Silver Nanoparticles

Four unique diffraction peaks found in the XRD examination of the produced Ag NPs point to face-centered cubic Ag crystals (JCPDS no. 00-004-0783) in *Figure 8(a)*. Furthermore, 2-theta values between 20 and 80º produced peaks that were consistent with those in earlier research published in the literature and may suggest the presence of AgNPs (Pawar et al., 2016). Results from TEM and SEM analyses

were used to evaluate and understand AgNPs and other materials. The analysis of *Figure 8(b-e)* indicates that AgNPs doped with BE exhibited nanosphere and nanocube shapes (Lee, Jun, 2019). It was also observed that the spherical structured NPs were homogeneous (Lee, Jun, 2019). As per the TEM examination, the nanoparticles' particle size was roughly 37-80 nm. When the results obtained from TEM analyses were compared with the silver NPs produced from BE in the literature, it was seen that the NPs produced in this thesis were smaller and nano-sized and their shapes were more homogeneous (Golli et al., 2023). The percentiles of the element ratios in the NPs were added to the table based on the elemental analysis results of the peaks in *Figure 8(b).*

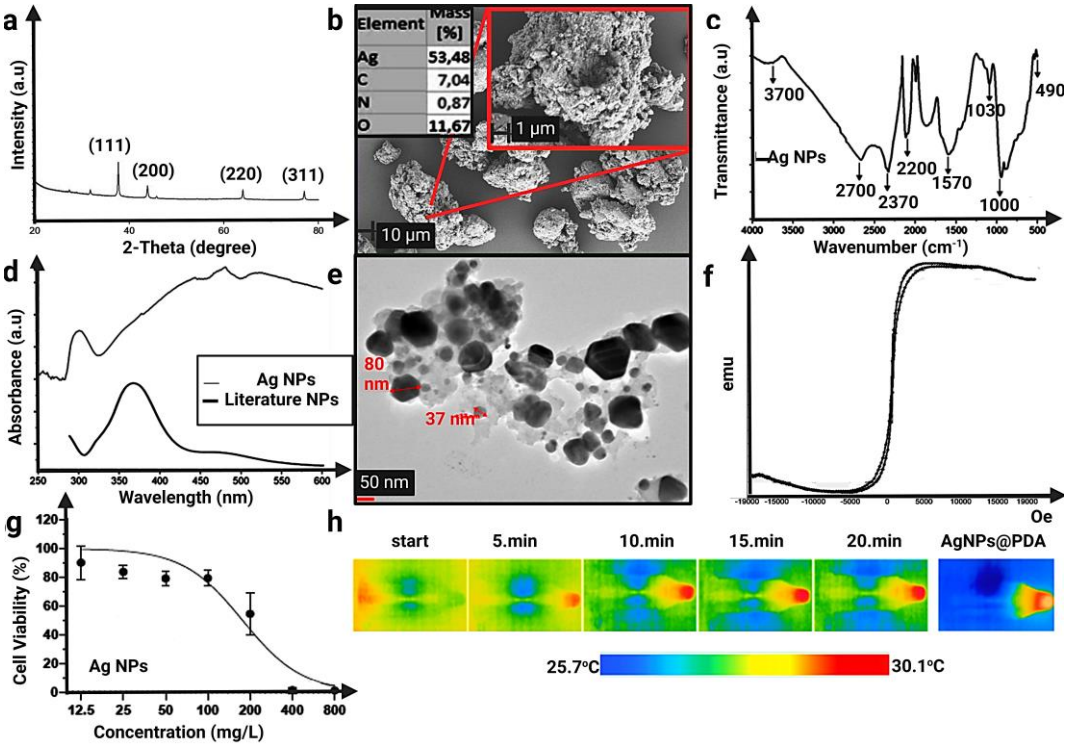


Figure 8: Characterizations of AgNPs: **a** XRD analysis; **b** SEM analysis at 10 and 1 micrometers with an EDS analysis table; **c** FTIR graph between 4000 and 500 cm^{-1}; **d** UV-visible spectrophotometer graph between 250 and 600 nm; **e** TEM image at 50 nm scale and particles size are approximately 37 nm; **f** VSM analysis data from magnetization (emu)/ H (Oe) graph; **g** luciferase-based cytotoxicity assay results according to the concentration; and **h** hyperthermia analysis results at 470 nm (blue-violet) light for AgNPs and AgNPs@PDA after 20 min [BioRender].

In the EDS analysis, 53.48% silver element was observed, while 11.67% oxygen element was found. In addition, the presence of 7.04% carbon element was thought to come from the carbon tapes used during the analysis. The fingerprint-area peaks

for silver NPs with BE were observed in the FTIR spectra at 3700 cm^{-1}, 2370 cm^{-1}, 1570 cm^{-1}, and 490 cm^{-1} (*Figure 8(c)*). It was observed that the peak in the 3700 cm^{-1} band belongs to O-H bonds (Golli et al., 2023). N-H bonds which are come from the proteins are represented by the wavenumber 1570 cm^{-1}, while C-C bonds are represented by the wavenumber 2370 cm^{-1}. It is evident that the aromatic primary amines' planar bending vibration had a C-H bond at 490 cm^{-1} and a C-H bond at 2700 cm^{-1}. This information indicates that functional groups are necessary for the synthesis of silver NPs because they supply reducing groups that facilitate the creation of NPs (Golli et al., 2023). Additionally, the band at 100–1030 cm^{-1} may contain cellulose's C–O–H deformation, while the band at 2200 cm^{-1} may contain nitrile carbenes. The bands at 1450 cm^{-1} and 1043 cm^{-1} correspond to the N–H and C–N (amines) stretch vibrations of the proteins, respectively (Jyoti et al., 2016). Upon examining the UV-visible result of the silver nanoparticle (*Figure 8(d)*), it is observed that the peak signifies a larger energy than the silver NPs reported in literature that were generated using conventional methods (ATEŞ et al., 2021, Singh et al., 2015). *Figure 8(f)* shows the magnetizations (emu)/ magnetic field H (Oe) graph for the silver nanoparticle The S-shaped M-H curves in *Figure 8(f)* illustrate the ferromagnetic behavior. The resulting curve showed zero coercivity and remanence values, as well as a characteristic magnetic hysteresis (Kanwal et al., 2019). Coercive field means the field at which M//H changes sign, while retentive means M at H=0 (Patil, Behera, 2023). The decrease in the Ms value and the increase in the Hc value mean that the magnetic property decreases. However, the fact that it shows a regular S shape means that it still shows a little magnetic property. If the ends of the S shape approach the y-axis, the Ms value increases, but if they approach the x-axis, the Ms value decreases (Patil, Behera, 2023). Ag NPs in *Figure 8(f)* had a mean standard deviation of 3.92E-3 emu, a saturation magnetization (Ms) value of 4.31E-3 emu, a retentively (Mr) value 595.403E-6 and a coercivity (Hc) value of 82 Oe. The results of the cell viability examination of AgNPs (*Figure 8(g)*) show that as the concentration of NPs rose, cell viability reduced. As demonstrated in *Figure 8(h)*, after 20 minutes, the PDA coating raised the temperature of the AgNPs from 27.9 to 30.1° C more quickly and significantly.

Gold Nanoparticles

AuNPs analysis and interpretation of the results are also explained in detail in the published article (Ersoy et al., 2024). XRD was used to verify that the produced AuNPs were crystalline. Four distinct sharp peaks at 2θ angle between 20 and 80° are visible in the XRD spectrum at 38.2°, 44.4°, 64.5° and 77.3°, with Bragg reflections corresponding to (111), (200), (220), and (311) in biomass-associated AuNPs which are cubic-face centered gold [24] that were previously described in a prior work (Gurunathan et al., 2014) in *Figure 9(a).* The peaks in this thesis were matched with the Joint Committee on Powder Diffraction Standards (JCPDS) card No. 893722 (Santhosh et al., 2022).

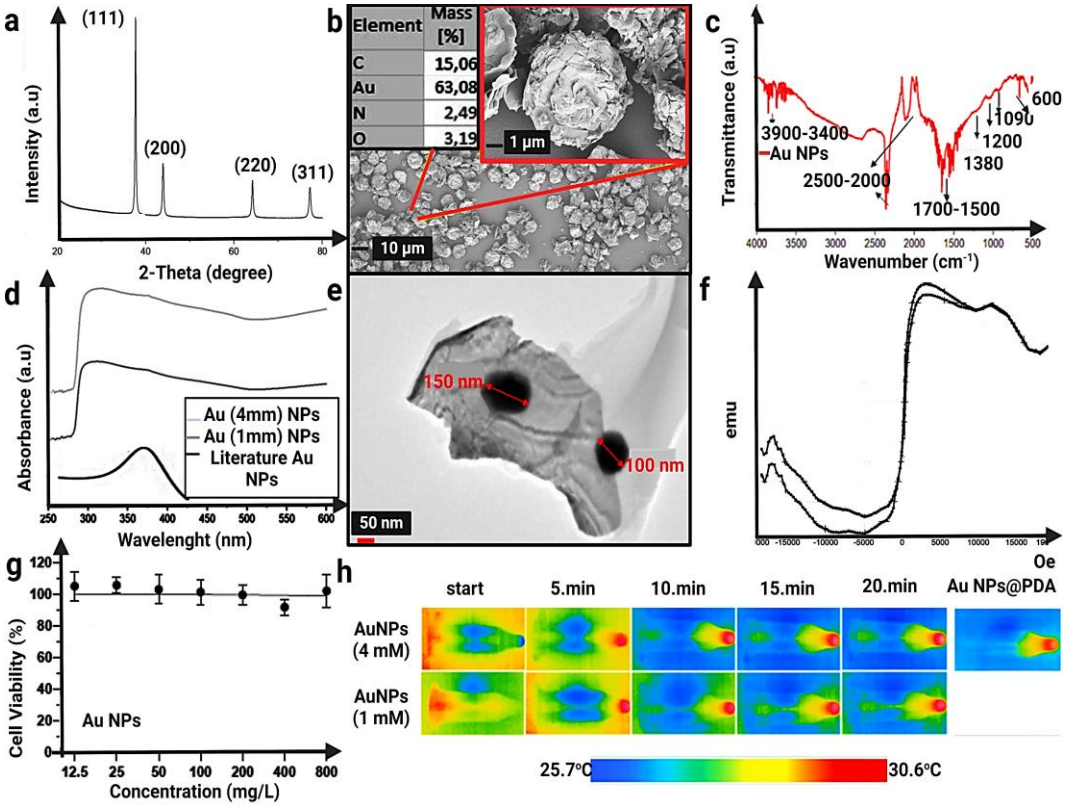


Figure 9: Characterizastions of AuNPs: **a** XRD analysis; **b** SEM analysis at 10 and 1 micrometer with EDS analysis table; **c** FTIR graph between 4000 and 500 cm^{-1}; **d** UV-visible spectrophotometer graph between 250 and 600 nm for 4 and 1 mM gold nanoparticles; **e** TEM image at 50 nm scale and particles size are approximately 100 nm; **f** VSM analysis data from magnetization (emu)/ H (Oe) graph; **g** luciferase-based cytotoxicity assay results according to the concentration of gold nanoparticles with non-coated PDA; and **h** hyperthermia analysis results at 470 nm for 1 and 4 mM Au NPs and (4 mM) AuNPs@PDA (blue-violet) light after 20 min (Ersoy et al., 2024) [BioRender].

When examining the SEM analysis *Figure 9(b, e),* it was seen that the AuNPs, which had appeared as nanospheres in the TEM analysis, were in the structure of nanoflowers. In a study in the literature, NPs were produced using BE, but it was observed that the nanostructures were spherical. Although the same $HAuCl_4$ was used, it was determined that the duration and temperature of the extract changed the morphological structure of the produced nanoparticle (Santhosh et al., 2022). As per the TEM examination, the nanoparticles' particle size was roughly 100-150 nm. Nanoflowers are a novel class of NPs with a flower-like structure. This approach is gaining popularity due to its great stability, efficiency, and ease of preparation. Nanoflowers have multiple applications, including biosensors, medication delivery, and purification (Ahire et al., 2022). The amide I, II, and III bands of polypeptides and proteins in *Figure 9(c)* for AuNPs with BE correlate to the 600, 1090, 1200, 1380, and 1630 cm^{-1} bands, and they are in line with previous results (Gurunathan et al., 2014). Furthermore, the bands at 1630 cm^{-1} are indicative of the vibrational modes of the C=C double bonds in these compounds (Gurunathan et al., 2014). It was observed that C–N from aromatic and aliphatic amines may be caused by the 1380 and 1090 cm^{-1} band values (Santhosh et al., 2022).

In previous studies, it was found that there may be peaks around 600 cm^{-1} caused by the bonding of carbon with halogen groups and that this is due to the extract used (Santhosh et al., 2022). The carbonyl and hydroxyl functional groups found in alcohols and phenol derivatives are represented by the bands at 3490 cm^{-1}, while the C=O stretching frequency range is represented by the big peak between 1500 and 1700 cm^{-1} (Gurunathan et al., 2014). Furthermore, nitrile carbenes may be present in the bands between 2000 and 2500 cm^{-1}. According to earlier studies published in the literature, the absorbance value of 0.12 for AuNPs made using conventional methods seems to peak between 350 and 500 nm (Cytodiagnostics, 2024). In the studies, it was observed that as the size of the nanoparticle decreases, the peak is observed in the lower wavelength range. For example, while the study in the literature is for a nanoparticle of 10-5 nm size, in this thesis study, a sharp double peak structure can be observed in the production of 100-150 nm sizes. In addition, when the absorbance peaks of AuNPs synthesized at 4 mM and 1 mM were examined, it was thought that the NPs produced at 4 mM ratio could have smaller sizes. Because as the absorbance value decreased, the particle size increased

in the study in the literature (Cytodiagnostics, 2024). As seen in *Figure 9(d),* this peak does, however, vary in form and concentration. A specific shape was absent from the M-H graphs in *Figure 9(f).* For AuNPs, the measurements were as follows: the Hc value was 82.350 Oe, the Mr value was 89.032E-6 emu, the Ms value was 628.6E-6 emu, and the standard deviation was 478.45E-6 emu (Kanwal et al., 2019). A regular S structure could not be observed in the graph. The results of the cytotoxicity investigation for AuNPs are shown in *Figure 9(g).* Broccoli has two purposes: it lowers the gold salt and then uses its thiol compounds to surface cap the resulting NPs, stabilizing them (Khoobchandani et al., 2013). Additionally, AuNPs encapsulation is made possible by BE, offering improved in vitro stability against agglomeration. AuNPs in combination with broccoli phytochemicals have been shown in the literature to demonstrate good internalization within prostate (PC3) and breast (MDA-MB-231) cancer cells, leading to in vitro anticancer activities against a range of cancer cells (Khoobchandani et al., 2013). Out of all the NPs, AuNPs had the highest cell viability. Furthermore, the 1 mM gold nanoparticle in *Figure 9(h)* was not examined as it was noted that the 4 mM gold nanoparticle had the greatest temperature recorded (28.6º C). Among all NPs, AuNPs@PDA has been recorded at the greatest temperature at 30.6° C (Ersoy et al., 2024). When the thermal analysis of the nanoparticle was examined, no significant temperature increase was observed between the 10th and 20th minutes, but all nanoparticle analyses were still performed for 20 minutes. In addition, the proof of the PDA coating was also performed by thermal analysis. Since the highest cell viability and thermal energy production were seen in AuNPs, AuNPs were selected for hyperthermia application despite their large particle size.

Zinc Oxide Nanoparticles

Figure 10(a) displays the XRD patterns for the ZnO NPs that were produced. For the hexagonal wurtzite ZnO phase, the diffraction peaks may be ascribed to the lattice planes (h, l, k) of (100), (002), (101), (102), (110), (103), (200), (112) at 2θ values of 37.0°, 40.23°, 42.39°, 55.85°, 66.77°, 74.62° and 78.89° (MuthuKathija et al., 2023, Osuntokun et al., 2019). The diffraction peaks are consistent with the powder diffraction standard established for the hexagonal phase of ZnO NPs (JCPDS No79-2205) (Osuntokun et al., 2019). The very crystalline nature of the produced ZnO NPs is shown by the considerable peak intensity

(MuthuKathija et al., 2023). The zinc nitrate (0.1 M), zinc acetate (0.1 M), and zinc acetate (1 M) in *Figure 10(b–e)* each have the well-known rod-like shape found in the literature and exhibit porosities in that order (MuthuKathija et al., 2023).

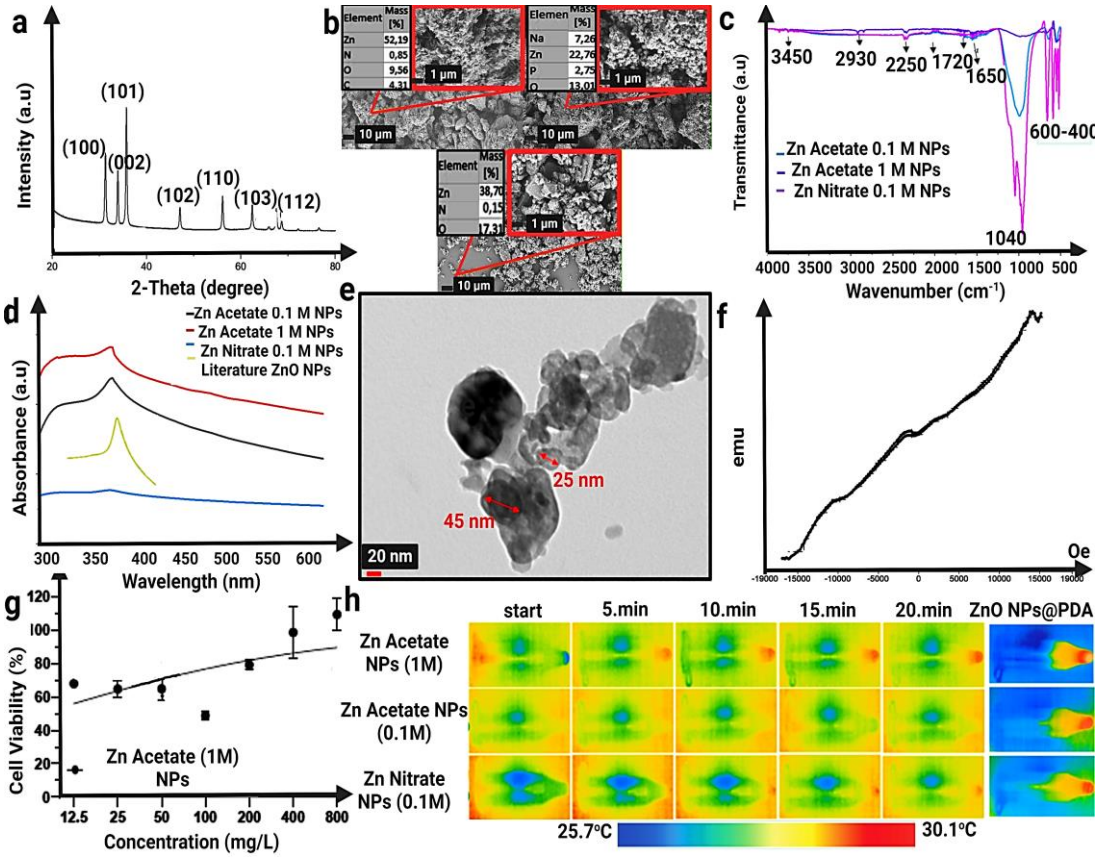


Figure 10: Charahterizations of ZnO NPs: **a** XRD analysis; **b** SEM analysis of zinc nitrate (0.1M) NPs; zinc acetate (0.1M) NPs; and zinc acetate (1M) NPs at 10 and 1 micrometer with EDS analysis table respectively; **c** FTIR graph between 4000 and 500 cm^{-1}; **d** UV-visible spectrophotometer graph between 300 and 600 nm for 0.1, 1 M Zinc acetate and 0.1 M Zinc Nitrate NPs; **e** TEM image at 50 nm scale and particles size are approximately 25 nm; **f** VSM analysis data from magnetization (emu)/ H (Oe) graph; **g** luciferase-based cytotoxicity assay results according to the concentration of ZnO NPs with non-coated PDA; and **h** hyperthermia analysis results at 470 nm for ZnO NPs and NPs@PDA (blue-violet) light after 20 min [BioRender].

The porosity and rod-shaped structure in the most recent SEM images grew together with the density of zinc acetate. As per the TEM study, the NPs had a size of about 25 nm. In the EDS analysis, 52.19% Zn element was found in NPs produced with 0.1 M zinc nitrate, 22.76% Zn element in NPs produced with 0.1 M zinc acetate and 38.70% Zn element in NPs synthesized with 1 M zinc acetate, respectively. In

addition, the presence of oxygen in the particles and XRD planes proved that ZnO NPs were produced. The peak in *Figure 10(c)* for Zn NPs with BE is measured at 3450 cm^{-1} due to O-H stretching. In addition, due to different bioactive compounds found in broccoli, the peak in the 3450 cm^{-1} band may overlap with the N-H of amines (Osuntokun et al., 2019). An absorption peak at 2930 cm^{-1} indicates the presence of the alkyl (methyl) group's C-H stretches. The bands at 2250 cm^{-1} may be made up of carbene nitrile. The peaks at 1720 cm^{-1}, which are associated with carboxylic acids or their esters, are the result of C=O bond stretching vibrations induced by non-ionic carboxylic groups (MuthuKathija et al., 2023). The peaks at 1650 cm^{-1} that were found as a result are related to the N-H bending vibration of amine or amide groups. Peaks at 1040 cm^{-1} were identified as aliphatic amines' C-N or C-H, C-O stretching vibrations (Osuntokun et al., 2019). Furthermore, the peaks observed in the region of 600–400 cm^{-1} have been attributed to the metal-oxygen. Thus, the literature (MuthuKathija et al., 2023) indicates that the high-intensity band at 444 cm^{-1} is caused by zinc (Zn-O) and oxygen. It has been discovered that the peaks in the literature are more similar to those of zinc acetate dihydrate and ZnO NPs made at a concentration of 1 M. It sought to examine the concentration difference between 1 M and 0.1 M zinc acetate as well as the variation between 0.1 M and 0.1 M zinc nitrate for ZnO NPs. Zinc acetate has a larger absorbance and a more appropriate wavelength value than zinc nitrate, as seen in *Figure 10(d)* (Estrada-Urbina et al., 2018). Moreover, a greater absorption value has been observed for zinc acetate at high concentrations. In the literature, a peak around 350 nm was observed in the UV-visible analysis of ZnO NPs synthesized with the help of BE (Osuntokun et al., 2019). A specific form was absent from the M-H graphs in *Figure 10(f).* Zn acetate NPs had a mean standard deviation of 512.76E-6 emu, a Ms of 957.87E-6 emu, a Mr 14.728E-6 emu and a Hc value of 0.005 Oe, respectively. Zn nitrate NPs had a mean standard deviation of 417.06E-6 emu, a Ms of 832.75E-6 emu, a Mr of 69.013E-6 and a Hc value of 0.023 Oe. As shown in *Figure 10(h),* which shows late and slightly heated NPs (27.4, 27, and 27.3° C), PDA coating allowed the particles to achieve high temperatures (30.5, 29.6, and 29.7° C, respectively). The PDA effect was observed in ZnO NPs and ZnO NPs@PDA particles. It has been proven that zinc oxide nanoparticles can produce heat energy by absorbing more light in the presence of PDA.

Titanium Dioxide Nanoparticles

The TiO_2 XRD spectrum in *Figure 11(a)* indicates that the generated NPs are well matched with the JCPDS card No. 71-1166, and this is corroborated by data from the literature. Six distinct peaks in the data are indicative of the NPs. The lattice planes in the earlier study (Shanavas et al., 2020) are (101), (004), (200), (211), (204), and (116), corresponding to the diffraction peak at 2-theta 25.2°, 37.7°, 47.9°, 54.7°, 62.7°, and 69.8°.

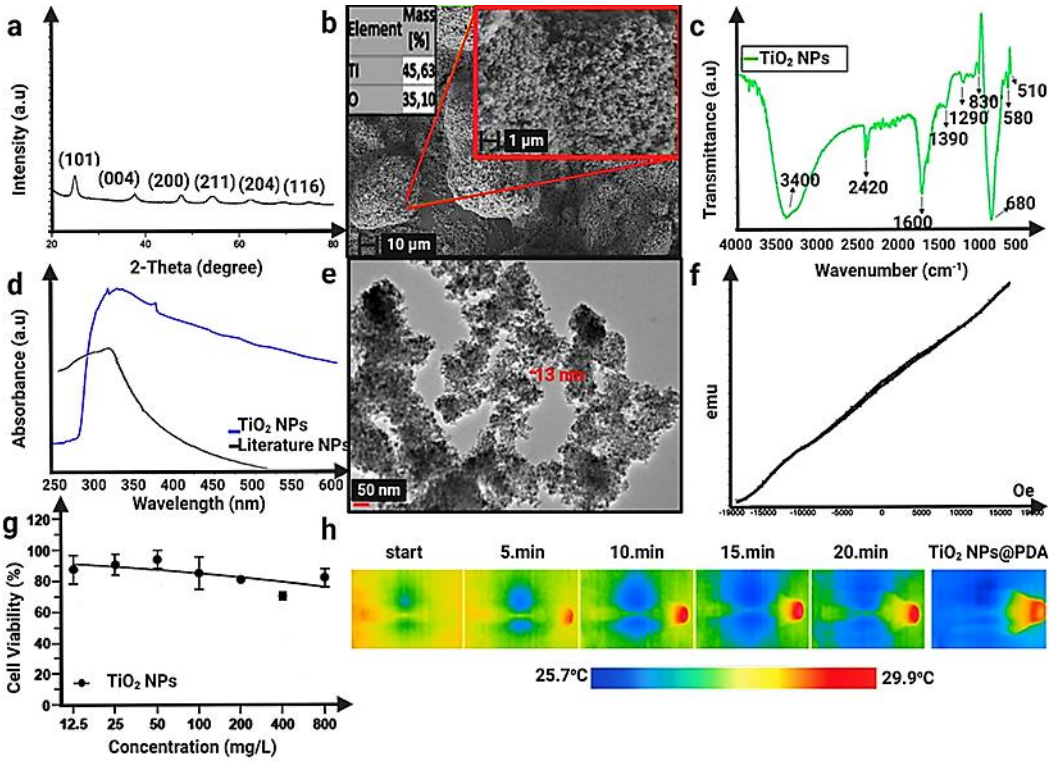


Figure 11: Characterizations of TiO_2 NPs: **a** XRD analysis; **b** SEM analysis of TiO_2 NPs at 10 and 1 micrometer with EDS analysis table; **c** FTIR graph between 4000 and 500 cm^{-1}; **d** UV-visible spectrophotometer graph between 250 and 600 nm; **e** TEM image at 50 nm scale and particles size are approximately 13 nm; **f** VSM analysis data from magnetization (emu)/ H (Oe) graph; **g** luciferase-based cytotoxicity assay results according to the concentration of titanium dioxide nanoparticles with non-coated PDA; and **h** hyperthermia analysis results at 470 nm (blue-violet) light for TiO_2 NPs and TiO_2NPs@PDA after 20 min [BioRender].

Additionally, these XRD peaks are associated with TiO_2 NPs that were created with BE's assistance. The TiO_2 nanoparticle's TEM and SEM pictures were both consistent with expectations. The structure of the nanosphere is dense and relatively vast. The average particle size is approximately 10 nm (*Figure 11(b-e)*). To determine the elements in the structure and their percentages, EDS analysis was

done. It has been established that titanium metal is present in the particles. According to EDS analysis, 45.63% titanium element was observed and 35.10% oxygen was observed. Thus, it was proven that TiO_2 NPs were produced successfully. TiO_2 NPs production using BE has not been found in the literature. Therefore, when compared to TiO_2 NPs microstructures synthesized using other plant extract which is aloe vera, it was determined that smaller nanoparticle sizes were produced than in the literature (Santiago et al., 2023). At the same time, spherical, non-agglomerated, homogeneous NPs were produced in this study. TiO_2 NPs containing BE are seen in *Figure 11(c)* as bands at 510, 580, 680, 830, 1290, 1390, and 2420 cm^{-1}. Specifically, the transmittance peak at 1390 cm^{-1} is caused by the C-H alkyl stretching vibration. The synthesis of Ti-O-Ti is confirmed by the formation of an FT-IR transmission peak between 400 and 800 cm^{-1}, which is in charge of the stretching vibration of the metal-oxygen bonding (Shanavas et al., 2020). The FT-IR transmittance peak at 2420 cm^{-1} is responsible for the aldehydic stretching bond of the C-H functional group. The biomolecules include protein amide III groups, as indicated by the FT-IR peak at 1290 cm^{-1} (Shanavas et al., 2020). Carboxyl groups are present in amino acids, as seen by the signal at 1390 cm^{-1} (Shanavas et al., 2020). The bands for the O-H band at 3400 cm^{-1} and the C-C bands at 1600 cm^{-1} are also included. The peak nm similar to that reported in the literature has also been found for TiO_2 in *Figure 11(d)* (K. Ganapathi Rao, 2014). In contrast to the UV analysis reported in the literature, the peak was observed in the 350–400 nm region and was higher. A particular form was absent from the M-H graphs in *Figure 11(f).* For TiO_2 NPs, the mean standard deviation was measured at 1.285E-3 emu, the Ms was 2.279 E-3 emu, the Mr was 34.367E-6 and the Hc value was 0.030 Oe. According to *Figure 11(g),* cell viability decreases with increasing nanoparticle concentration; hence, if TiO_2 NPs are to be used in health research, they should be used sparingly. It has been demonstrated in *Figure 11(h)* that PDA-coated NPs outperform coated NPs in all cases.

Iron Oxide Nanoparticles

In *Figure 12(a),* the XRD pattern showed four unique 2 peaks at 23.6º, 28.7º, 33.9º, and 39º, respectively, with indices of (1 3 0), (3 2 2), (0 1 6), and (1 5 1), and they agree with the findings of earlier research. The literature (Niraimathee et al., 2016) indicates that they bear a striking resemblance to the orthorhombic-structured peaks

of iron oxide crystals and the results are consistent with the conventional XRD pattern of Fe_3O_4 (JCPDS 76-0958) (Niraimathee et al., 2016). However, the planar peaks indicating the crystal structure of the produced nanoparticle are not as sharp as in the literature (Kumar et al., 2023).

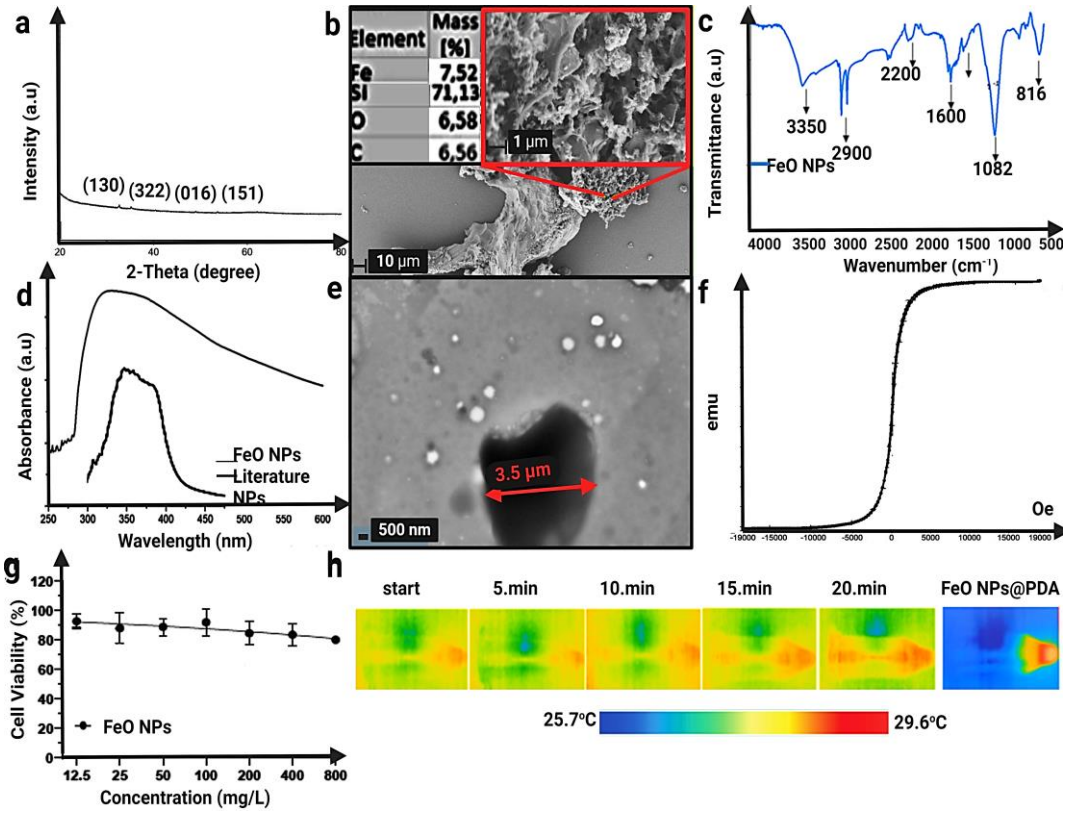


Figure 12: Characterizations of FeO NPs. **a** XRD analysis; **b** SEM analysis of iron oxide NPs at 10 and 1 micrometer with EDS analysis table; **c** FTIR graph between 4000 and 500 cm^{-1}, **d** UV-visible spectrophotometer graph between 250 and 600 nm; **e** TEM image at 500 nm scale and particles size are approximately 3.5 micrometer; **f** VSM analysis data from magnetization (emu)/ H (Oe) graph; **g** luciferase-based cytotoxicity assay results according to the concentration of iron oxide nanoparticles with non-coated PDA; and **h** hyperthermia analysis results at 470 nm (blue-violet) light for iron oxide NPs and iron NPs@PDA after 20 min [BioRender].

Figure 12(e) was not a perfect image due to the thicker FeO NPs, while *Figure 12(b)* looked like a snowflake. In TEM analysis, thick coatings do not produce a decent image. As per the TEM examination, the nanoparticles' particle size was roughly 3.5 µm. FeO NPs synthesized with BE were not found in the literature. When iron oxide NPs synthesized from Mimosa pudica root extract were examined, it was observed that the NPs clustered due to their magnetic effect (Niraimathee et al., 2016). The band situated at 900-600 cm^{-1} in *Figure 12(c)* denotes F-O bonds.

Polyphenol compounds are indicated by the absorption band at 1600 cm^{-1}, which is linked to the stretching of the C=O bond. Iron oxide NPs are formed through the reduction of iron ions, a process that is facilitated by phenol groups and polyphenol compounds (Razack et al., 2020). The water-soluble polyphenol compound that has coated the surface of the generated Fe NPs is represented by the band with the maximum intensity, which is ascribed to the O-H groups. The CO_2 in the sample compartment or C-N stretching from unreacted impurities could be the cause of the band at 2200 cm^{-1}. The band at 3350 and 2900 cm^{-1}, which represents the O-H bond's stretching, indicates the aqueous phase. The reduction of ferric chloride is shown by an increase in the absorption band (Razack et al., 2020). In comparison to prior work (Alagumira Meyyapan, 2014), the UV-absorbance graph shows that the peak at the same wavelength value in *Figure 12(d)* was produced with a higher absorbance value in iron NPs. The super-paramagnetic nature of iron NPs is supported by all of these features in *Figure 12(f)* if the NPs are dried at 60° C for a day prior to calcination (Ghodake et al., 2021). The measurements of the mean standard deviation, Ms, Mr and Hc for Fe NPs were 27.39E-3 emu, 29.60E-3 emu, 1.74E-3 emu and 53.908 Oe, respectively. Cell viability declined with concentration in *Figure 12(g),* but not as much as it did for the other NPs that is. *Figure 12(h)* shows that after 20 minutes, the late and weakly heated NPs (27.8° C) could attain high temperatures when coated with PDA (29.7° C). As in other nanoparticle results, the presence of PDA was proven by thermal analysis. Although FeO NPs were kept under blue laser light for 20 minutes, they did not produce as much heat energy as when coated with PDA.

Discussion

The production of metal oxide NPs using plant extract and "green synthesis" have gained a lot of attention in the literature since it is affordable, sustainable, economical, easier, non-toxic, and ecologically friendly. Although the production of NPs with the help of vegetable or plant extract is common, there hasn't been much discussion in the literature on applications for NPs made through green synthesis. It has been noted that heat conduction is a rare analysis in the creation of NPs with plant extract. These research results demonstrate that in addition to silver (Golli et al., 2023) gold (Piruthiviraj et al., 2016) and zinc oxide (Osuntokun et al., 2019) NPs generated through green synthesis TiO_2, and FeO NPs are also

synthesized using the help of BE. The synthesized NPs are suitable for use in photothermal therapy (PTT) applications due to the positive outcomes of hyperthermia and cytotoxicity. Biological analyses of NPs like antibacterial activity assays and fungicidal activity assays made from plant and vegetable extracts were highlighted in earlier studies (Amendola, Meneghetti, 2009, Reference Module in Chemistry, Molecular Sciences and Chemical Engineering, 2018) because of fewer chemicals. This work highlights their hyperthermia characteristics as well as biological properties. Furthermore, it has been observed in the literature that NPs coated with PDA heat up more quickly and very much than non-coated NPs. Therefore, all NPs were coated with PDA to improve the heat energy property from light energy. Moreover, produced NPs which are less toxic, cheap, safe, more affordable, and accessible and hence, they could have a positive impact on many industries, including engineering, electronics, computers, energy, and medicine.

The results also include a few unfavorable outcomes. For instance, in EDS analysis for all NPs, it may have taken the carbon element from the calcination furnace, although the mouth of each aluminum crucible is closed with aluminum foil. It has also been thought that other elements and peaks may have come from crosslets used for calcination instead of raw materials of NPs like aluminum (Al) and chrome (Cr). Moreover, it was found that the reason why the silicon (Si) ratio is too high is that the Si plates are not very well coated with NPs. The presence of Si was due to the base placed during the analysis. The presence of its own element has been proven in the analysis of each nanoparticle. Broccoli contains iron, calcium, phosphorus, magnesium, potassium, manganese, zinc, and selenium. The NPs raw material in the structure and the elements other than oxygen in the water came from broccoli. Besides, for TEM analysis of FeO NPs, it is thought that the iron nanoparticle solution may have been obtained in this way because it was coated too thick when preparing the sample for the analysis in *Figure 10(e)*. For a more accurate interpretation, TEM analysis has been studied for iron nanoparticles. Compared with the literature, the S shape observed from the VSM analysis of the produced iron oxide nanoparticle is not smooth enough and therefore it showed less magnetic properties (Niraimathee et al., 2016). Additionally, when the Ms and Hc values of all produced NPs were compared, it was observed that the highest Ms values were in iron oxide and TiO_2 NPs. It has been observed that some peaks have a higher

absorption value compared to the metal nanoparticle absorption and wavelength values in the literature, and the wavelength values have shifted to the left in UV-visible spectrophotometer data. Compared to the wavelength and absorption values of all NPs produced from broccoli in the literature, a higher absorption value was obtained in all of them. The analysis performed is important for hyperthermia analysis because nanoparticles are stimulated by selecting the appropriate wavelength in the analysis. For this reason, hyperthermia analysis was performed on metal oxide NPs using a blue laser with a wavelength of 470 nm. According to the results, it was possible to reach up to 30.6º C with the highest (4 mM AuNPs) but it is not enough for PTT application. It was thought that the reason for this was due to the fact that green synthesis was preferred. Because it has been seen in the literature that NPs produced from plant extracts by green synthesis are not used in any application field and there has not been enough research on this subject. Since it is usually produced from plant extracts and contains fewer chemicals, it is focused on biological analyses. However, it has been observed that even zinc oxide and iron oxide NPs, which do not work well in the production of heat energy from light energy, work well when coated with PDA. Also, as shown in *Figure 10(g),* according to the analysis results, it is thought that there may be an error related to zinc oxide NPs in the cell viability analysis. Since cell viability decreases as nanoparticle concentration increases (*Figure 8(g)*), as suggested for silver NPs in health studies, they should be used at low rates. Additionally, despite the filter paper's size not being extremely small, manual shredding was successful in getting the particles through the filter paper with little difficulty. When blending dried broccoli, it is essential to use filter paper with smaller holes.

Future research may aim to enhance the properties of metal oxide NPs produced from BE by enhancing their capacity to produce heat from light energy and if they are supported with photosensitizer materials, it has been thought that the results of hyperthermia may be better. Finally, our approach is that gold nanoparticles, in particular those made from BE, are a potential method and nanoparticle by further enhancing their capabilities in medical research and cancer treatment.

2.4.Conclusions and Future Works

This work shows that by using BE, it is possible to produce FeO, and TiO_2 NPs in addition to AuNPs, ZnO and AgNPs, by examining their physical, morphological, thermal, biological, and optical properties. According to the outcomes of the analyses, compared to nanoparticles produced via chemical and physical processes, these nanoparticles demonstrated high absorbance value, high cell viability, good nanostructure, and size properties, but less ability to convert light energy into heat energy. PDA-coated nanoparticles perform better than uncoated nanoparticles according to the thermal analysis of NPs@PDA. Furthermore, the best hyperthermia, cell viability, and absorbance values were provided by 4 mM AuNPs when observations from all metal oxide nanoparticles were evaluated. However, while PDA coating improves heat absorption quality, the improvement remains insufficient for PTT. It is believed that several photosensitizer additives like rose bengal can be added to further improve the capabilities of Au@PDA NPs and used in the second chapter study for PTT application because green synthesis is a cheaper, nontoxic, sustainable method than traditional methods. Moreover, it was determined that the thermal properties of AuNPs produced by green synthesis could be improved and because these particles are highly biocompatible, they could be used for various biomedical applications not only PTT but also drug delivery, imaging, and even neurostimulation. In addition to the AgNPs used for the second part, zinc oxide produced with the help of BE was also used in the electrochemical study in the third part of this thesis. Since ZnO is used as an electrode in many supercapacitor and battery applications, it was also desired to investigate how NPs produced by green synthesis exhibit properties. Thanks to this thesis, five different nanoparticles were produced with BE by green synthesis method and after physical, chemical and biological characterizations, Au NPs were selected for hyperthermia application and ZnO NPs were selected for micro-supercapacitor application. Product design was made for two different applications by combining the selected nanoparticles and novel additive manufacturing processes. Although green synthesis has many advantages, there are still difficulties in industrial production

due to its limitations. For example, quality control of particles, limitations in large-scale production and synthesis are still problems that need to be solved (Ying et al., 2022). For this reason, this thesis study on the green synthesis method and applications of nanoparticles, which require further development and have many unknowns, is expected to contribute to the existing gaps in the literature.

In future studies, it is desired to study how the mass production of the produced nanoparticles can be achieved, how to produce nanoparticles that can exhibit properties as strong as those produced by physical and chemical methods, while ensuring sustainability and environmental friendliness using green synthesis. At the same time, it is planned to perform the same characterizations by testing nanoparticle synthesis by growing plants in metal-rich organic solvents using the intracellular method instead of the extracellular method. Furthermore, because extract manufacturing is one of the most crucial steps, it is recommended to experiment with different solvents, pH, temperatures, and timeframes. After PDA coating, tests should be undertaken to detect variations not only in hyperthermia outcomes, but also in NPs size and morphology. NPs synthesized under various settings (pH, temperature, metal precursor concentration) may give diverse effects in hyperthermia. Furthermore, because PDA coating did not produce enough heat energy for PTT in future investigations, the second chapter included trials with different photothermal agents.

In summary, green synthesis is considered a sustainable method for our world, environment, humanity, and science. It is believed that nanomaterials, with their unique properties, will solve problems, develop tools, and produce products beneficial to society. Thanks to ongoing research in this field, green synthesis is expected to become a more widespread method in the future.

3. CHAPTER 3: 3D PRINTING OF GREEN SYNTHESIZED NANOPARTICLES FOR HYPERTHERMIA APPLICATIONS

3.1.Introduction

The objective of this chapter of the thesis was to print nanoparticle-added photo-thermo-responsive hydrogel with the goal of removing the drawbacks of PTT, which is a substitute for conventional cancer treatment (Ersoy et al., 2024). For printing hydrogels, (LIHAM) via N-isopropyl acrylamide (NIPAM), PEG, green synthesized gold nanoflowers (AuNPs) coated with rose bengal (RB) as a photosensitizer, and PDA as photo-initiator materials were used. The printing procedure from the meta-structure, which was designed as a 20x2 mm using 3DS Max Autodesk Software, was carried out with the microArch S240 BMF PμSL 3D printer. Five different photosensitive hydrogels were printed for physicochemical, morphological, thermal and biological analyses. This part also aims to demonstrate that kirigami LIHAM hydrogel can change shape by doping with AuNPs@PDA@RB exclusively under 565 nm laser without the need for a heater. As a result, it has been seen that the LIHAM hydrogels coated with green synthesized gold nanoflowers which was produced from the first chapter's study can be produced with a 3D printer in micro-sized and complex structures for hyperthermia applications. To have a better understanding of the study, the motivation, as well as the technologies and chemical ingredients used, were thoroughly explored.

3.1.1. Cancer Treatments

Cancer is a group of disorders characterized by abnormal cell proliferation with the ability to spread to or invade other sections of the body (Yu et al., 2024). Cancer is an increasingly common and deadly disease that can occur all over the world, with more than 100 types of cancer affecting people (Yu et al., 2024). The World Health Organization (WHO) has estimated that there were approximately 20 million new cases of cancer worldwide in 2022, with 70% of these cases occurring in low- and middle-income groups (Cuadrado et al., 2024). One study found that the most prevalent cancers were breast (2.26 million cases), lung, colorectal, prostate, non-melanoma skin, and stomach (Cuadrado et al., 2024). Cancer is a disease that can be treated based on its stage. It is caused by radiation, chemicals, dangerous foods like cigarettes and alcohol, as well as genetic and environmental factors.

Limitations of traditional treatments

Finding the appropriate treatment for each type of cancer and early diagnosis is very important. There are various methods of cancer treatment. The type of treatment you receive will be determined by the type of cancer and its stage (National Cancer Institute, Terese Winslow, 2021). Cancer is mostly treated with traditional treatments such as chemotherapy, radiation, and surgery, but it is frequently associated with debilitating side effects (Yu et al., 2024). Patients, find it difficult to go about their regular lives during chemotherapy due to side effects such as severe weight loss, nausea, hair loss, and compromised immune systems (A. Venugopal, 2024). Furthermore, because cancer cells develop immunity to chemotherapy over time, its effects weaken and destroy both healthy and malignant cells. Radiation therapy is another classic treatment approach. Although it targets the malignant spot, it also harms the surrounding organs, causing burns and exhaustion. In addition, the treatment can lead to additional malignancies and tissue damage (A. Venugopal, 2024). For these reasons, many studies have been conducted to develop alternative treatment methods that will allow patients to continue their lives with maximum energy and to completely destroy cancer without harming healthy cells.

Innovative cancer treatments

Novel therapies such as photodynamic therapy (PDT), sonodynamic therapy (SDT), and PTT have been investigated in the quest for more effective and less hazardous treatments (Yu et al., 2024). Among these, PDT and PTT have become quite widespread due to the advantages they have in recent years. In PDT, the patient is given a medicine that is triggered by light and kills cancer cells, known as a photosensitizing agent. The light can originate from a laser or another source (A. Venugopal, 2024). The medicine can be administered orally, through the skin, or intravenously, depending on where the tumor is located in the body. After 24 to 72 hours, the medicine will separate from healthy cells but remain in cancer cells. The tumor is subsequently subjected to light, depending on its location. The light induces cancer cells containing the photosensitizer to generate oxygen, which kills the cancer cells. Most patients are treated as outpatients and often return home the same evening. PTT is another approach for reducing the death rate of healthy cells (A. Venugopal, 2024). PTT is a localized thermal therapy that destroys tumor cells by heating them to 40-44° C with a photothermal converter agent that converts light energy into heat energy. It is a promising method that causes minimal collateral damage to healthy tissues (A. Venugopal, 2024).

3.1.2. Photothermal Therapy

PTT is also called thermal therapy or hyperthermia therapy (A. Venugopal, 2024). Hyperthermia is a treatment for cancer or other diseases that involves raising the body's temperature to 40°C to 44°C to eliminate malignant cells (Yu et al., 2024). It is a therapeutic procedure that has gained popularity due to its low toxicity, noninvasiveness, simplicity, and ability to treat tumors in regions where surgical resection may be ineffective (Yu et al., 2024). Tumors are more sensitive to heat than healthy cells, making hyperthermia an effective therapy option (Yu et al., 2024). Hyperthermia-induced cell death can occur through a variety of mechanisms, including membrane breakdown, protein denaturation, and the formation of reactive oxygen species, which leads to necrosis (death of cells that are damaged to the point of being unable to continue living activities) and apoptosis (built dying of cells) (Yu et al., 2024). If it's necessary to look more closely at the

mechanism of treating hyperthermia, this method leverages the photothermal effect, which is when the photothermal agent absorbs photons from laser radiation, increases its energy, and changes from the basal monolinear state to the unstable excited monolinear state before returning to the initial state through radiationless relaxation of vibration (photothermal particles collide with surrounding material molecules and release energy), which raises the temperature (Yu et al., 2024).

However, the success of PTT is vitally dependent on the photothermal agents, particularly the nanoscale versions, which are capable of producing significant thermal energy in response to light irradiation. Noble metal NPs have recently emerged as the leaders in this field, gaining worldwide interest for their large specific surface area and unusual optical, electrical, and catalytic capabilities (Yu et al., 2024). Noble metals are used in PTT because of their strong surface plasmon resonance, which provides to the successful absorption of certain wavelengths of light in the NIR spectrum and subsequent conversion into thermal energy, resulting in localized thermal therapies that are efficient for tumor destruction (Yu et al., 2024). Nanomaterials for clinical applications should be harmless, stable, hydrophilic, have a long blood flow time, selectively target diseased cells, tissues, have minimal aggregation, and have optimal features for high buildup at the tumor site while avoiding macrophages of the reticuloendothelial system (RES) (Fang, Chen, 2013). As plasmonic excitation element metals, noble metal nanoparticles such as Au and Ag are widely used in this application. In addition, magnetic field-guided Fe metal nanoparticles can also be used for hyperthermia. In this work, the hyperthermia potential of gold nanoflower NPs produced in the first part was investigated (Yu et al., 2024). Other photosensitive materials used for hyperthermia application in this thesis are also mentioned below.

3.1.3. Hyperthermia Ink Components

3.1.3.1.Gold nanoflowers

Although damage to healthy cells is less than that of chemotherapy or other therapies, PTT is not common due to many unresolved disadvantages, such as capillary leak syndrome, itching on the skin, redness, burns, absorption-scattering

of light, and treatment ineffective in deep. These factors indicate the potential of using transition metal oxide NPs to mitigate light therapy's drawbacks (Rapp, DeForest, 2020). AuNPs are ideal photothermal agents because they have tunable optical properties in the NIR and IR regions. Also, AuNPs are biocompatible, absorb light efficiently, easy to synthesize, non-toxic, inherent localized plasmonic resonance (LPR) properties and stable (Fang, Chen, 2013). However, numerous parameters influence the performance of AuNPs. For example, because the absorbance range varies with NPs size and shape, so does the light source. For instance, photothermal effects from gold nanospheres irradiated with a 515 nm laser were greatest for nanospheres ranging in size from 20 to 40 nm. Additionally, NPs must be smaller than 10 nm to pass through cells. In this thesis, hyperthermia performance of gold nanoflowers produced with BE using green synthesis method was investigated. Since it was aimed to improve the hyperthermia analysis results obtained in the first part, additives materials were selected for this purpose.

3.1.3.2.Polydopamine

PDA is bioadhesive, biocompatible, and biodegradable, with a high photothermal conversion efficiency (Li et al., 2021a). Moreover, it has demonstrated tremendous potential in biomedical domains, owing to its distinct physicochemical features, good drug binding capacity, varied adhesion ability, and pH sensitivity (Li et al., 2021a). PDA is frequently used as a photothermal agent because of its excellent photo-initiator properties and biodegradability compared to other photothermal agents, and it can decay in the human body (Huang et al., 2023). NIR light is converted into heat by PDA, which kills cancer cells both in vitro and in vivo (Xu et al., 2022). In the other study, it was seen to treat cancerous tissues with a scaffold produced by 3D printing from NPs and PDA with hydrogels (Qu et al., 2022). In this thesis study, as seen in the hypethermia analysis results in the first part (*Figure 7(e)*), it was shown that AuNPs@PDA particles conjugated with PDA can produce more heat energy using the light source. For this reason, AuNPs@PDA particles were used in the second part. However, since it was thought that the feature still needed to be improved, different additives were added.

3.1.3.3.Rose Bengal

AuNPs have been coated with various photosensitizer materials to increase their thermal absorbance properties for biomedical applications. RB, is a food additive and low-cost photosensitizer, utilized to achieve the combined antibacterial effects of PTT and PDT. Under 550 nm visible light irradiation, RB can be transformed to the excited triplet state, and energy transfer can be used to produce reactive oxygen species (ROS). However, RB's water solubility prevents it from being immediately integrated into the hydrogel (Li et al., 2021b). As a result, in this study, AuNPs@PDA@RB particles were formed by conjugating them with AuNPs@PDA nanoparticles. In this method, the goal was to improve hyperthermia performance while also making the NPs non-toxic. It was observed that RB and Au nanorods could produce oxygen efficiently in green light with 532 nm, while photothermal efficiency was high in 810 nm red light according to the previous research (Wang et al., 2013, Wang et al., 2014). Furthermore, no studies on RB, PDA, or gold nanoparticle coating have been identified in the literature. Moreover, hydrogel was used in this study to attach, send or provide targeted delivery of the produced nanoparticles to the cancerous area in the human body.

3.1.3.4.NIPAM

Thermoreactive hydrogels made from thermosensitive polymers have been extensively researched in the literature (Ersoy et al., 2024, Haq et al., 2017). These polymers can be negatively as well as positively thermosensitive. The first has a lower critical solution temperature (LCST), whereas the second has a higher critical solution temperature (UCST). LCST polymers shrink when the temperature rises above their critical temperature, whereas UCST polymers behave similarly when the temperature drops. More exactly, around the critical temperature, the polymer in solution undergoes a phase change from soluble to insoluble (Reference Module in Chemistry, Molecular Sciences and Chemical Engineering, 2018, Haq et al., 2017). However, LCST polymers are better suited to biological applications since they can release the chemical at human body temperature. Thermoresponsive events occur due to a precise balance of hydrophobic and hydrophilic segments in the polymer's monomer (Haq et al., 2017). The interaction between polymer segments

and water changes with slight temperature changes due to a shift in hydrophilic and hydrophobic forces. Although copolymers, such as triblock copolymers, have been known to be thermosensitive polymers, they have not received substantial research due to their difficulties in manufacturing. The monomer structure in thermosensitive homopolymers is typically hydrophilic, with some hydrophobic groups such as methyl, ethyl, and propyl (Haq et al., 2017). pNIPAM's monomer structure comprises of amide (-CONH-) and propyl (-$CH(CH_3)_2$) and when the temperature is low, water molecules dissolve the hydrophilic amide group, which dissolves the polymer (Haq et al., 2017). When the temperature rises, the hydrogen bond weakens, and the contacts between the hydrophobic propyl groups become stronger. This finally leads to the leakage of water from the structure (Haq et al., 2017). Simultaneously, the polymer chains collapse, resulting in a volume phase change (Haq et al., 2017). The pNIPAM hydrogel is not an exception to the general rule that hydrogels have restricted mechanical properties. The low thermoreactivity of the pNIPAM hydrogel significantly complicates the issue. Natural pNIPAM hydrogels react to changes in the outside temperature very slowly. The main cause of this is the development of an impermeable surface structure that prevents water from escaping during the hydrogel wrinkling process (Haq et al., 2017). Pore-forming NPs and PEG additives can be added during gel formation to boost the reaction rate (Haq et al., 2017).

The use of NPs with pNIPAM (Moradi et al., 2022, Paunović et al., 2022) is quite common as it reduces the disadvantages such as gold, graphene, silver, xanthan, and iron on heat conduction applications in the literature (Ersoy et al., 2024). This thermo-responsive polymer is normally toxic and must be used in combination with other non-toxic products to be used in biological applications. By adding various biodegradable monomers and/or crosslinkers or natural polymers like poly (amino acids), polysaccharides, and synthetic polymers like poly(esters), poly(caprolactone), and PEG, various methods for the preparation of biodegradable NIPAM-based hydrogels are being investigated (Cooperstein, Canavan, 2013, Tang, Okano, 2014). In this thesis, PEG, AuNPs@PDA@RB nanoparticles were added to the NIPAM solution in order to improve the properties of the hydrogel. Furthermore, hydrogel production has been carried out with many polymer production techniques. In comparison to traditional 2D fabrication techniques,

using three-dimensional printing (3DP) to manufacture hydrogel objects may provide unparalleled flexibility in achieving the intended complexity composition, fully tapping into the special thermo-sensitivity property in reaction to environmental changes, arrangement, and precision in medicine applications such as skin patches, implants, vessels, and artificial organs (Bilici et al., 2022).

3.1.4. 3D Printing of Hydrogels

Additive manufacturing (AM), often known as 3DP, is a new manufacturing technology that creates products layer by layer (Graça et al., 2024). First, the model to be printed is created using a CAD application and saved as an STL (stereolithography) file type. STL is a file format widely used in 3D printing and computer-aided design. The printing material is then selected based on the 3D printing process that will be employed. After setting printing parameters, the model is sliced using appropriate software for the device and printed (Liu et al., 2023).

3.1.4.1.Types of 3D printer

There are several types of 3DP, including powder-based printing (binder jet printing), extrusion-based printing (fused deposition modeling (FDM) and hydrogel-forming extrusion (HFE), stereolithographic printing (SLA), selective laser sintering printing (SLS), inkjet printing (IJ), and digital light processing (DLP). There are also three types of 3D printer ink: solid based, powder based, and liquid based (Graça et al., 2024). Solid-based ink can be printed using the FDM method, whereas powder-based ink can be printed using the SLS method. Liquid ink may be printed using SLA and DLP technology (Graça et al., 2024). The SLA technology employs an oscillating mirror system to control UV laser (355 nm or 405 nm) point scanning cross-linking to cure resin materials, resulting in improved mechanical qualities but less suitable material, poor processing precision, and sluggish processing speed. Furthermore, incompletely cross-linked resins are poisonous. As a result, a digital mirror device with high precision and speed of manufacturing, as well as a DLP system based on photosensitive polymer liquid,

were built using SLA technology (Liu et al., 2023). In contrast to SLA, which uses a point-by-point exposure, DLP technology uses a light source to illuminate each layer at the same time. In a DLP system, the photon source is lighted from below the resin bath, while the construction platform is immersed from above; this allows for 3D production with reduced resin volume use. The cured layer is not in direct contact with air, making it less sensitive to oxygen inhibition (Bagheri, Jin, 2019).

3.1.4.2.Microstereolithography (μSLA) printer

Microstereolithography (μSLA) enhances the possibilities of DLP. Its primary purpose is to improve resolution while retaining the ability to manufacture larger or more components (Graça et al., 2024). This is accomplished by inserting a high-precision lens between the projector and the resin tub, which allows the construction platform to move in the XY plane (Graça et al., 2024). This novel approach uses a top-down methodology to allow for repeated imaging passes while preserving excellent resolution. The μSLA technology can reach an XY resolution of roughly 2 μm, with minimum feature sizes as tiny as 10 μm and dimensional tolerances up to 10 μm (Graça et al., 2024). These approaches can also provide high resolution with small feature sizes (micrometers or less). To that aim, this technology has opened up new possibilities in a variety of industries, including microfluidics, biomedical devices, soft robotics, surgery, tissue engineering, dentistry, and drug delivery (Liu et al., 2023). In this thesis, since a small-sized and complex-shaped printing will be made on the human body, a projection micro-stereolithography (PμSL) printer (S240, BMF, Shenzhen, China), which utilized a UV projector (405 nm) as the light source (Chen et al., 2022), was selected. First of all, the hydrogel making mechanism of the device and the hydrogel design should be mentioned.

3.1.4.3.Photopolymerization

The technique for 3D photopolymerization is to use liquid monomers/oligomers that can be cured/photopolymerized and create thermosets when exposed to a light source with a specific wavelength (Yu et al., 2020). A photoinitiator is required to transform photolytic energy into reactive species capable of driving chain

development through radical or cationic mechanisms. However, due to the difficulties of continuous UV light exposure, such as shrinkage and polymer property degradation, 3D photopolymerization techniques must be created (Bagheri, Jin, 2019).

3.1.4.4.Design of hydrogels

pNIPAM was used in a study that looked into kirigami design in the literature. As the temperature climbs over the LCST, the hydrogel's hydrophilic to hydrophobic properties change, causing isotropic shrinkage. By adding monomers or functional particles to the isopropylacrylamide monomer, the structures that are built exhibit reactions to several stimuli (Zhang, Sitti, 2024). Such changeable kirigami meta-structures have great promise for advancing fundamental small-scale meta-structure research as well as microscale soft robots, wearables, drug delivery, miniature robotics, and medical device design and production (Zhang, Sitti, 2024). Kirigami structures make excellent building blocks for reconfigurable meta-structures based on timed cuts made to thin sheets or films. Simulations using thermo-responsive materials can reveal the characteristics of thermal shape transformation (Zhang et al., 2021). The thermo-responsive polymer contracts when heated and expands when cooled because of its kirigami structure. It is believed that kirigami design has enormous promise because of this movement change in response to temperature, particularly in drug release and cancer treatment. In previous studies, the mechanism and the drawing of the kirigami shape were explained in detail (Zhang et al., 2021, Zhang, Sitti, 2024) in *Figure 13*. Printing NIPAM material with a 3D printer is thought to be quite lacking in the literature. In addition, no research on RB, PDA, or gold nanoparticle coating has been found in the literature. Moreover, it is believed that scientific research is deficient regarding the applications of nanoparticles made using green synthesis. This study investigated to demonstrate that it may be applied to temperature settings in addition to its biological benefits.

For these reasons, this study aims to show that the LIHAM material synthesized using NIPAM and PEG was printed in a kirigami metastructure via a PμSL printer by coating AuNPs@PDA@RB. The kirigami structure changes shape by absorbing

the correct light source and generating heat without using a heater (*Figure 13*). Since printing kirigami structures at micron sizes is quite difficult with traditional 3D printer methods, a PμSL printer was made from a hydrogel solution with high printability, flexibility, and rheological properties. The AuNPs, RB, and PDA were added to the LIHAM solution to investigate printability. Furthermore, the study intends to explore the impacts of LIHAM, AuNPs, PDA, and RB, as well as the characteristics they contribute to the hydrogel, using analyses that were performed to compare the physicochemical, morphological, and thermal properties of newly printed photoresponsive metastructures.

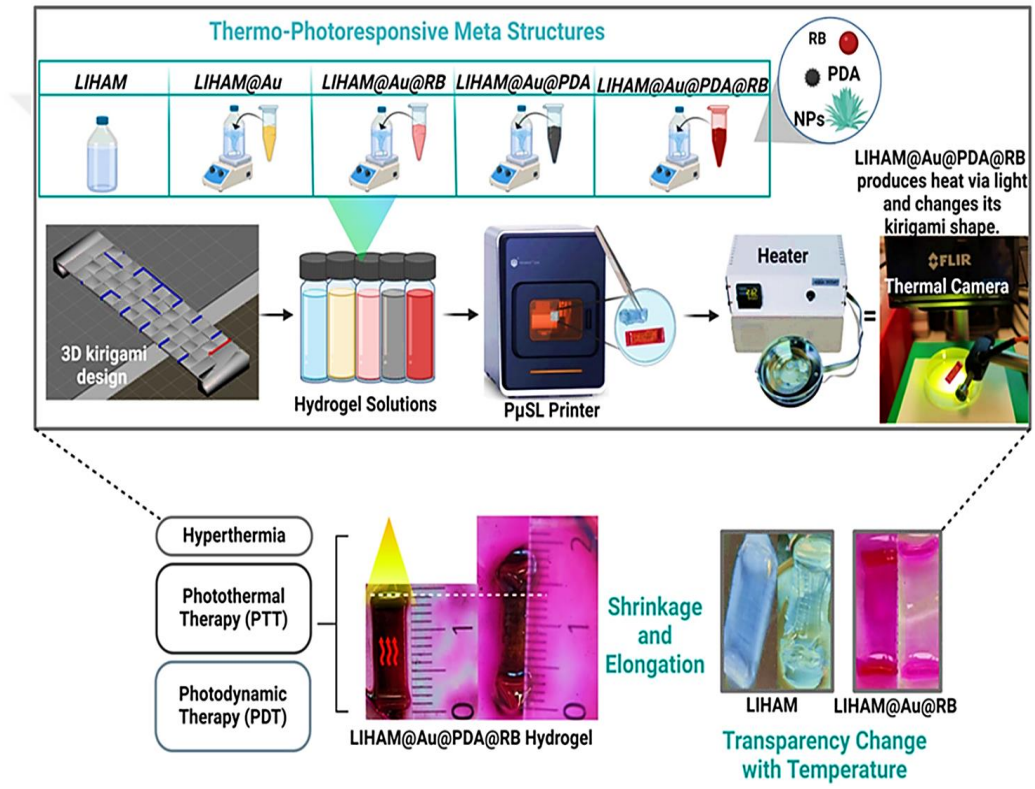


Figure 13: Printing stage of kirigami meta-structure design with PμSL 3D printer (Ersoy et al., 2024) [BioRender].

3.2.Materials and Method

3.2.1. Materials

N-Isopropylacrylamide (H_2C=CHCONHCH(CH_3)$_2$, CAS Number: 2210-25-5) as a monomer; lithium phenyl-2,4,6-trimethylbenzoylphosphinate (LAP/TPO-Li, $C_{16}H_{16}LiO3P$, CAS Number: 85073-19-4) as a photoinitiator; acrylamide (AM, CH2=CHCONH2, CAS Number: 79-06-1) as a monomer; 2-Hydroxyethyl methacrylate (HEMA, CH2=C(CH3)COOCH2CH2OH, CAS Number: 868-77-9) as a monomer; Poly(ethylene glycol) diacrylate (PEGDA, CAS Number: 26570-48-9) as a crosslinker and PEG were used as a pore-forming agent from Sigma-Aldrich. DW was used as a solvent for producing LIHAM solution (Zhang et al., 2023b). 100 nm AuNPs were synthesized via the green synthesis method with the help of BE and coated with polydopamine in our previous chapter. RB ($C_{20}H_2Cl_4I_4Na_2O_5$, CAS Number: 632-69-9) was used by Sigma-Aldrich as a photosensitizer and tissue glue for coating AuNPs@PDA (Ersoy et al., 2024).

3.2.2. Synthesis of LIHAM

As done in the previous study (Zhang et al., 2023b, Zhang et al., 2023a), the material ratios are NIPAM: TPO-Li: AM: HEMA: PEGDA: PEG: DW weight by weight, respectively 500:10:29: 29:150:300:4500. Firstly, NIPAM and AM were weighed and added in powder form to a beaker, and then 300 microliters of HEMA were added to it. PEGDA and PEG were weighed in a separate beaker and mixed by adding DW without forming a phase. The second prepared solution (PEGDA, PEG, and DW-liquid solution) was added to the first prepared solution (NIPAM, AM, and HEMA) and mixed for a few minutes until dissolved with the help of an ultrasonic sonicator. Finally, TPO-Li was added to it and mixed again with the help of the sonicator. The prepared final product was placed in a glass container and covered with aluminum foil to prevent exposure to light (Ersoy et al., 2024). All the processes can be seen in *Figure 14(a).*

3.2.3. Conjugated of Gold Nanoflowers@Polydopamine with Rose Bengal

In *Figures 4* and *5*, how gold nanoflowers were produced by the green synthesis method using BE was explained with schematically in the first chapter. Firstly, the dried broccoli thrown into pure water was mixed with heat and then filtered with the help of filter paper. Then, the reaction was carried out for 24 hours by adding gold (III) chloride trihydrate to BE and pure water. AuNPs@PDA NPs were obtained by reacting the gold nanoflowers obtained after drying and heat treatments with dopamine chloride. In this research experiment procedure, 100-nm-sized Au NPs (4 mM) were coated with PDA again (*Figure 6*). First, NPs:DMSO was prepared at a ratio of 1:10 and sonicated under 150 W for 15 minutes in a beaker. Next, NPs:TRIS buffer was added at a ratio of 1:19, and dopamine was added at a ratio of 1:1 for dopamine hydrochloride:NPs. After all the ingredients were added, the mixture was mixed in a magnetic stirrer at 1000 rpm for 24 hours. The NPs@PDA solution was then centrifuged at 8000 rpm for 10 minutes and twice cleaned with double DW to remove excess unconjugated PDA. Then, a 10 mM RB solution was prepared with 1 µl of DW for conjugation. The prepared RB solution was added to 1 ml of AuNPs@PDA solution. Then it was kept at 30^{o} C for 5 hours . After 5 hours, it was centrifuged at 8000 rpm for 5 minutes, and the process was repeated twice times with double DW to remove unconjugated RB (Ersoy et al., 2024). The AuNPs@PDA@RB coating experimental steps are shown in *Figure 14(b).*

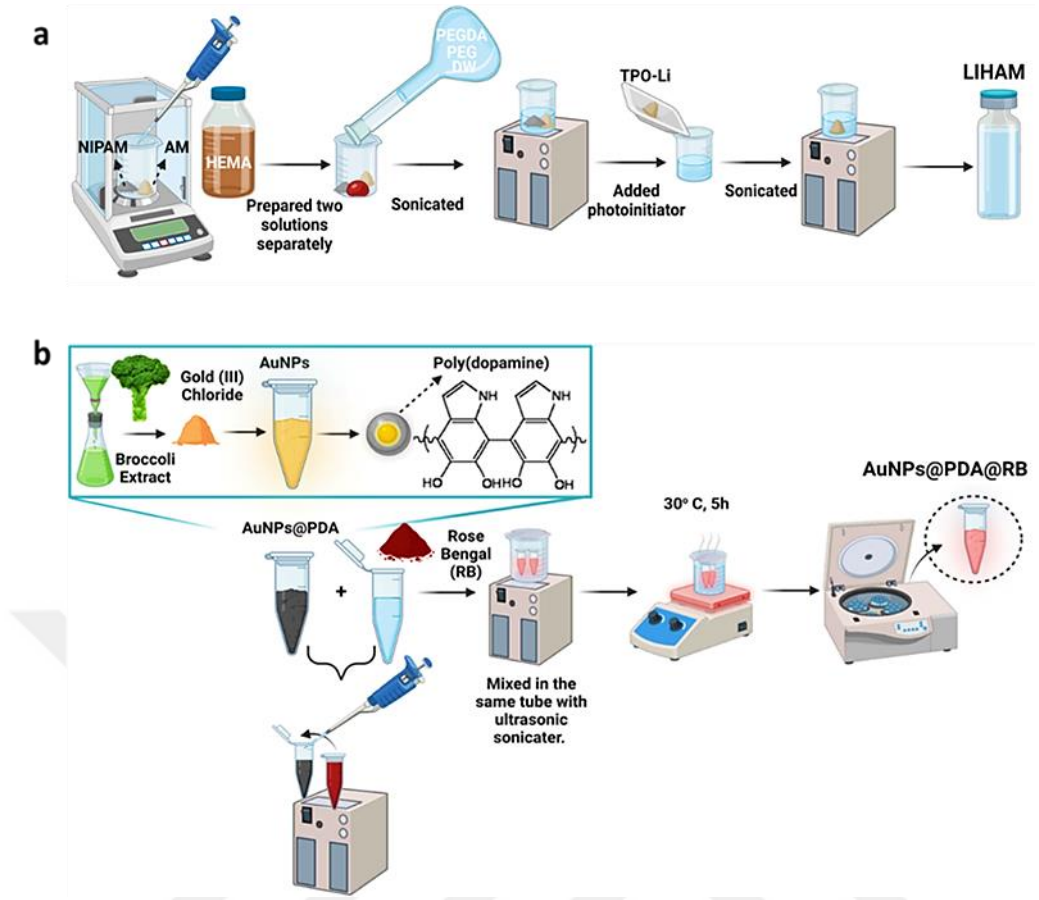


Figure 14: a Synthesis steps of LIHAM solutions and **b** Experimental steps of conjugated AuNPs@PDA with RB [BioRender] (Ersoy et al., 2024).

3.2.4. Printing of LIHAM

The kirigami meta structure model was drawn in the previous study with 3DS MAX Autodesk Software in dimensions of 20x2 mm. Then, this file was transformed into dimensions suitable for the BMF S240 PμSL 3D-printer chamber, according to x-y-z coordinates, with the help of ChitoBox Software (Zhang et al., 2021).

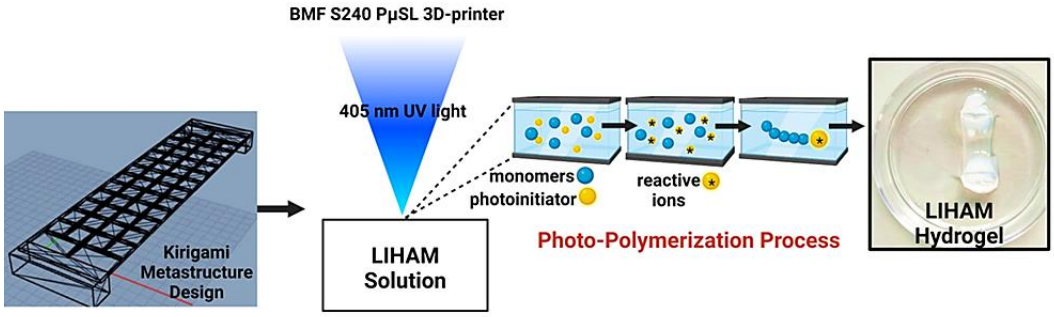


Figure 15: Photo-polymerization steps of hydrogels [BioRender] (Ersoy et al., 2024).

Then, with the help of Bulk Utility Rename Software, 200 different images were renamed with kirigami slices and turned into files for the printer in *Figure 15*. As seen in Table 1 and Table 2; pure LIHAM hydrogel was printed at different exposure times, intensity of light values, and different solution trials. In *Figure 16*, the best result was observed at 8-6-6-6-4 seconds exposure time and 60 lumens in Table 1 (Experiment 3); and in *Figure 16,* the best solution ratio result was as prepared in the previous study in Table 2 (Experiment a). For this reason, the prepared file was added to the printer computer, and the appropriate parameters for the printer, exposure time of 8-6-6-6-4 seconds and intensity of light 60 lumens, mode single were set. Also, five different hydrogels in this study were printed in BMF S240 according to these parameters (Ersoy et al., 2024).

Table 1: Printer exposure times and intensity of light changing of printing parameters for finding the best meta structure.

Experiments	Exp. time for layer (second)	Intensity of light (lumen)	+/-
1	4-2-2-2-2	50	-
2	8-6-6-6-4	50	+
3	8-6-6-6-4	60	+
4	10-8-8-8-5	60	-
5	12-10-10-10-6	60	-

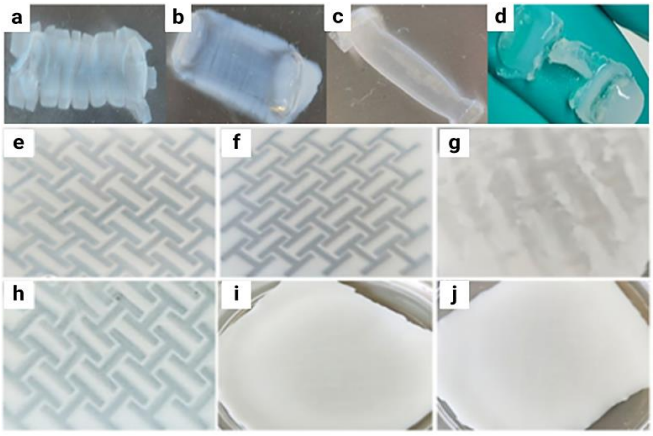


Figure 16: LIHAM kirigami hydrogels according to the printer time and intensity parameters for Exp.2 **a**, Exp.3 **b**, Exp.4 **c**, and Exp.5 **d** at RT. Furthermore, LIHAM hydrogels images according to the solution parameters after printing with CELLINK and Volumetric introduce Lumen X 3D bioprinter to Exp.a for 10 seconds **e**, Exp.a for 20 seconds **f,** Exp.b for 20 seconds **g**, Exp.c for 20 seconds **h**, Exp.d for 20 seconds **i**, and Exp.e for 20 seconds **j** at RT [BioRender].

Table 2: Changing solution ingredients like photo-initiator and monomers for finding the best ratio to the printing of hydrogels (X= times).

Experiments	Photoinitiator (TPO-Li)	Monomer (NIPAM)	Monomers (AM-HEMA)
a	same	same	same
b	same	2X	same
c	3X	same	same
d	2X	2X	same
e	2X	2X	2X

When Table 1 and *Figure 16* are examined together, unfortunately, material in experiment 1 could not be removed from the printer properly because it was very soft hydrogel. In *Figure 16(b),* experiment 3 was better and a shape difference was observed when compared to other hydrogels. If the intensity of light and the exposure printing time were increased too much, this has been shown to damage the hydrogel, reducing its flexibility, and distorting the kirigami shape in *Figure 16(c)* and *(d)*. Although experiments 2 and 3 in Table 1 produced smooth hydrogels in kirigami shape, it was seen in *Figure 16(b)* that the best result was given by experiment 3, where the intensity of light was 60 lumens. As exposure time and intensity of light increases, printing time increases for the 1st, 4th, 10th, 25th, and 160th layers, and the overall time was decreased (Ersoy et al., 2024).

The printing was done by changing the parameters to prove that the best solution result is in the proportions written in the experiment section. According to *Figure 16(f)*, the best result is experimenting with a has been printed for 20 seconds. It has been observed that the higher the base exposure time, the thicker and stiffer the LIHAM hydrogel. The power level of the printer was %80, the body exposure time was 10 or 20 seconds, and the base exposure time factor was 2X. The printed chainmail meta structure had dimensions of 28.99 mm x 28.97 mm x 2.25 mm for the Table 2 experimental setup. Based on the experimental findings shown in Tables 1 and 2, it has been observed that as the exposure time increases, complex structures can be printed in more detail, such as kirigami or chainmail. However, the chemical structure of the hydrogel that was exposed to high-intensity light for too long deteriorated and was damaged, so its shape and properties were not as desired. For this reason, the most appropriate time and lumen value were determined, and the main experiments of the study were started (Ersoy et al., 2024).

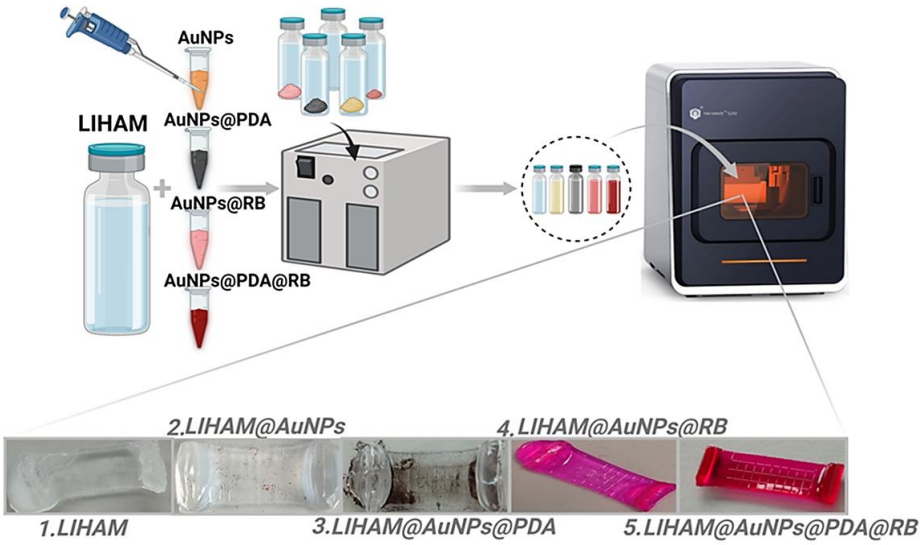


Figure 17: Five different hydrogels according to the photoinitiators [BioRender] (Ersoy et al., 2024).

As seen in *Figure 17*, five different LIHAM solutions were prepared to examine the effects and properties of gold nanoflowers, RB, and PDA photosensitizer additives. Firstly, a 225 ml LIHAM solution was prepared according to the best chemical ratio. Then, this pure LIHAM solution was distributed into five different 45 ml glass jars. The first is just pure LIHAM hydrogel. Secondly, AuNPs were added to the LIHAM solution, and the effect of gold nanoflowers wanted to be understood. Then, thirdly, AuNPs@PDA was added to the LIHAM solution to see the PDA benefit. Additionally, RB benefits were seen by adding AuNPs@RB to the fourth LIHAM solution. All additives AuNPs@PDA@RB were added to the fifth LIHAM solution. Thus, the analyses aimed to determine the best hydrogel content by comparing morphological, thermal, chemical, physical, biological, and printability aspects. PDA, AuNPs, and RB additives added to LIHAM solutions were mixed with glass bottles using an ultrasonic sonicator for more than 1 hour to mix homogeneously. After the hydrogels were printed with the BMF S240 printer, they were placed in small petri dishes, dripping DW on them, and covered with paraffin. They were stored for analysis at +4^{o} C (Ersoy et al., 2024).

3.2.5. Characterization of Kirigami Meta Structure Hydrogels

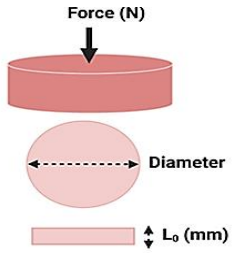
The characterization of 3D printed kirigami meta structure hydrogels is divided into four groups as physicochemical, morphological, thermal, and biological

characterization. The characterization methods examined in the four groups are explained below, respectively.

Rheological Measurements

A Discovery Hybrid Rheometer HR20 equipped with a TA Instrument and a Peltier stainless steel parallel plate with a 20 mm diameter were used for the rheological analyses. While rheological analyzes were carried out, hydrogels were printed in circular shapes with a 3D printer. Their lengths and diameters are added in the table in *Figure 18* (Ersoy et al., 2024). Throughout all measurements, a low viscosity was utilized as a solvent trap, and the gap spacing was fixed to 0.5 mm. To determine the correct value in the amplitude/angular frequency analysis, MPa/oscillation strain analysis was first performed (*Figure 19*). In order to examine force amplitude/angular frequency, with 5 points per decade were obtained for $\omega = 10^{-1}$ to 10^{2} (rad s^{-1}), strain from 0.1 to 100, and shear rate from 0.01 to 100 (1/s) at 20° C. Viscoelastic behaviors (amplitude sweep test, frequency sweep test, and temperature sweep test) and compression analyses of hydrogels were examined with the help of rheological measurements. In the compression analysis, 40.0 mm parallel plate and Peltier plate stainless steel were used. Again, the temperature was determined as 25° C, soak time 180 seconds, duration 300 seconds, strain 1%, and angular frequency 10 rad/s (Ersoy et al., 2024).





Area of Hydrogels $A = \frac{\pi d^2}{4}$

Stress $\sigma = \frac{F}{A}$

Strain $\varepsilon = \frac{dL}{L}$

Elastic Modulus (E) = (stress)/strain

Sample Name	Initial Length, L_0(mm)	Diameter(mm)
LIHAM	2.8361	10
LIHAM@AuNPs	2.9989	10
LIHAM@AuNPs@PDA	7.2627	15
LIHAM@AuNPs@RB	3.3436	10
LIHAM@AuNPs@PDA@RB	3.922	10

Figure 18: Rheology analyses for compression test [BioRender] (Ersoy et al., 2024).

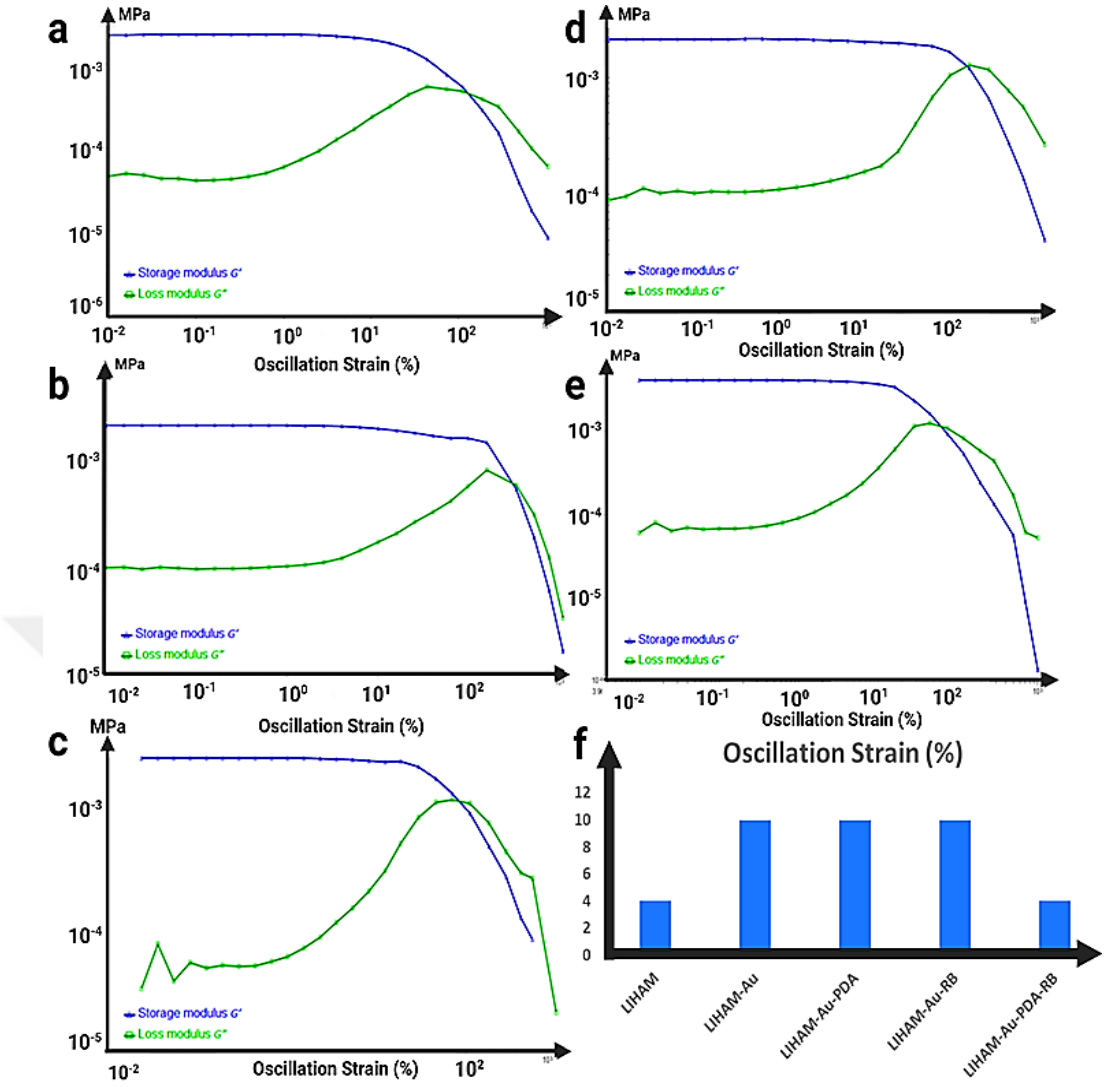


Figure 19: Oscillation strain values of the hydrogels before examining the viscoelastic behaviors [BioRender] (Ersoy et al., 2024).

Osmotic Swelling Response

The hydrogels were submerged in DW solution at RT for swelling experiments, and the solutions were changed every other day. The specimens were weighed after equilibrium swelling in DW. Following the recording of the dry weight and swelling ratio (Q_w) was computed using the formula **(1)**:

$$Qw = \frac{Ws}{Wd} \qquad (1)$$

where W_s and W_d are the gel sample's equilibrium swollen and dried weights, respectively (Bilici et al., 2022).

FTIR

FTIR was used to confirm the chemical functional groups in molecules that vibrate when exposed to light wavelengths (Ersoy et al., 2024) of the produced hydrogels. With the TENSOR II FTIR Platinum ATR Routine Spectrometer from Bruker Optics, the spectroscopic investigation was carried out over a wide wavenumber range of 500-4000 cm^{-1}.

Enzymatic Degradation

The hydrogels' enzymatic degradation tests were carried out in Dulbecco's Phosphate Buffered Saline (DPBS) with no calcium, and no magnesium from Gibco at a collagenase type I from Gibco concentration of 1 mg/ml^{-1}. The samples, which weighed almost 0.1 g, were immersed in 3 ml of collagenase solution at 37° C. Their weights were taken at daily intervals, and the weight loss was calculated using the formula below **(2)**:

$$\boldsymbol{Weight\ Loss}\ \% = \frac{(\boldsymbol{W0}-\boldsymbol{Wt})}{\boldsymbol{W0}}\boldsymbol{x}100 \qquad \textbf{(2)}$$

where W_o and W_t are the weight of hydrogel samples at time 0 and at time t, respectively (Bilici et al., 2022).

SEM

Using a ZEISS Sigma 300 VP SEM, the morphological structures of printed and molded specimens were identified by ImageJ software. The specimens were vacuum-coated with Au after being freeze-dried initially. At a working distance of 15–36 mm and an accelerating voltage of 3 kV. The EDS method from Thermo Scientific was used to determine the elemental composition of the nanoparticles. When the particles were 1 μm in size, the region where the particles were dense was selected, and EDS analysis was performed according to the kV value of each element. Moreover, according to the EDS data, the Si ratio was high because the number of nanoparticles was low (Ersoy et al., 2024).

TEM

Transmission Electron Microscopy (TEM) was performed with a Philips CM200 microscope (300 kV, LaB6 cathode). 1 μl of nanoparticle suspension was deposited

on a copper grid (Plano) and slowly air-dried. With a TVIPS TemCam-F216 CMOS camera, pictures were captured. Since all LIHAM hydrogels were too large and thick for TEM analysis, five different LIHAM solutions were used in TEM analysis by dropping 1 drop onto the grid instead of the hydrogel. The samples were observed by TEM under 200 kV accelerating voltages. Imaging was simple for materials with electron densities noticeably higher than formless carbon (Ersoy et al., 2024).

Differential Scanning Calorimetry (DSC) Analysis

DSC is a thermal analysis tool that monitors temperature changes and alterations in a sample's physical properties over time. The TA Discovery DSC 2500 device was for hydrogel analysis. The sample should be positioned as securely as possible on the container's bottom. The material is pressed into the aluminum container before going into the oven. The minimum and maximum sample weights should be 7 mg and 10 mg, respectively (Ersoy et al., 2024).

Hyperthermia

For the thermal analysis, the degree of warming of the hydrogels was observed for 30 minutes using M565F3 nm (yellowish green) light at 565 nm. In addition, for the additives, 20-minute measurements were taken on M625F2, M565F3 and M470F3 laser sources to determine which wavelength of laser light the particles absorbed better and converted into heat energy. Using a thermal infrared camera (ETS320, FLIR Systems, OR, USA), thermal pictures and temperature data were captured with the led current of 700 mA according to the hyperthermia analysis results of AuNPs, PDA, and RB photosensitizer additives (Lee et al., 2023). Hydrogels with DW were put in the small petri dish and every 10 minutes, the images on the camera screenshot, and the production of heat energy from light energy were observed for each hydrogel for 30 minutes. AuNPs, AuNPs@PDA, AuNPs@RB, and AuNPs@PDA@RB solutions were dripped 100 microliters on all doped hydrogels for hyperthermia analysis and analysis was performed after half an hour. Based on results from the UV-visible spectrophotometer, the thermal analysis measured the degree of warming of the nanoparticles for 20 minutes using M470F3 nm (blue-violet) light at 470 nm and a FLIR thermal camera with a lead current of 1000 mA. Before the hyperthermia analysis, 2 ml of ethanol was added

to the nanoparticle powders in the capsules, and they were sonicated for 1 minute using a sonicator. No ethanol was added; the NPs@PDA solution was left in its original state. The camera's photos were captured every five minutes, and for twenty minutes, each nanoparticle's conversion of light energy into heat energy was tracked (Ersoy et al., 2024).

Luciferase-based cytotoxicity assay

For the cytotoxicity experiment, BJ cells, which are fibroblasts generated from skin, were employed. The base medium for this cell line is the ATCC-formulated Eagle's Minimum Essential media, Catalog No. 30-2003. To generate the complete growth medium, mix the fetal bovine serum with the basic medium until it reaches a final concentration of 10% (Ersoy et al., 2024). For the cytotoxicity analysis, each group (n = 8) employed 8 distinct samples. To produce a cytotoxicity medium, 10% DMSO solution was added to the negative control, and only BJ fibroblast was planted in the well as the positive control. The well was then incubated for two days at 37° C in a 5% CO_2 and 95% air-humidified environment. Hydrogels were cultivated with BJ fibroblast cells to investigate their cytotoxicity (Ersoy et al., 2024).

3.3.Results and Discussion

3.3.1. Physicochemical Characterizations

These characterizations consist of rheological measurements which are viscoelastic behaviors (amplitude sweep- angular frequency sweep- temperature sweep) and compression test, osmotic swelling response, FTIR and enzymatic degradation.

3.3.1.1.Rheological measurements

Compression

Figure 18 shows the calculations and hydrogel values used in the compression analysis. In compression analysis, the samples were pressed in a cylindrical shape so that the force could be applied equally to all parts of the sample. The diameter and initial height parameters of the hydrogels are shown in the table in *Figure 18.* The stress/strain curve and Young's modulus graphs were drawn from the data obtained as a result of the analysis.

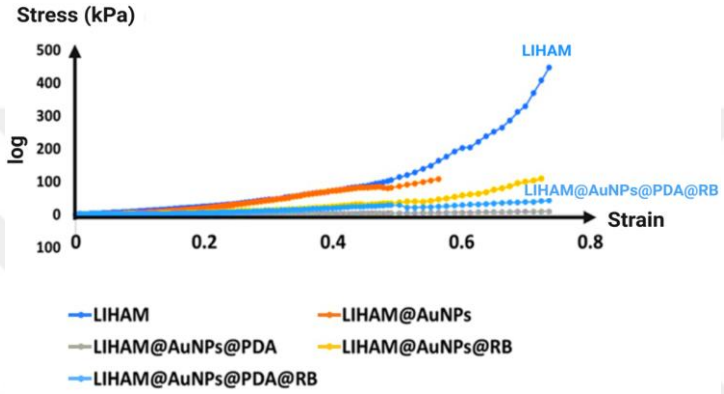


Figure 20: Stress/Strain curve for five different hydrogels (Ersoy et al., 2024).

The stress/strain diagram in *Figure 20* examined five different hydrogels. Except for LIHAM@AuNPs, the strain values of the other hydrogels were found to be close to each other. All the curves were found to be suitable for polymer behavior. Additionally, the area under the stress/strain graph showed the absorbed energy. Although the LIHAM hydrogel moved into the plastic deformation region, the LIHAM@AuNPs@PDA@RB hydrogel remained in the elastic deformation region for a longer time. This result showed that the hydrogel was more elongated, more flexible, and more ductile against force. It has been understood that the LIHAM hydrogel has a more brittle behavior than the LIHAM@AuNPs@PDA@RB hydrogel, both because of the analysis and according to the observations during the experiment (Ersoy et al., 2024).

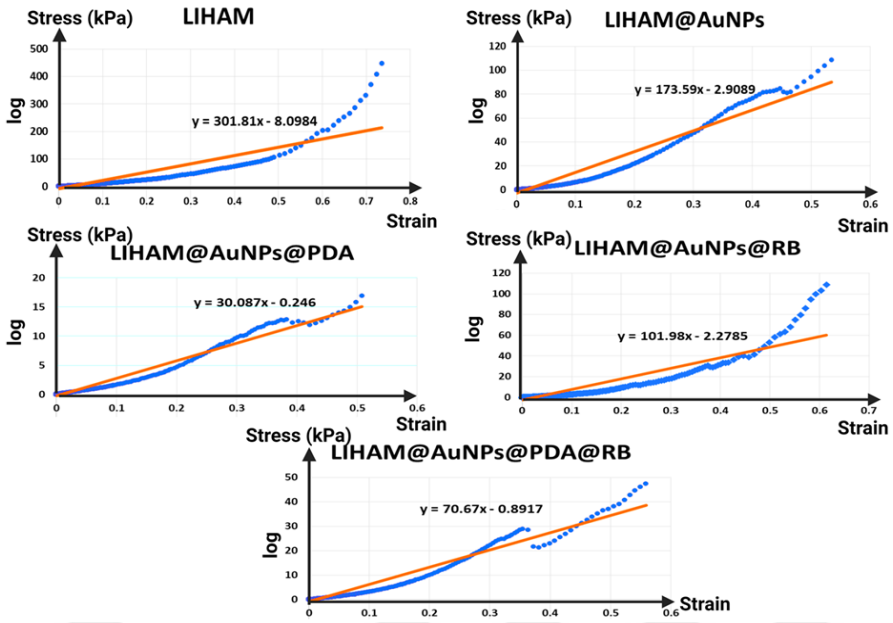


Figure 21: Young's modulus curves for five different hydrogels stress/strain curve diagrams with blue lines (datas from the analysis) and orange lines (linear fits) (Ersoy et al., 2024).

When *Figure 21* is examined, the slopes of the stress/strain diagrams are shown. The number written next to the x value in the equations of the slope lines shows the slope of the graph. Since Young's modulus value was found from the stress/strain ratio, the slope gave the elastic modulus value. According to the calculation results, elastic modulus value of hydrogels gave these values: LIHAM hydrogel is 301.81 kPa, LIHAM@AuNPs hydrogel is 173.59 kPa, LIHAM@AuNPs@PDA hydrogel is 30.087 kPa, LIHAM@AuNPs@RB hydrogel is 101.98 kPa, and LIHAM@AuNPs@PDA@RB is 70.67 kPa, respectively. The obtained elastic modulus values were interpreted according to the application area and it was aimed to select the most efficient hydrogel. The elastic modulus represents stiffness, that is, the resistance of the hydrogel to deformation. The high elastic modulus shows that the material is rigid, and the elastic strain will be small when tensile force is applied. For this reason, when the values are compared, the fact that the LIHAM hydrogel has the highest elastic modulus shows that the hydrogel has a more rigid feature than the others and is not prone to change shape. When force was applied, the LIHAM hydrogel disintegrated faster under force because the range of reversible extension behavior was smaller than other hydrogels. The lowest elastic modulus value was observed in LIHAM@AuNPs@PDA and

LIHAM@AuNPs@PDA@RB hydrogels. Due to the chemical and physical bonds between the hydrogels, the hydrogel is stronger and more flexible, and thus, it showed better elongation behavior under force than the LIHAM hydrogel due to its ductile structure. While RB and PDA additives increase printability, they also change the chemical bonds between NIPAM and PEG polymers, making the material more flexible and durable. When rheology analyses were generally interpreted, it was seen that LIHAM@AuNPs@PDA@RB hydrogel gave the best results in terms of durability, energy storage, high force resistance at high temperatures, flexibility, and tendency to deform. Additionally, it has been shown in previous studies that the modulus value of the hydrogel increases at higher temperatures (Zhang et al., 2023b). The reason for this is that gold nanoparticle, RB, and PDA conjugation were added to the NIPAM and PEG solution, changing the chemical bonds between them, and allowing the material to have a more planar flexible structure. Literature-based research indicates that metal ions create coordination complexes with amino groups to form non-covalent crosslinking, which results in the production of stiffer nanogels. Because of this, it was assumed that combining NIPAM, PEG, and AuNPs in the solution altered the bonds, which is why it was projected that the mechanical, chemical, and thermal characteristics of the newly created hydrogel solutions would alter (Ersoy et al., 2024). Furthermore, AuNPs coated with PDA exhibit darkening of the particles and an observation of excessive amine solubility, which is created by the oxidative self-polymerization of dopamine. It has been found that the boiling point of a substance rises with the number of amine groups present, along with the hydrogen bonding rate and the force needed to break the bonds (Huang et al., 2023). The RB molecule is a common photosensitizer for photodynamic therapy and an appropriate agent for nanoparticle bio-conjugation. It was believed that an increase in the mechanical and thermal characteristics coming from the aromatic groups was seen when the groups still present in the RB structure were introduced to the LIHAM solution. It has been predicted that the changes occurring in LIHAM and other hydrogels are due to the chemical bonds of the added photoinitiators (Wang et al., 2013).

Viscoelastic Behaviors

The viscous component of the stress is represented by the loss modulus (G" or E") of a material. Comparably, the storage modulus (G′), which drives the abrasive

particles radially (normal force), is a measure of the capacity to store energy elastically. Because the rate of shear is so low at low frequencies, there is a large capacity for the medium to retain its original strength. The rate of shear rises with frequency, increasing the amount of energy input to the polymer chains in the process. As a result, in *Figure 22*, storage modulus rises with frequency. If the storage modulus is higher than the loss modulus in the graph, this shows that the material is more solid than liquid. When this material was deformed, it was able to return to the yield point (Bilici et al., 2022, Ersoy et al., 2024).

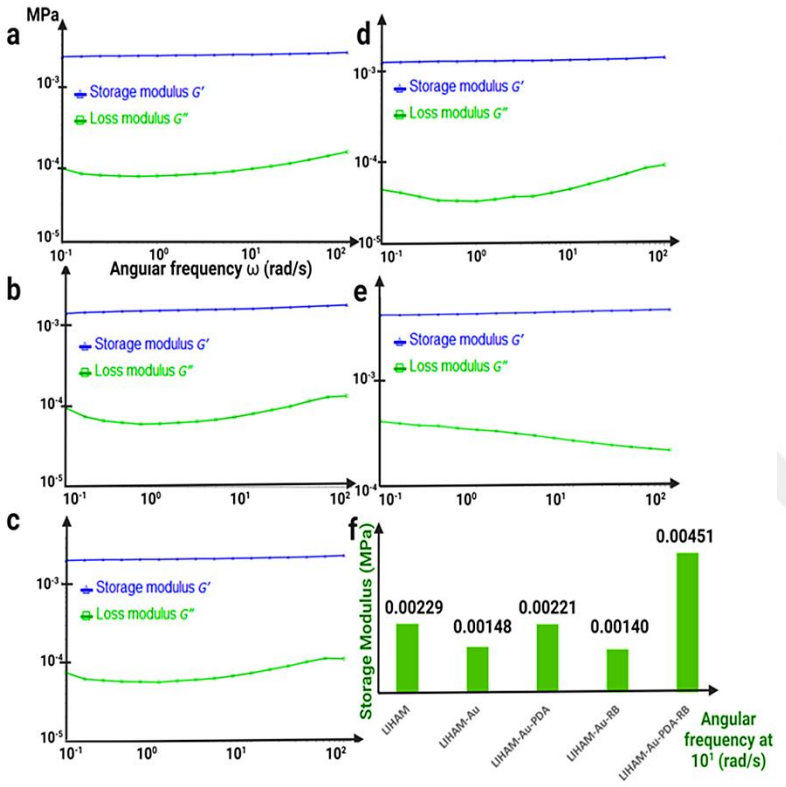


Figure 22: Angular frequency sweep of hydrogels **a** LIHAM, **b** LIHAM@AuNPs, **c** LIHAM@AuNPs@PDA, **d** LIHAM@AuNPs@RB, **e** LIHAM@AuNPs@PDA@RB, and **f** table of storage modulus (G′) of different hydrogels at 10^1 (rad/s) (Ersoy et al., 2024).

When more force was applied than the yield point, the material could not return to its previous shape. At 20° C, the strain ranged from 0.1 to 100, the shear rate from 0.01 to 100 (1/s), and the force amplitude/angular frequency from $\omega = 10^{-1}$ to 10^2 (rad s^{-1}) (Bilici et al., 2022). Rheological measurements were used to investigate the viscoelastic behaviors of the hydrogels (amplitude sweep test, frequency sweep test, and temperature sweep test) and compression analyses. Rheology analysis was carried out with oscillation movement and the samples were printed in a round

shape to ensure that the applied force spread equally throughout the sample. According to oscillation strain analysis, value ranges were determined for angular frequency analysis. In oscillation strain analysis, values of 10^{-1}-10^{2} were selected for hydrogels. When *Figure 22* was examined, the storage modulus was higher than the loss modulus, proving that the material showed solid behavior. At the point where the angular frequency value is 10, the storage modulus values of the hydrogels are shown in *Figure 22(f)*. According to the results, the hydrogel that can store the most energy was LIHAM@AuNPs@PDA@RB. The energy it stores has doubled compared to LIHAM hydrogel. This showed that the LIHAM hydrogel coated with AuNPs, RB, and PDA could store higher energy as viscoelastic behavior (Ersoy et al., 2024).

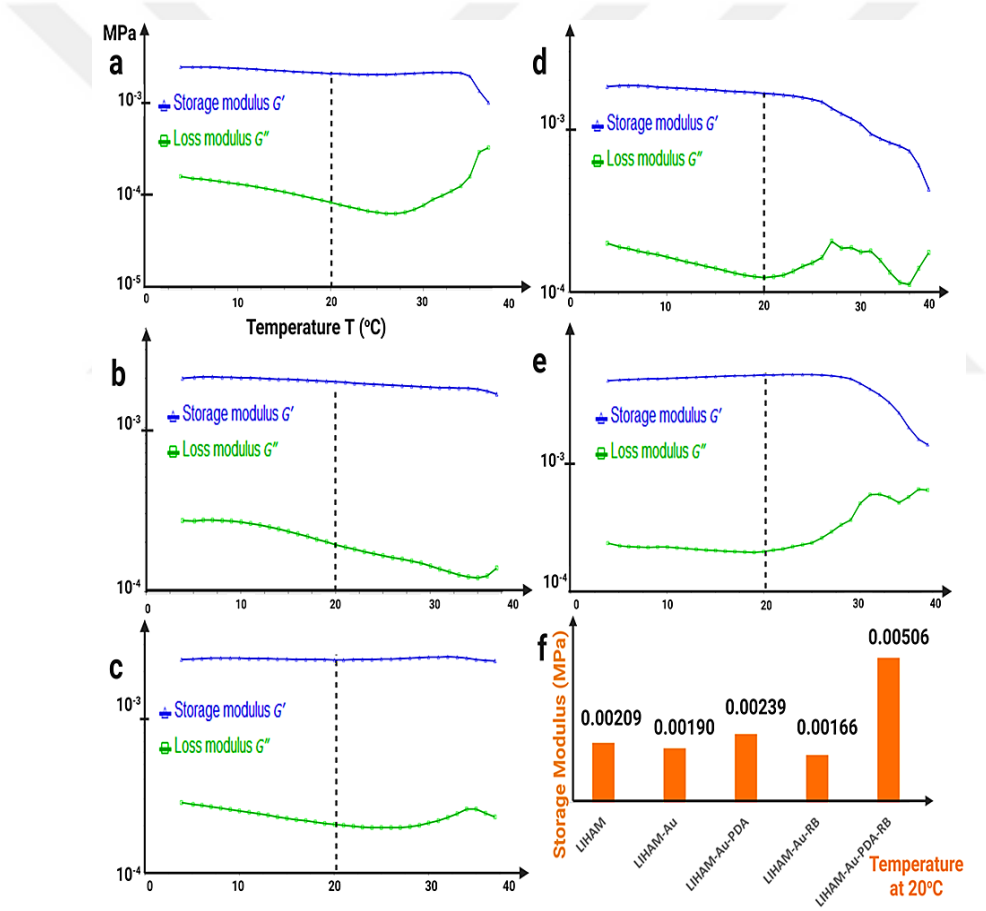


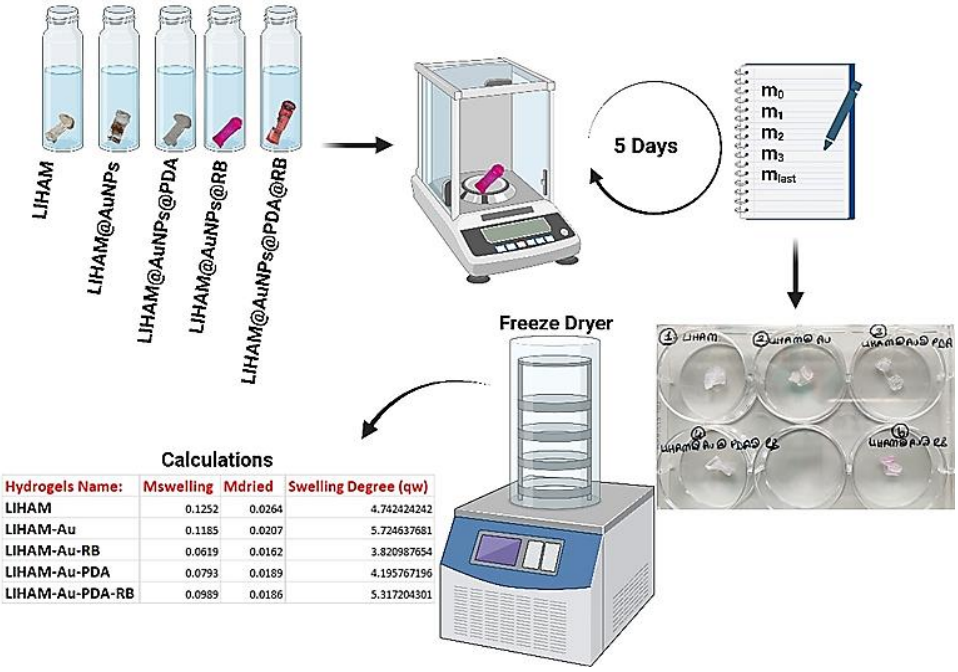
Figure 23: Temperature sweep analysis of hydrogels **a** LIHAM, **b** LIHAM@AuNPs, **c** LIHAM@AuNPs@PDA, **d** LIHAM@AuNPs@RB, **e** LIHAM@AuNPs@PDA@RB, and **f** table of storage modulus (G1) of different hydrogels at 20° C (Ersoy et al., 2024).

When *Figure 23(e)*, the graph of the LIHAM@AuNPs@PDA@RB hydrogel, is examined, it is seen that it has a much higher storage modulus value than the

LIHAM hydrogel. As of 27.5° C, the storage modulus value started to decrease. Although it had the same average storage modulus as the LIHAM hydrogel at 35° C, it showed a rapid decrease. At the same time, the loss modulus value started to increase starting from 20° C. The storage modulus of hydrogels when the temperature is 20° C is shown in *Figure 23(f)*. As in the angular frequency graph, it is shown that the LIHAM@AuNPs@PDA@RB hydrogel has twice the storage modulus than the LIHAM hydrogel at 20° C. In *Figure 23*, the changes in storage modulus and loss modulus values of LIHAM (a) and LIHAM@AuNPs (b) hydrogels depending on temperature are examined. As seen in FTIR analysis, adding AuNPs caused the proliferation of amino groups in the LIHAM hydrogel. The increase in amino groups caused the resistance to heat to increase and the melting-boiling point to increase. This shows that as the LIHAM hydrogel is heated to higher temperatures, when AuNPs are added, its storage modulus is still high and it does not transition to the liquid phase (Ersoy et al., 2024).

3.3.1.2.Osmotic swelling response

Hydrogel swelling properties are important variables that affect cellular function in biological investigations.



Hydrogels Name:	Mswelling	Mdried	Swelling Degree (qw)
LIHAM	0.1252	0.0264	4.742424242
LIHAM-Au	0.1185	0.0207	5.724637681
LIHAM-Au-RB	0.0619	0.0162	3.820987654
LIHAM-Au-PDA	0.0793	0.0189	4.195767196
LIHAM-Au-PDA-RB	0.0989	0.0186	5.317204301

Figure 24: Osmotic swelling response of five different LIHAM hydrogels after inside DW for five days and calculations of $M_{swelling}$, M_{dried}, and Q_w values (Ersoy et al., 2024) [BioRender].

The gel network's swelling characteristic offers cells a favorable environment, and its breakdown property promotes the development and proliferation of new tissue (Bilici et al., 2022). The hydrogels underwent swelling tests by being submerged in DW at RT. Analysis stages and calculation details are given in *Figure 24*. The weight swelling ratios of the hydrogels were then plotted against the names of five distinct hydrogels in *Figure 25*. When *Figure 25* is examined, the highest swelling ratio was observed in the LIHAM@AuNPs hydrogel. When the cytotoxicity analysis was examined, it was seen that the results were compatible with the swelling degree. Then, the highest swelling degree rate was observed in the LIHAM@AuNPs@PDA@RB hydrogel (Ersoy et al., 2024).

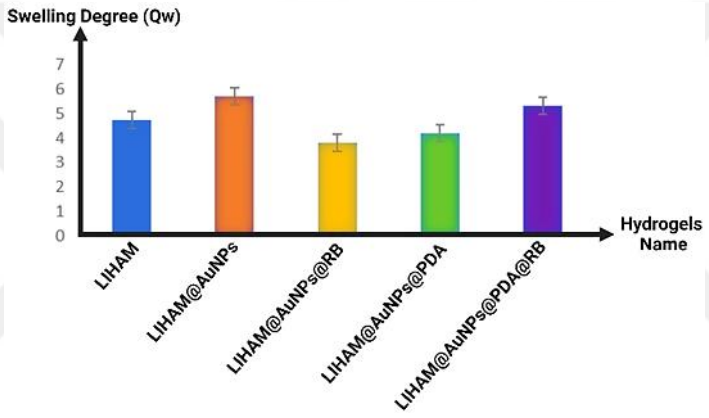


Figure 25: Graphic of swelling degree for each hydrogel according to the additives (Ersoy et al., 2024).

3.3.1.3.FTIR

The absorbance peaks of the chemical bonds in five distinct hydrogels are displayed in *Figure 26*. FTIR graphs of NIPAM, PEG, PEGDA, HEMA and AM chemicals from studies in the literature are shown in *Figure 27* (Ersoy et al., 2024). The peaks of pure NIPAM exhibit double bond properties in the 1600–1650 cm^{-1} (C=C aromatic and aliphatic) and 610–990 cm^{-1} (stretching mode of vinyl double bonds) ranges. Similar peaks (700-900 cm^{-1}) are seen for substituted groups with double bonds and cis-trans, as well as a characteristic peak for =C-H located somewhat above 3000 cm^{-1}. N-H stretching is also characterized by the large and powerful peak about 3292 cm^{-1} (Ersoy et al., 2024). The peak in the 2888 cm^{-1} band indicates the C-H bond for pure PEG (Ersoy et al., 2024). The carbonyl groups absorb at

1724 cm^{-1} and the C=C bonds at 1633 cm^{-1} on the PEGDA FTIR graph (Ersoy et al., 2024). The large -OH peak in the 3300–3700 cm^{-1} band of the HEMA monomer spectrum indicates hydrogen bonding.

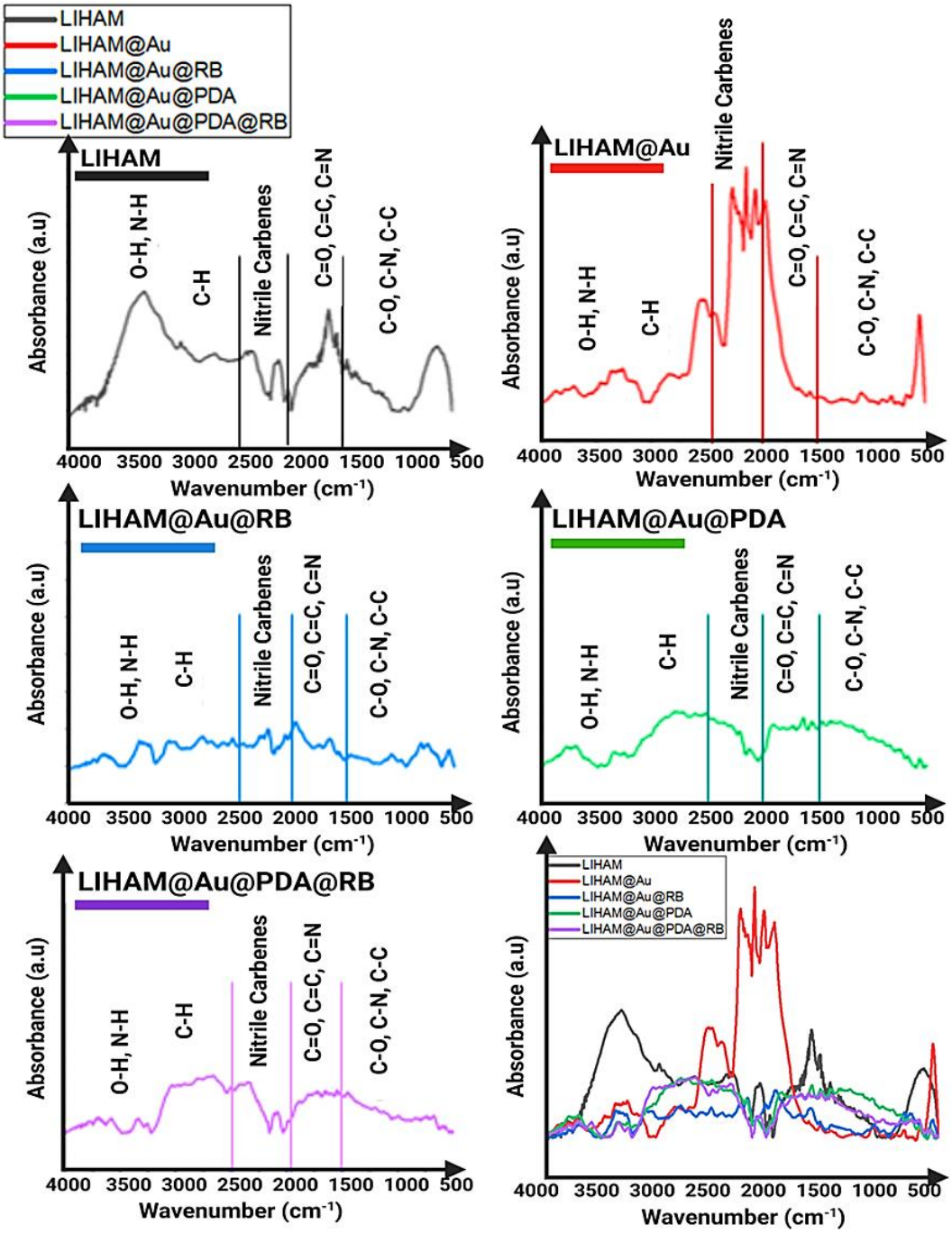


Figure 26: FTIR analysis of hydrogels between 500-4000 cm^{-1} (Ersoy et al., 2024).

In addition, the graph shows the shoulder at 3100 cm^{-1} and the peaks at 1637, 933, and 816 cm^{-1}, which correspond to the –C=C– in the HEMA spectrum. The FTIR graph of HEMA also shows the –C=O (1719 cm^{-1}), –C-O-C-(1321–1032 cm^{-1}),

and –CH2 (1404–1379 cm^{-1}) (Ersoy et al., 2024). When the graph of the LIHAM hydrogel was examined, it was seen that the C=O carbonly groups in the 1700 band range came from HEMA and PEGDA. It was estimated that the nitrile peaks in the 2000-2500 band range came from the AM monomer. It has been proven by FTIR analysis that adding gold nanoparticles significantly changes the chemical bonds of the LIHAM hydrogel, as observed in rheological analyses. Likewise, adding RB and PDA also changed the chemical bonds of the LIHAM hydrogel, according to FTIR results. Generally, O-H, C-H, and N-H chemical bonds were observed between 4000 and 3000 cm^{-1}. The source of nitrogen from the chemicals used in the LIHAM solution was seen in this range. With the addition of gold nanoparticles, the O-H bonds in the structure decreased in this range, but LIHAM revealed more nitrogen sources in its structure and showed C-Cl bonds in the 800-550 cm^{-1} band range. The use of gold (III) chloride raw material and four chlorine elements in RB showed the presence of C-Cl halogen bonds. It was observed that the absorbance of nitrogen bonds decreased in the peaks of LIHAM@AuNPs@RB hydrogel. In addition, by adding PDA to the LIHAM@AuNPs hydrogel, the peaks of Cl bonds decreased, and C-H bonds increased as seen in the 3000-2500 cm^{-1} band range. The peaks of C=O chemical bonds in the 1800-1500 cm^{-1} band range were observed both when RB and PDA were added. The halogen groups' peaks shrank when PDA was added. When the FTIR graph of the LIHAM@AuNPs@PDA@RB hydrogel was compared with the graph of the LIHAM@AuNPs@PDA hydrogel, different peaks were observed only in the nitriles carbenes band range (Ersoy et al., 2024).

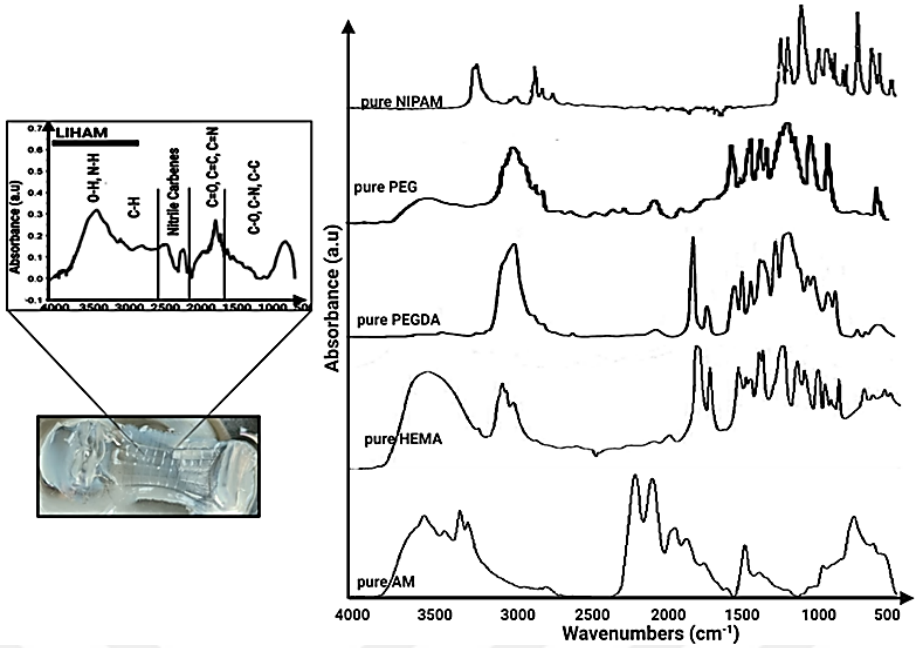


Figure 27: FTIR peaks for chemicals which used for producing LIHAM solution in the band range of 4000-500 cm^{-1} (Ersoy et al., 2024) [BioRender].

3.3.1.4.Enzymatic degradation

To assess the enzymatic degradability, swollen hydrogels containing different additives were incubated at 37° C for ten minutes at a collagenase concentration of 1 mg ml^{-1} (50 mg Collagenase/50 ml DPBS). Their weight loss was recorded at ten minutes intervals. In *Figure 28*, the enzymatic degradation analysis stages are shown in order (Bilici et al., 2022).

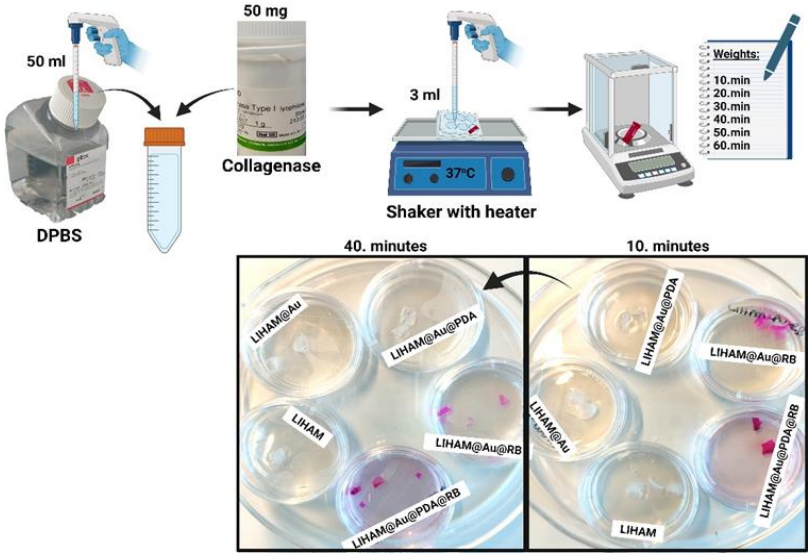


Figure 28: Enzymatic degradation analysis for each hydrogel [BioRender].

According to the graph shown in *Figure 27*, the LIHAM@AuNPs@PDA@RB hydrogel was completely degraded after 4 hours. Adding AuNPs, RB, and PDA to the LIHAM hydrogel, which had the lowest degradation, increased the degradation percentage. Since the decrease in mass was very small after the 80th minute, mass measurements were made at the 140th and 260th minutes. While LIHAM hydrogel cannot be degraded in the body for a longer period without adding additives, it has been proven that LIHAM@AuNPs@PDA@RB hydrogel, which can be completely degraded by the collagenase enzyme after 260 minutes, can be destroyed in the body after 260 minutes.

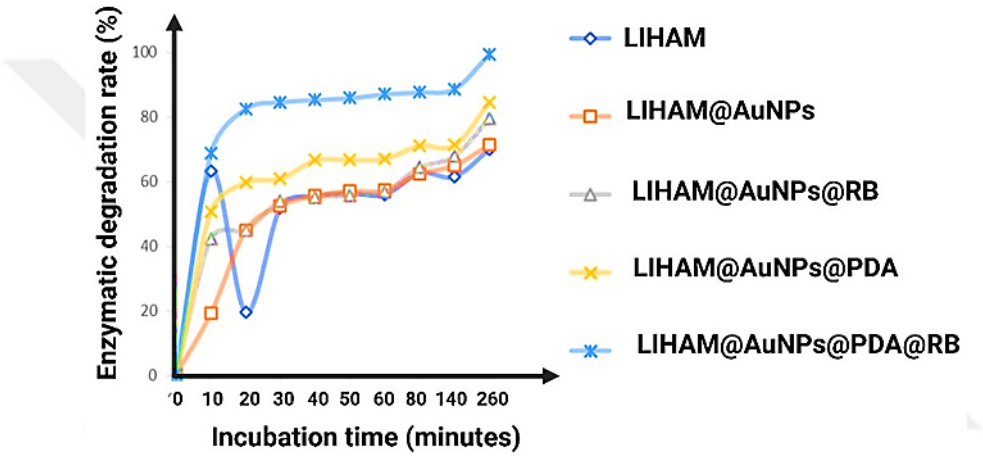


Figure 29: Enzymatic degradation rate percentage of hydrogels for 260 minutes [BioRender].

3.3.2. Structural/Morphological Characterizations

3.3.2.1.SEM and TEM

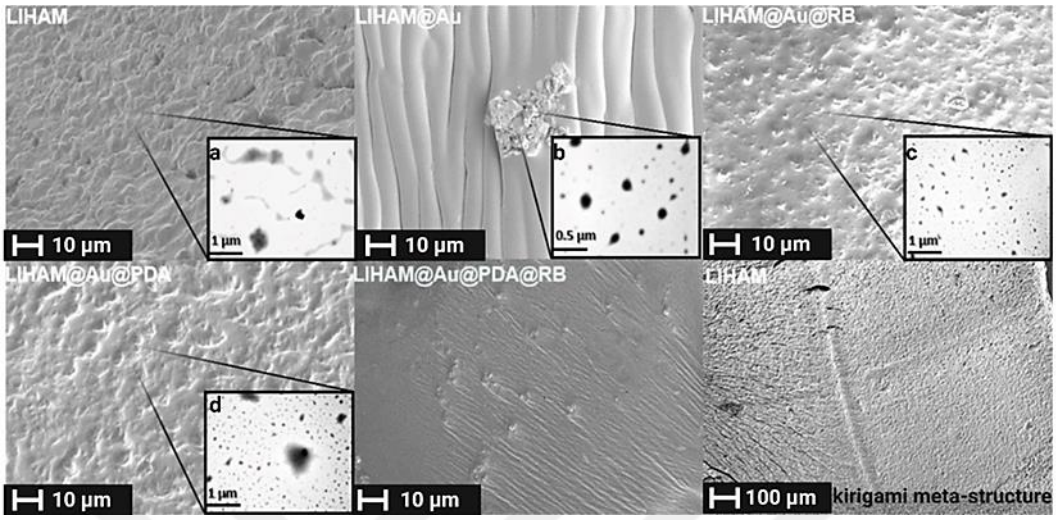


Figure 30: SEM of LIHAM hydrogel image at 10 µm and TEM of LIHAM hydrogel image at 1 µm, SEM of LIHAM@AuNPs hydrogel image at 10 µm and TEM of LIHAM@AuNPs hydrogel image at 0.5 µm, SEM of LIHAM@AuNPs@RB hydrogel image at 10 µm and TEM of LIHAM@AuNPs@RB hydrogel image at 1 µm, SEM of LIHAM@AuNPs@PDA hydrogel image at 10 µm and TEM of LIHAM@AuNPs@PDA hydrogel image at 1 µm, SEM of LIHAM@AuNPs@PDA@RB hydrogel image at 10 µm and SEM of kirigami shape of LIHAM hydrogel image at 100 µm (Ersoy et al., 2024) [BioRender].

When *Figure 30* is examined, SEM and TEM analysis images of the hydrogels are shown. When SEM analyses were examined, 10-micrometer images of the hydrogels were added. At the same time, the kirigami structure is shown with a 100-micrometer image of the LIHAM hydrogel. In *Figure 30(a)*, the image of the LIHAM solution in the TEM image is taken as a basis to interpret the TEM image of other hydrogel solutions. In the SEM image of the LIHAM@AuNPs hydrogel, particles were seen on the hydrogel. When the TEM analysis of the LIHAM@AuNPs solution was examined in *Figure 30(b)*, it was thought that the particles with a size of 200 nm were AuNPs. When the TEM image of *Figure 30(c)* was compared with the TEM image of *Figure 30(a)*, the presence of rose bengal and nanoparticles in the solution was observed at a scale of 1 µm. In *Figure 30(d)*, a TEM image of LIHAM@AuNPs@PDA solution at 1 µm is shown. The PDA structure appeared larger in solution in the TEM image compared to the nanoparticles. Since hydrogels are too large and dense substances for TEM analysis,

analyses were made from solutions of hydrogels. However, the solution of LIHAM@AuNPs@PDA@RB hydrogel was also too dense in concentration for TEM analysis. For this reason, TEM analysis of the LIHAM@AuNPs@PDA@RB solution could not be taken (Ersoy et al., 2024).

3.3.3. Thermal Characterizations

As a thermal characterization, DSC analysis was performed on the hydrogels to observe phase transitions, glass transition temperature (Tg) values, and reactions. At the same time, hyperthermia analysis was performed on five different hydrogels to examine the hyperthermia effect, which is one of the important aims of the study, and to prove that the developed hydrogels are photoresponsive-thermoresponsive.

3.3.3.1.DSC

DSC analysis shows how the heat capacity (Cp) of the material changes with temperature. The amorphous, crystalline, and glass transition temperature (Tg) values of the material were all understood thanks to this study. The Tg value was displayed in the shifted baseline section of the DSC analysis. The ascending peaks are the result of crystallization and represent exothermic reaction energy. The downward-pointing peaks represent the "melting" endothermic reaction energy. While amorphous polymers do not show melting temperature values, semicrystalline polymers show crystallization temperature and melting temperature values in DSC analyses. Confining the pNIPAM chains within nanopores may reduce their free motion and rotation, which could change the Tg. A positive delta T value indicates an exothermic reaction, while a negative value indicates an endothermic reaction. According to the literature, DSC analysis of pNIPAM undergoes an endothermic phase transition at a specific temperature. This phase transition includes a series of segmental motions and rotations in the surrounding free volume of pNIPAM (Ersoy et al., 2024).

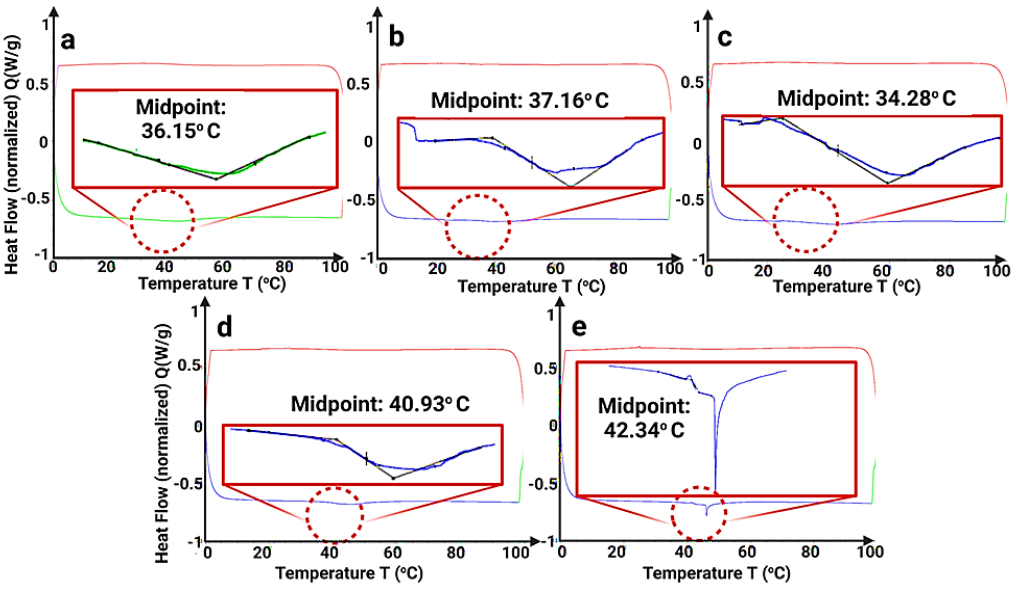


Figure 31: DSC analysis of five different hydrogels and Tg values of these hydrogels: **a** LIHAM, **b** LIHAM@AuNPs, **c** LIHAM@AuNPs@RB, **d** LIHAM@AuNPs@PDA, and **e** LIHAM@AuNPs@PDA@RB (Ersoy et al., 2024) [BioRender].

As seen in *Figure 31,* DSC analysis diagrams of five different hydrogels were compared. DSC analysis of LIHAM hydrogel showed a Tg value of 36.15° C. The Tg value of LIHAM@AuNPs hydrogel increased to 37.16° C. Adding gold nanoparticles increased the physical bonds between NIPAM and PEG hydrogel and increased the Tg value as it made the movements of the molecules more difficult. When the bonds between AuNPs and AuNPs@RB were examined, it was seen that the chemical bonds between pure nanoparticles were stronger. Therefore, adding RB decreased Tg only slightly. As seen in the FTIR analysis, it was observed that there was a significant difference between the LIHAM@AuNPs and LIHAM@AuNPs@RB peaks and when RB was added, it quenched many chemical bonds in the gold nanoparticles. For this reason, it was thought that there was a decrease in the Tg value. The Tg value of LIHAM@AuNPs@PDA hydrogel increased up to 40.93° C. The strong bonds between AuNPs@PDA, caused the bonds to strengthen in the LIHAM hydrogel. Therefore, it was understood that it should have more activation energy. It was observed that the highest energy was required in the LIHAM@AuNPs@PDA@RB hydrogel. By conjugating AuNPs@PDA@RB, the chemical bonds between them were strengthened and more energy was required for the molecules to move due to conjugation. The state in which π systems (such as double bonds) are "chemically linked together" is

referred to as "conjugation". Therefore, the Tg value increased to 42.34º C. At the same time, LIHAM did not show melting temperature and was found to be amorphous in structure. However, as the additives increased, a semicrystalline polymer structure appeared, especially in the DSC analysis of the LIHAM@AuNPs@PDA@RB hydrogel. The crystallization temperature showed an exothermic reaction between 43-45º C. It showed an endothermic reaction peak at a melting temperature 46.14º C and 0.23040 J/g enthalpy is necessary for melting. It was understood that the hydrogel changed from amorphous to semicrystalline as a result of the change in the chemical and physical bonds. At the same time, this interpretation is explained by the increase in mechanical properties and Tg value with semicrystallinity. The fact that the LIHAM hydrogel was completely transparent showed that the material was an amorphous polymer. However, since LIHAM@AuNPs@PDA@RB is a translucent polymer, it was proven to be semicrystalline with DSC analysis (Ersoy et al., 2024).

3.3.3.2.Hyperthermia analysis

In this study, five different printed hydrogels were also loaded with additives and were exposed to a 565 nm yellow laser without using a heater, and their shape changes were analyzed by heating them with gold nanoparticles, rose bengal, and PDA. Images of LIHAM, LIHAM@AuNPs, LIHAM@AuNPs@PDA, LIHAM@AuNPs@RB, and LIHAM@AuNPs@PDA@RB hydrogels have been added in *Figure 32*. The first images of the hydrogels after printing, the second images after exposure to 565 nm yellow laser for 20 minutes, and the final images after exposure to the heater for 20 minutes are shown, respectively (Zhang et al., 2024).

When *Figure 32(a)* is examined, there is no change in the structure of the LIHAM hydrogel as it does not show any heating under 565 nm light since it does not have any nanoparticles or additives in its structure. When heated to 60º C with a heater, color change, shrinkage and elongation were observed. For other hydrogels, observations were made under 565 nm light and with a 60º C heater, respectively. In particular, the color change of the hydrogel containing RB was observed more clearly and the hydrogel began to become transparent as it heated. It has been shown

in previous studies that as the temperature increases, an opaque material can become transparent due to the different orientation of the atoms in the hydrogel due to their transformation (Zhang et al., 2023b, Zhang et al., 2023a).

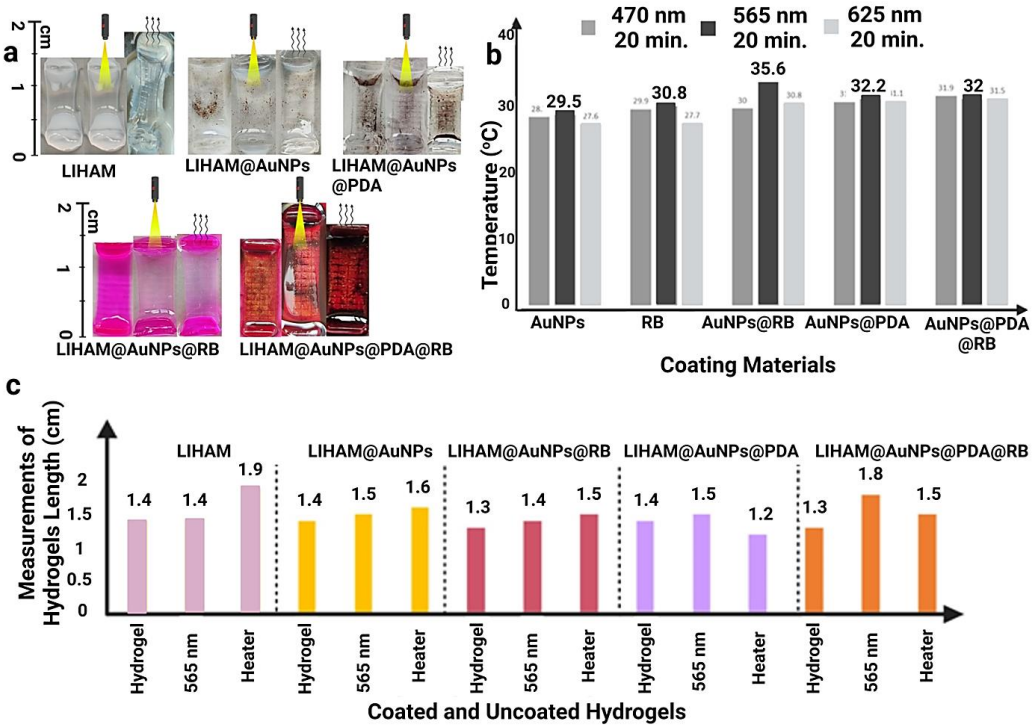


Figure 32: a Hyperthermia analysis of five different hydrogels at a 565 nm (yellow laser) light source which is the best light for AuNPs, RB, and PDA to increase the temperature and cm scale of length of hydrogels at the beginning, after 565 nm light for 20 minutes and after heater for 20 minutes respectively. **b** Temperature degrees of AuNPs, RB, and PDA photosensitizer after 20 minutes at three different visible light sources (470 nm (blue), 565 nm (yellowish green) and 625 nm (red)). **c** Length of five different hydrogels at the beginning, at 565 nm and heater respectively (Ersoy et al., 2024) [BioRender].

Since the hyperthermia analysis result of AuNPs@PDA@RB coated particles gives the best results under 565 nm green light, the analysis of the hydrogels was also performed under 565 nm by waiting for them to warm up for 20 minutes. It is shown in *Figure 32(b)*. According to the analysis results, LIHAM@AuNPs@PDA@RB showed the best hyperthermia effect. When explained in terms of mechanism, it is shown in *Figure 32(a)* that with the increase in temperature observed, the LIHAM hydrogel changes from a globally uniform transformation state to a locally diverse transformation state, and thus the hydrogel shrinks when heated (Zhang et al., 2023b). As seen in *Figure 32(b),* it is shown how much the additives heat up under lasers with three different wavelengths for 20 minutes. The 565 nm green light laser

absorbs more than other blue and red lasers and can convert light energy into heat energy. In the literature, the UV-visible analysis results of gold nanoflowers, RB, and PDA are consistent with the data in *Figure 32(b).* It has been understood that RB and AuNP particles especially absorb lighter and heat since they show absorbance in the 500-600 nm band in UV analysis (Ersoy et al., 2024). The heat absorption properties of hydrogels at three different nm laser sources in *Figure 32(b)* were interpreted by researching UV analyzes from the literature. The absorbance value of pure RB molecule is very high around 550 nm. Likewise, AuNps@RB also shows a peak around 550 nm in UV-analysis (Ersoy et al., 2024). Since adding RB increases the absorbance value, it is thought to be more successful than PDA in converting light energy into heat energy. It has been determined that particles at wavelengths of 625 and 470 nm have a lower potential to absorb light and convert it into heat energy.

Since *Figure 32(a)* and *(c)* were drawn in harmony with the measurements, they were seen to support each other and were examined together and commented on. In *Figure 32(c),* the lengths of the hydrogels during printing and after being kept in a heater and 565 nm yellow light for 20 minutes are given for five different hydrogels, respectively. The average length of all hydrogels after printing was measured as 1.3-1.4 cm. It was observed that the LIHAM hydrogel elongated the most after being kept in the heater for 20 minutes. After being exposed to 565 nm light for 20 minutes, there was almost no change in the length of the LIHAM hydrogel, and it did not change shape. It was observed that LIHAM was not a photo-responsive hydrogel before adding any additives. LIHAM hydrogel is a thermo-responsive polymer and changes shape with the heater. However, when gold nanoparticles, RB, and PDA were added, the hydrogels became photoresponsive. In particular, the LIHAM@AuNPs@PDA@RB hydrogel has been proven to be both photo-responsive and thermo-responsive. LIHAM@AuNPs@PDA@RB hydrogel was able to change its shape with a heater by exposing it to 565 nm light for only 20 minutes and its length was 1.8 cm. Thus, it converted heat energy by absorbing light energy and changed shape thanks to NIPAM.

3.3.4. In Vitro Characterization

As an in vitro analysis, Luciferase-based cytotoxicity analysis was performed on five different hydrogels.

3.3.4.1.Luciferase-based cytotoxicity assay

Hydrogels should not be significantly cytotoxic to be used in possible biological applications and to determine biocompatibility. Therefore, we used BJ cells—fibroblasts derived from skin to assess the cytotoxicity of five distinct hydrogels in a 10% DMSO solution. Luciferase-based cytotoxicity assay analysis was performed concerning the study in the literature (*Figure 33*). Cell viability percentage graph of LIHAM, LIHAM@PDA, LIHAM@AuNPs, LIHAM@AuNPs@PDA, LIHAM@AuNPs@RB, and LIHAM@AuNPs@PDA@RB hydrogels as a result of luciferase-based cytotoxicity assay (Ersoy et al., 2024).

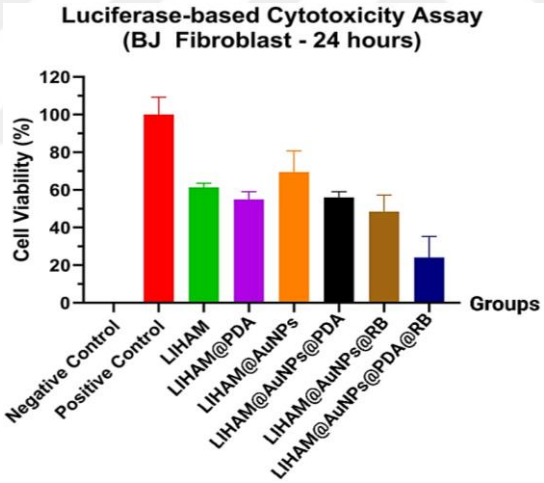


Figure 33: Cell viability percentage graph of hydrogels as a result of luciferase-based cytotoxicity assay (Ersoy et al., 2024).

When *Figure 33* is examined, it is observed that the best result is given by LIHAM coated with AuNPs. Only the cell viability of LIHAM hydrogel is lower without gold nanoparticles. It has been observed that gold nanoparticles increase cell viability. However, it has also been seen in studies in the literature that cell viability decreases as PDA concentration increases (Mahmoud et al., 2021). For this reason, it was thought that the PDA ratio used in this experiment was high. The cell viability of LIHAM hydrogel was 60.594%. LIHAM@PDA hydrogel was made to observe

the PDA effect. After LIHAM hydrogel was printed with a 3D printer, it was coated with PDA in the same proportions and stages as the gold nanoparticle procedure. The cell viability of LIHAM@PDA hydrogel was 58.528%. The cell viability of LIHAM@AuNPs hydrogel was 81.606%. It has been proven that gold nanoparticles highly reduce NIPAM toxicity and can be used in biomedical applications (Ersoy et al., 2024). However, a study in the literature has shown that RB is phototoxic in vitro (Yao et al., 2014). For this reason, it was thought that cell viability decreased due to its use at high rates. For this reason, LIHAM results coated with RB were more toxic than LIHAM only hydrogels.

Discussion

These results show that LIHAM hydrogels printed in kirigami form from NIPAM and PEG solution with PμSL printer can be printed by doping with AuNPs, PDA, and RB photosensitizer agents to be developed morphologically, thermally, and mechanically for the specific application areas. In our previous study, 100 nm size gold nanoparticles that gave the best morphological, thermal, biological, and optical results were selected from the metal oxide NPs synthesized with the help of BE via the green synthesis method and were used in this thesis. pNIPAM is one of the most popular stimulus-responsive polymers for research and when it was examined in previous studies in the literature on pNIPAM, research was shown in biomedical applications by generally using it with a second biodegradable polymer material, since it is a toxic material (Ersoy et al., 2024). Because it is a thermo-responsive material that is difficult to synthesize and especially to print with 3D printers, research has generally been done on production methods. Research on pNIPAM developed by doping with nanoparticles has also been investigated (Ersoy et al., 2024). When the literature was researched on PDA-doped nanoparticles and RB-doped nanoparticles, many studies were encountered (Ersoy et al., 2024). However, no hydrogel design has been seen in the literature by adding both PDA, RB, and gold nanoparticles to the solution prepared with NIPAM and PEG, as in this study to hyperthermia analyses via 565 nm light.

The new material called LIHAM in the previous study (Ersoy et al., 2024), which was prepared with NIPAM, PEG, and other monomers, is a very soft material after being printed in pure form and does not convert light energy into heat energy. When

AuNPs, PDA, and RB were added inside this solution, the printed LIHAM@Au@PDA@RB hydrogel turned into a material with a more solid form, regular kirigami shape, better mechanical and chemical properties, and high printability properties. The added photosensitizer materials were very beneficial according to the results. In this article, the benefits of AuNPs, PDA, and RB were compared with five different hydrogels developed separately.

Rheology analyses were one of the most successful analyses of LIHAM@AuNPs@PDA@RB hydrogel. It was twice as good as the LIHAM hydrogel in terms of viscoelasticity and energy storage. When the DSC analysis was examined, it was determined that the LIHAM hydrogel had an amorphous structure and the Tg value was 36.15º C, but the chemical bonds between the LIHAM@AuNPs@PDA@RB hydrogel were strengthened and showed Tm and Tg (42.3º C) values in the semicrystalline structure. According to the hyperthermia results, the LIHAM@AuNPs@PDA@RB hydrogel was able to change shape under 565 nm light as much as the LIHAM hydrogel changes shape when heated with a heater. At the same time, it was observed that the hydrogel began to shrink and elongate as it heated and became transparent. The five distinct hydrogels that were created have very different morphologies and physicochemical analyses. The material had a more planar, flexible structure, and the chemical linkages between NIPAM and PEG solution were altered by adding gold nanoparticles, RB, and PDA conjugation during photo-polymerization under UV light with a 3D printer photo-polymerization. Studies based on the literature have demonstrated that metal ions and amino groups form coordination complexes that result in non-covalent cross-linking and the creation of stronger nanogels. Thus, it has been proposed that the bonds are altered when NIPAM, PEG, and AuNPs are combined in solution (Ersoy et al., 2024). The graph of the LIHAM@AuNPs hydrogel in FTIR analysis shows the proliferation of amino groups. PDA-coated AuNPs have also shown extremely high amine solubility. It has been observed that the concentration of amine groups, hydrogen bonding rate, and bond-breaking force all raise a substance's boiling point. It was postulated that an enhancement in the mechanical and thermal properties of the aromatic groups was seen when the groups remaining in the RB structure were added to the LIHAM solution. The FTIR analysis revealed the presence of aromatic groups and an increase in C-H peaks when RB was added to

the LIHAM@AuNPs@PDA hydrogel. It was anticipated that the chemical bonds of the additional photoinitiators would cause the modifications seen in LIHAM and other hydrogels (Ersoy et al., 2024).

However, this study also has limitations observed during the analyses and aspects that need to be improved in future studies. Since all LIHAM hydrogels were too large and thick for TEM analysis, five different LIHAM solutions were used in TEM analysis by dropping 1 drop onto the grid instead of the hydrogel. Since LIHAM@Au@PDA@RB was a very thick and too dense solution, an image could not be obtained in TEM analysis. It was believed that lesser concentrations may be evaluated for TEM analysis since the printer was set to generate the best monomer concentrations.

Increasing temperature values were observed by keeping the photosensitizer additives solutions prepared with AuNPs, RB, and PDA under 470, 565, and 625 nm visible light for 20 minutes. Because of this analysis, 565 nm yellow light was selected as the most suitable visible light with a temperature increase of up to 35.6^{o} C. Hyperthermia analysis was performed on the hydrogels under this visible light. Nevertheless, for the hyperthermia analysis, after the hydrogels were printed, 100 microliters of additive solutions were added to them so that they could be transformed from light energy into heat energy and changed shape. For this reason, the AuNPs@PDA@RB ratio used in future studies can be increased and added after printing. It was thought that the hydrogels could not be mixed with enough gold nanoparticles because the gold nanoparticles settled to the bottom after the solution was prepared and added to the printer case during 3 hours. It has been observed that adding AuNPs, PDA, and RB photosensitizer agents directly into the solution is not efficient, and adding AuNPs, AuNPs@PDA, AuNPs@RB solutions after the LIHAM hydrogel is printed in the printer will be more efficient. As an alternative, it is thought that smaller-sized gold nanoparticles can be produced for future studies, or Triton-X can be dropped into the solution during ultrasonic mixing for the disperse process in LIHAM solution. Furthermore, it has been observed that hydrogels shrink a lot after a long time when heated with a heater. But still, the same amount of shrinkage was not observed under 565 nm light. It is thought that the reason for this is that the added nanoparticles were produced by the green synthesis method, not the traditional method, and due to their weak power to absorb

light energy and convert it into heat energy. Nonetheless, while green synthesis increased cell viability, it reduced the hyperthermia effect. When the studies in the literature were examined (Wang et al., 2014, Yao et al., 2014), it was seen that gold nanoparticles coated with RB could reach temperatures up to 70° C. When the experimental study in the literature was examined, it was seen that the gold nanoparticle synthesized by the traditional method also showed a stronger hyperthermia effect with the addition of silver.

As examined in the DSC analysis of the hydrogels, it was thought that the deformation temperature of the hydrogel may have changed since the Tg values changed with additives. It was observed that LIHAM@AuNPs@PDA@RB hydrogel did not shrink as much as other hydrogels, but only elongated Normally, if the cytotoxicity were compatible, the cell viability of the LIHAM@AuNPs@PDA@RB hydrogel was expected to be high. Nonetheless, as seen in some studies in the literature, it has been observed that excessive use of RB and PDA ratios increases toxicity. In addition, the hydrogels returned to their original shapes when placed in a +4° C refrigerator. It is shown in *Figure 34* that the hydrogels remained intact for three weeks.

Furthermore, the cell viability of LIHAM hydrogels with gold nanoflowers added was over 80%. It is thought that one of the reasons for this is the synthesis of gold nanoparticles using green synthesis. However, while green synthesis increased cell viability, it reduced the hyperthermia effect. Normally, if the swelling ratio (Q_w) value and cytotoxicity were compatible, the cell viability of the LIHAM@AuNPs@PDA@RB hydrogel was expected to be high. Nonetheless, as seen in some studies in the literature, it has been observed that excessive use of RB and PDA ratios increases toxicity (Yao et al., 2014).

It is thought that the developed LIHAM@Au@PDA@RB hydrogels will be beneficial not only in hyperthermia but also in the fields of photodynamic therapies, drug delivery, and tissue engineering, as a patch instead of tissue taken after surgery in cancer treatment (Sridhar et al., 2023). In future studies, the hyperthermia properties of LIHAM@Au@PDA@RB hydrogel can be further improved and loaded with drugs, thus contributing to research in the field of health. Finally, our approach has photothermal therapy or a skin patch on the cancerous area because

the developed hydrogel has become a promising material mechanically, thermally, and morphologically.

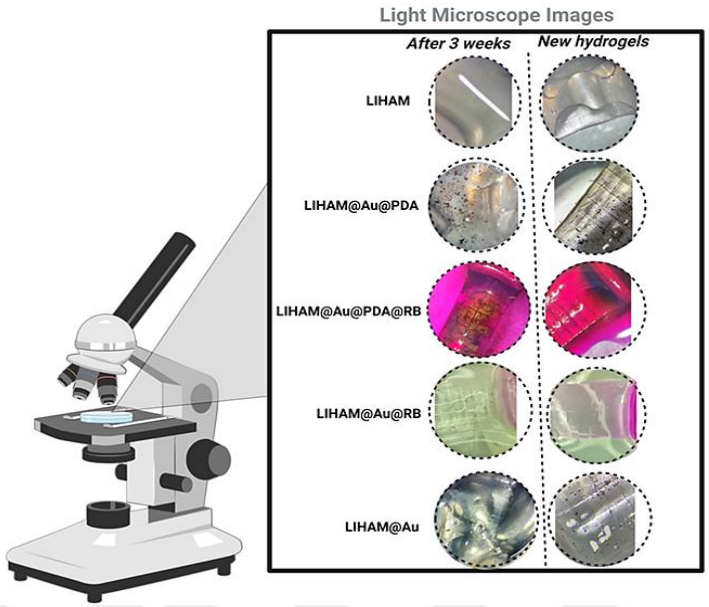


Figure 34: Microscopic images of the hydrogels after they were printed and kept in the refrigerator at +4° C for 3 weeks (Ersoy et al., 2024) [BioRender].

3.4.Conclusions and Future Works

In the second section of this thesis, the physicochemical, morphological, biological, and thermal properties of LIHAM hydrogels synthesized with AuNPs, PDA, and RB doped NIPAM-PEG generated with BE in the first part were compared. In addition, the positive impacts of additives on hydrogels were investigated. Furthermore, the optimal hydrogel for LIHAM was identified by evaluating hydrogel printability, exposure time, and light intensity. It was discovered that LIHAM hydrogel doped with AuNPs, PDA, and RB showed higher printability with high resolution. It was discovered that the hydrogels grew stronger as the exposure time and light intensity increased. However, continuous UV light exposure was demonstrated to disrupt the hydrogel's linkages, resulting in a brittle structure. Strong and flexible hydrogels can be printed using the right UV duration and light intensity. According to the results of physicochemical and hyperthermia analyses, the AuNPs@PDA@RB doped version of kirigami hydrogels printed with

a single mode of 20x2 mm, 8-6-6-6-4 base exposure time, and 60 lumens gave the best mechanical, thermal, and physical outcomes. According to the research completed for this study, LIHAM@Au@PDA@RB hydrogel is more printable than other hydrogels. When AuNPs, PDA, and RB photosensitizers were applied to hydrogels simultaneously, the resulting material was superior to when they were added separately. It was expected that keeping the gold nanoparticle ratio and density constant, coating with RB-PDA additives at a reduced rate and adding them to the LIHAM hydrogel would improve biological analyses. It was hypothesized that if smaller nanosized AuNPs could be created, they would be more dispersed in the LIHAM solution and hence more integrated into the hydrogel structures. In this method, the hyperthermia feature and biological effects of hydrogels are expected to improve. Because, as previously stated, AuNPs reduced the toxicity of LIHAM solution. Improved concentration studies of LIHAM@AuNPs@PDA@RB hydrogel have shown that it can be used in future studies, particularly in biomedical applications such as hyperthermia, photothermal therapy, drug delivery, and medical robotics, due to its good hyperthermia, shape change, and physicochemical properties. Future investigations will involve both in vitro and in vivo analyses (*Figure 35*). Thus, when AuNPs synthesized with the help of BE and smaller than 15 nm in size are conjugated with PDA and RB at non-toxic ratios, the hyperthermia effect can be studied on cancer cells, and the real performance can be observed.

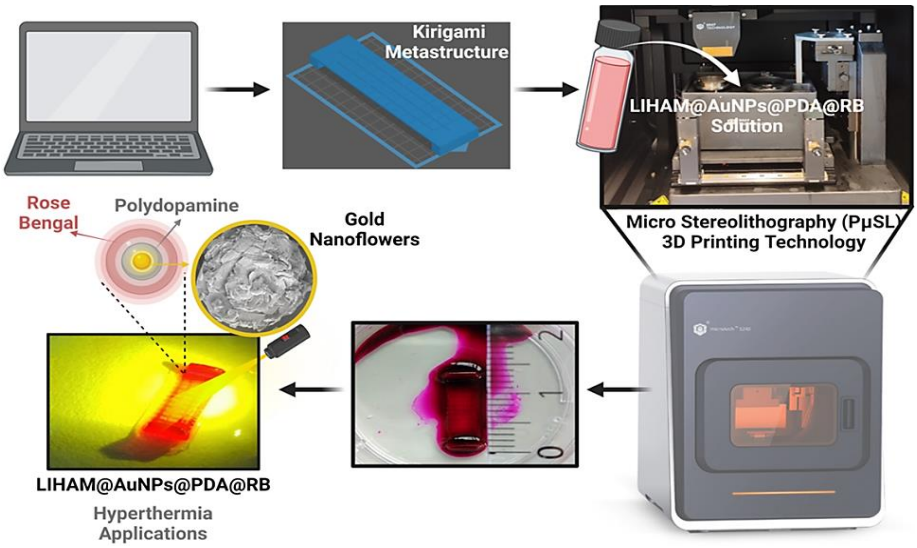


Figure 35: Briefly, the results of the second part and the inspiring LIHAM@AuNPs@PDA@RB hydrogel that can be used in future studies (Ersoy et al., 2024) [BioRender].

4. CHAPTER 4: 3D DIRECT-INK WRITING OF GREEN SYNTHESIZED NANOPARTICLES FOR MICRO-SUPERCAPACITORS

4.1.Introduction

As the world's population grew, the demand for energy has also increased. Non-renewable energy sources cannot match this increasing demand and could harm the environment; hence, there is an increased interest in renewable, sustainable, and clean energy systems (Putri et al., 2024). Electronics and energy storage research has been extremely successful, particularly in the fields of wearable gadgets, electric cars, smart electronic devices, human health monitoring, sensitive robotic skin, wearable photovoltaics, flexible transient electronics, fingertip gadgets and medical microdevices thanks to nanotechnology (Vandeginste, 2022). Furthermore, lightweight, flexible, and wearable energy devices have gained popularity in recent years. There are two important energy storage systems which are supercapacitors and batteries. They have different properties according to their electrochemical performances. Batteries store chemical energy using electrochemical reactions between positive and negative electrodes and an electrolyte (Maria Guerra, 2023, Ovhal et al., 2020) by Faraday's electrolysis principles which govern charging, which involves the movement of ions between electrodes to transform chemical energy into electrical energy and during discharge, the procedure is reversed. Supercapacitors, by contrast, store energy electrostatically. When a voltage is applied to both electrodes of a capacitor, a Helmholtz double layer forms, separating the ions in the electrolyte and producing a mirror charge distribution with opposing polarity (Maria Guerra, 2023). Another notable distinction is between energy density and power density for them. Energy density is the amount of energy stored

per volume, whereas power density is how quickly this energy may be supplied (Maria Guerra, 2023). Batteries have a higher energy density than supercapacitors, however, supercapacitors have higher power density therefore they transfer energy far faster than batteries. Cycle life refers to the number of charge and discharge cycles and supercapacitors have far longer cycle life than batteries (Maria Guerra, 2023). Batteries and supercapacitors are used to store energy, but their size and stiffness make them unsuitable for wearable devices. As a result, researchers have concentrated on creating flexible, thin-structured supercapacitors which are micro-supercapacitors (Vandeginste, 2022). In this section of the thesis, flexible, quasi-solid-state, symmetric micro-supercapacitors were created as wearable devices using ZnO nanoparticles and calcined broccoli, which were previously produced with BE from Chapter 2.

4.1.1. Micro-Supercapacitors

Micro-supercapacitors (MSCs) are systems that store charges at the electrode-electrolyte interface by reversible electrostatic ion adsorption or redox reactions (Tang et al., 2020). They have grown in favor in recent years because of their higher power density, quick rate capabilities, and long cycle life (Park et al., 2020). Despite its novel qualities, MSCs' limited capacitance has led to low energy density, limiting their practical application. As a result, high-performance MSCs have been researched to enhance capacitance (Park et al., 2020). This has been shown to be possible with the development of MSC design, the electrode and electrolyte materials used.

4.1.2. Mechanism of Micro-Supercapacitor

MSCs are classed based on electrolyte, energy storage mechanism and composition of the electrodes. MSCs are categorized into two groups based on their energy storage mechanism: electric double-layer capacitors (EDLC) and pseudocapacitors (PC) (Kamal K. Kar, 2023). EDLC is also created when charges separate at the electrolyte-electrode interface, resulting in charge storage. During charging, the two

electrode surfaces are either negatively or positively charged. As a result, the electrodes attract oppositely charged electrolytic ions. When the electric field scatters, the oppositely charged layers generate mutual attraction, which ensures the integrity of the electrical double layer and stores energy. During the discharge process, electrons flow from the negative to the positive electrode, releasing energy and creating a current in the external circuit. Porous carbon electrode material primarily constructs EDLCs, accounting for their large surface area (Kamal K. Kar, 2023). PC holds charge through rapid and reversible adsorption/desorption or redox reactions. During charging, the applied electric field causes ions to gather at the electrode-electrolyte interface, which is followed by a highly reversible process at the electrode that stores energy (Kamal K. Kar, 2023). During the reaction, ions discharge from the electrode, releasing stored energy via the external circuit. PC has a larger capacitance value than EDLC. Common PC materials include metal complexes, conducting polymers, MXenes, and metal-organic frameworks (Kamal K. Kar, 2023).

4.1.3. Types and Materials of Micro-Supecapacitors

Micro-supercapacitors are categorized into two types: stacking (or sandwich) and in-plane nesting configurations (Vandeginste, 2022). Sandwich supercapacitors include three components: electrodes, electrolytes, and separators. The perfect electrode should possess the following characteristics: Increasing the surface area can improve the specific capacitance, for better power density, the electrode must have high electronic conductivity, good thermal and chemical stability, and high corrosion resistance (Iqbal et al., 2020). Planar supercapacitors, also known as micro capacitors, are a new form of supercapacitor with three components integrated onto the same plane: electrode material, electrolyte, and current collector. The planar configuration design generates planar channels for electrolyte ions, allowing them to flow quicker in two dimensions (Iqbal et al., 2020). Furthermore, when supercapacitors are folded, rolled, or bent, the planar design has no impact on ion transport (Peng et al., 2014). Unlike the typical sandwich configuration, the two symmetric electrodes are positioned in the same plane. The most notable advantages

of this structural design are its smaller size and simpler manufacturing methods (*Figure 36*).

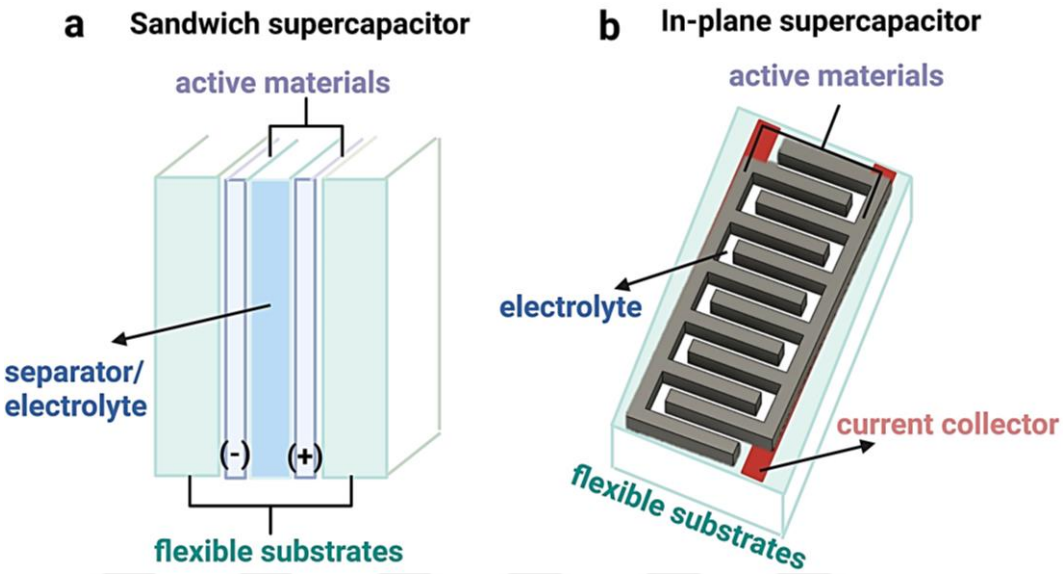


Figure 36: Supercapacitor types and required materials: **a** Sandwich type supercapacitor and, **b** in-plane supercapacitors (Vandeginste, 2022) [BioRender].

4.1.3.1.Electrodes

Electrode materials can be listed as carbon materials (EDLC), metal oxides (PC) and metal oxide-carbon composite materials. According to the classification of supercapacitors, there are advantages and disadvantages of these materials (Kamal K. Kar, 2023). EDLCs utilize activated carbon, carbon nanotubes, and graphene, whereas PC employ conducting polymers and metal oxides (Vandeginste, 2022). The first is carbon materials, such as one-dimensional (1D) carbon nanotubes and 2D graphene nanosheets (NSs), which are commonly employed in microelectronic double-layer capacitors (m-EDLCs) to obtain high-rate capacitance via ion sorption. In contrast, pseudocapacitive materials such as transition metal oxides are commonly employed to give higher capacitances (Jia et al., 2020). Detailed comparison of carbon, metal oxide and hybrid electrodes are given in Table *3* (Kamal K. Kar, 2023).

Table 3: Comparison of electrochemical advantages and disadvantages of carbon, metal oxide and composite electrodes (Kamal K. Kar, 2023).

Electrode Materials	Carbon	Metal Oxides	Metal Oxide-Carbon Composites
Surface area	High	Generally low	Generally controlled by carbon support
Pore size distribution	Various ways to tailor	Difficult to tailor	Carbon support tailoring options
Specific capacitance	Low	High	High
Conductivity	High	Low	Generally controlled by carbon support
Rate capability	High	Low	Good
Stability	Good	Poor	Good
Cost	Low	High	Moderate

Micro-pseudocapacitors (MPCs) have a lower rate capacitance than m-EDLC materials due to the presence of Faradic redox reactions (Kamal K. Kar, 2023). The inclusion of conductive carbon and pseudocapacitive materials into printable inks has been proposed as a viable method for improving electrical conductivity by constructing an optimum electrode structure with quick kinetic routes and large redox active sites (Tang et al., 2020). Carbon-based materials generate capacitance by accumulating electrostatic charge at the electrode/electrolyte interfaces (Kamal K. Kar, 2023). However, carbon-based electrodes powered by electric double-layer capacitance have a low theoretical capacitance. Carbon nanotubes (CNTs) are a popular carbonaceous material for energy storage system construction. CNTs boost the electrode's base frame conductivity. However, due to limited ionic penetration of the electrolyte, CNTs aggregate (Iqbal et al., 2020) reducing effective surface area and electrochemical efficiency. The use of transition metal oxides and/or sulfides can help to eliminate such discrepancies (Peng et al., 2014). To make high-

capacitance supercapacitors, PCs with capacitance obtained from the faradic redox reaction of pseudoactive materials such as transition metal dechalcogenide like MoS_2, TiS_2, CoS_2, ZrS_2 and transition metal oxide like RuO_2, MnO_2, NiO, TiO_2, ZnO, and conductive polymers like poly (2-methyl thioaniline) (PMTA), polyaniline (PANI), polypyrole (PPy), poly(3,4-ethylenedioxythiophene) (PEDOT), polythiophene (PTh), are employed (Kamal K. Kar, 2023). In terms of electrochemical performance, composite materials made from carbon and pseudomaterials outperform EDLCs and PCs (Kamal K. Kar, 2023). Nanostructured materials, such as 0 to 3D nanomaterials, have been proven to improve MSC performance due to their high specific surface area and porous structure for ion diffusion (Kurra et al., 2015). These 3D nanostructured materials created through chemical oxidation/reduction can be mixed with liquid binders to make slurries (Kurra et al., 2015). The spaces (pores) within the nanomaterial of this electrode allow the electrolyte to diffuse entirely. Furthermore, the high surface area nanostructure improves the energy density of MSCs (Kurra et al., 2015). However, the high electrical resistance at the nanomaterial interface, combined with the binders, decreases the conductivity of the electrode system, resulting in a lower power output (Kurra et al., 2015). Although a large specific surface area is the most basic criterion for supercapacitor electrode materials, it is insufficient to ensure optimal performance (Xue et al., 2011). Electrolytes can enhance electrode surface area but cannot produce ultra-micropores or narrow, lengthy micropore channels. As a result, constructing channels for 3D designs provides an opportunity to improve the performance of supercapacitors (Xue et al., 2011). In this thesis, a symmetric micro-supercapacitor was produced using the same material in both anode and cathode sections as electrode. ZnO NPs produced by green synthesis method using BE was used as an active material while calcined broccoli at high temperature was used as a carbon source to make metal oxide-carbon hybrid electrodes.

4.1.3.2.Electrolytes

An electrolyte is a solution of acid, base, or salt in a specific solvent. In general, electrolytes should have wide potential window and temperature range, great electrochemical stability, high ionic conductivity, environmental friendliness, and low cost (Iqbal et al., 2020). Electrolytes are categorized into three types: liquid,

solid-state (or quasi-solid-state), and redox active. Liquid electrolytes can be either aqueous (acid, basic, or neutral) or nonaqueous (Iqbal et al., 2020). Another classification is solid state electrolytes, which include dry solid polymers, gel polymers, and inorganic electrolytes (Iqbal et al., 2020). Solid electrolytes are often made up of an ionic conductor and a binder, such as a polymer, which allows for the production of solid layers. To date, PVA has been the most widely utilized binder material in solid electrolytes for 3D-printed supercapacitors (Kamal K. Kar, 2023). KOH is the most often used alkaline electrolyte, with better ionic conductivity than lithium hydroxide, sodium hydroxide, and other electrolytes (Iqbal et al., 2020). Quasi-solid state gel polymer electrolytes are flexible and elastic, making them excellent for wearable electronics. Gel polymer electrolytes are composed of a polymer, an electrolytic salt, and a solvent that are mixed using melt or solution processes such as in situ polymerization, casting, or phase inversion methods (Vandeginste, 2022). In this study, micro-supercapacitor generation was carried out employing gel polymer electrolytes containing KOH and PVA.

4.1.3.3.Current collectors

Supercapacitors have limitations due to their poor energy density. Because current collectors are one of the most important bulk components of supercapacitors, they can be used to overcome these restrictions. There are two kinds of current collectors: carbon- and metal-based. Metal-based materials include nickel foam, copper and aluminum foil, whereas carbon-based materials include graphene foil, carbon fiber, carbon paper, and graphite tape (Soni et al., 2024). The ideal current collector should have high electrical conductivity, low contact resistance with the active electrode material, a stable and strong bonding strength with the active electrode material, a large specific surface area, a high mechanical strength/modulus, a low weight, high thermal stability, high electrochemical stability, be environmentally and cost conscious (Soni et al., 2024). However, high conductivity inks were utilized directly as electrodes without the need for additional current collectors to demonstrate their efficacy (Abdisattar et al., 2022, Liu et al., 2021).

4.1.4. Additive Manufacturing for Micro-Supercapacitors

Efforts have been undertaken to boost energy storage by improving overall performance for energy conversion and storage, optimizing shapes to maximize the likelihood of reactions, and packing more active material into the same space (Putri et al., 2024). Various patterning techniques, including laser scribing, spray masking, and photolithography, have been employed in literature research to create patterned electrodes (Kurra et al., 2015, Park et al., 2020). However, large-scale MSC manufacture has severe restrictions, including complex processing. Over the last decade, researchers have studied MSCs manufactured using a variety of processes, including nickel foam, MEMS (deep reactive ion etching), interference beam graphene foam, and chemical vapor deposition. However, these MSC production processes are usually difficult, expensive, time-consuming, and they frequently require highly hazardous materials to remove the photoresist and template. AM was employed as a novel production method to generate 3D electrodes for MSCs. This technology has various benefits, including fast, low-cost, material-saving production and the capacity to change 3D objects (Kurra et al., 2015). 3D printing for energy storage uses computer-aided design to pattern electrode (or electrolyte) materials in three dimensions (Jia et al., 2020). 3D printing is a cutting-edge technique that allows for rapid processing and virtually limitless fabrication and modification of the desired material's morphological properties (Liu et al., 2015). Electrodes, electrolytes, and microfluidic components are frequently modified to improve mass transport via ion/compound diffusion channels, increase surface area to allow high loading of catalytically active materials and modify the material surface to facilitate better interfacial mechanisms by taking advantage of 3D printing technologies' freedom of geometry (Liu et al., 2015). Furthermore, the use of 3D printing in the manufacturing process has the potential to cut operational costs by correctly forecasting the required raw material using computational modeling, hence avoiding waste formation (Liu et al., 2015). 3D printing method employs layer-by-layer material deposition to raise electrode height, increasing the amount of active material loaded per unit area. In many circumstances, the interfacial resistance between layers is low because the printed layer fuses with the following layer as it transitions from liquid to solid, resulting in a monolithic structure (Kurra et al., 2015). Moreover, because printing does not result in material loss, material

can be retained during production. 3D printing also saves time and money by requiring only basic printing methods that take place under ambient circumstances. (Kurra et al., 2015) Direct ink writing (DIW), aerosol jet printing, fused deposition modeling (FDM), electrospinning-based printing, bonding inkjet (BIJ) printing, selective laser melting (SLM), digital light process (DLP) printing, two-photon lithography, and Meniscus printing have all been used to create 3D architectural electrodes for MSCs (Kurra et al., 2015).

4.1.4.1. Extrusion based 3D printing

Extrusion printing (EP), also known as direct ink writing (DIW), is a potential AM technique with features including material diversity, low cost, and a straightforward printing approach that does not require post-processing (Kurra et al., 2015, Park et al., 2020). Extrusion-based 3D printing, a novel technology, has recently been shown to generate complex structures with applications in a variety of fields, including electronics, biomedicine, and energy storage. Printing ideal structures without collapse is crucial for creating inks with high viscosities and shear-thinning rheological characteristics (Shen et al., 2018). During the printing process, functional inks are extruded from the nozzle and printed vertically on surfaces (Shen et al., 2018). EP broadens the material options for MSC electrodes by including large surface area materials like CNT, graphene, and pseudomaterial. However, rheology study is a precondition for selecting EP materials (Shen et al., 2018). The viscosity of the EP material reduces with increasing shear rate, indicating shear thinning. Extrusion briefly reduces the viscosity of the print medium, but it recovers to its former state once it exits the nozzle (Shen et al., 2018). This is significant because increased viscosity can help a printed structure retain its shape (Shen et al., 2018). As shear stress increases, the shear elastic modulus and loss modulus become more important. At low shear stress, the shear elastic modulus (G′) exceeds the viscous modulus (G″), which explains how materials retain their shape despite minor wetting/spreading effects (Shen et al., 2018). At higher shear stress, the shear elastic modulus (G′) is somewhat smaller than the loss modulus (G″), implying that when stress is applied to the material at the extrusion nozzle during 3D printing, the material flows and spreads freely, exceeding shear efficiency (Shen et al., 2018). When the material is exposed to ambient air via the nozzle, it hardens quickly before returning to a dormant condition under modest

shear stress (Shen et al., 2018). Although extrusion printing is commonly used to create 3D electrodes, it has several limitations. First, solids in solvents can clog nozzles, disrupting or impeding material flow (Shen et al., 2018). Second, it is challenging to print spatial 3D patterns such as helical shapes for complicated structures because ink is not a solid structure that can be damaged just by gravity. Therefore, printed items must be post-treated promptly (Park et al., 2020). To date, 3D printing has been utilized to create electrochemical structures for lithium-sulphur batteries, lithium-ion micro batteries, and symmetric MSCs. However, 3D printing of desirable devices with high electrochemical performance for energy storage applications is still in its early phase (Shen et al., 2018).

4.1.4.2.3D Printing parameters

When printing on an extrusion-based 3D printer, rheological and printing parameters also play an important role. While rheological parameters include thixotropy, shear thinning, viscoelastic behavior, and yield stress, printing parameters include nozzle diameter, printing speed, printing pressure, and nozzle temperature (Putri et al., 2024). The key rheological characteristics for a material to be utilized as an ink are that it is viscous, homogeneous, and can deposit smoothly without clogging the nozzle (Putri et al., 2024). Its viscosity should be low due to the high shear rate induced by the printer's pressure, which permits ink to flow through the nozzle (Putri et al., 2024). After the ink has deposited, it should instantly regain its solid-like qualities in order to maintain its shape (Putri et al., 2024). Chain entanglement caused by intermolecular hydrogen bonding, ionic interactions, and van der Waals forces causes the viscoelastic response of polymer liquids to applied force (Putri et al., 2024). The intermolecular chain entanglement of biobased polymers provides internal frictional forces that limit polymeric chain movement when exposed to external forces (Putri et al., 2024). Shear force determines polymer fluid flow and viscoelastic behavior (Putri et al., 2024). At low shear rates, chain entanglement in bio-based polymers inhibits movement, resulting in high viscosity and elastic solid-like behavior ($G' > G''$) (Putri et al., 2024). Increased shear rates cause unwinding and reorientation of the bio-based polymer chain towards applied forces, exceeding the yield stress threshold (τy) where $G' = G''$ (Putri et al., 2024). Unwinding the polymer chain reduced viscosity, resulting in viscous flow ($G' < G''$) (Putri et al., 2024). This mechanism allows a polymeric material to exhibit shear

thinning properties, which explains how the ink extrudes and flows from the printing nozzle during the 3D printing process (Putri et al., 2024). The loss tangent (tan δ) is a ratio of two values (G″/G′) that determines a polymeric ink's suitability for extrusion-based printing (Putri et al., 2024). Ink materials with tan $\delta > 1$ have fluid properties and are easily extruded during printing. Polymeric materials with tan $\delta < 1$ often have solid-like elastic properties (Putri et al., 2024). It is widely recognized that in extrusion-based printing processes, the extrusion rate and printing pressure must be adjusted simultaneously. The combination of high printing pressure and speed results in extruded ink in the form of droplets rather than filament (Putri et al., 2024). Low printing pressure and speed yield thick filament (Putri et al., 2024). As a result, the balance between these two properties needs to be improved.

4.1.4.3.Post-treatments

Pure bio-based polymers require a specific post-printing treatment before application. The most important post-printing step for bio-based polymers is solidification (Putri et al., 2024). Several procedures can be used to solidify the material, including drying, crosslinking, solvent exchange-phase inversion, heat treatment, and chemical treatment (Putri et al., 2024). The drying category comprises techniques like ambient drying, oven drying, and freeze-drying (Putri et al., 2024). It could range from conventional ambient temperature drying to cross-linking methods (Putri et al., 2024). Cross-linking is the most common post-printing solidification process for bio-based polymers that do not fully dry at ambient temperature (Putri et al., 2024). It was explained that the porosity formed by the freeze-drying process increases the available surface area for electrolyte transport, which speeds up ion diffusion (Putri et al., 2024). A fabrication approach that combines chemical crosslinking, freeze-thawing, solvent exchange, and ambient drying has been proposed to build a mechanically stable and porous structure for supercapacitors. Additional processing of 3D-printed bio-based polymers after solidification may be necessary to make them appropriate for energy conversion and storage applications. After the solidification of 3D printed bio-based polymers, thermal processing is the most commonly used fabrication method (Putri et al., 2024). Thermal processing can remove or convert bio-based polymers to carbonaceous compounds, thereby lowering unwanted electrical resistance (Putri et

al., 2024). Aside from that, thermal processing has been demonstrated to preserve the fine-printed structure. Thermally processed 3D printed electrodes have been demonstrated to carry electrons quicker than unprocessed or chemically processed ones (Putri et al., 2024). In this study, post-treatment was performed by applying oven drying after printing with an extrusion-based 3D printer.

4.1.5. Micro-Supercapacitor Ink Ingredients

In the near future, 3D printing could provide a sustainable, large-scale production approach for energy conversion and storage components (Putri et al., 2024). In addition to sustainable manufacturing through 3D printing, it is necessary to address the sustainability and ecology of materials used in energy conversion and device construction. It is well acknowledged that the key components of today's energy conversion and storage systems have a negative impact on the natural ecosystem and offer possible risks. This hazard is caused by the use of nonrenewable and harmful goods, which contribute to the depletion of natural resources and the contamination of terrestrial and aquatic ecosystems throughout their life cycles. As a result, it is vital to create a paradigm shift by combining biobased materials into energy device components. The natural availability, low toxicity, and degradability of biobased materials will increase sustainability and lessen the environmental effect of energy devices (Putri et al., 2024). The polyvinylidene fluoride (PVDF) binder and N-Methyl pyrrolidone (NMP) solvent are commonly utilized. However, because NMP is very toxic, it does significant harm to both human health and the environment. As a result, CMC was used as a binder and clean water as the solvent in this study. The study's goal was to demonstrate the energy potential of non-toxic materials, as green energy generation is the ultimate goal.

4.1.5.1.Green synthesized ZnO nanoparticles as an active material

Among all metals, gold has the highest conductivity, but it is also the most expensive and has a small reserve. Although copper and aluminum are both cheap and have strong electrical conductivity, their powders are rapidly oxidized and lose some of their electrical conductivity when stored (Li et al., 2020). Therefore, the use of metallic zinc anodes in micro-supercapacitors has become widespread due

to their advantages such as low redox potential, abundant resources, and excellent chemical stability in aqueous solutions (Zhu et al., 2024). ZnO is non-toxic and in the form of nanoparticles, the particles have a high surface-to-volume ratio (Domínguez-Perles et al., 2010). ZnO-NPs have attracted a lot of attention because to their exceptional properties, such as a broad direct band gap of 3.37 eV at ambient temperature and a high excitation binding energy of 60 meV (Domínguez-Perles et al., 2010). It has excellent surface conductivity and electron mobility. It's a low-cost, readily available, and environmentally beneficial substance (Kamal K. Kar, 2023). Zinc oxide is a common energy storage technology with a high energy density of 650 A/g. Despite some limitations, such as dendritic growth during repeated cycles, which reduces life cycle, it is a promising electrode material for supercapacitors (Dhanemozhi et al., 2017). NPs have also been used in many devices such as supercapacitors, solar cells, acoustic waves, and optically transparent electrodes (Jeon et al., 2023). There are chemical, physical, and biological methods to synthesize ZnO NPs. However, with the widespread use of green materials in energy storage, nanoparticles produced by the biological method, green synthesis, have also become quite attractive due to their certain properties such as cost-effectiveness, non-toxicity, and environmental friendliness (Jeon et al., 2023).

4.1.5.2.Broccoli extract and dried broccoli as a carbon content

Carbon-based electrode materials are useful for energy storage devices because they are inexpensive, have high conductivity, and are resistant to heat and chemicals (Iqbal et al., 2020). As mentioned in the introduction, it has been observed that combining carbon materials used in EDLC systems with metal oxide sources that exhibit pseudocapacitive effects results in better electrochemical analyses. In the literature, there is no record of an electrode system that utilizes metal nanoparticles produced from BE and a carbon source derived from burning broccoli at high temperatures.

4.1.5.3.Carboxylmethyl cellulose (CMC) as a natural binder

Bio-based polymers, which are polymeric macromolecules derived from biological or renewable resources, are a popular material choice due to their vast natural

reserves, versatility, biocompatibility, cheap cost, sustainability, and environmental friendliness. The macromolecular network and chemical properties have also been proven to boost ionic mobility, making them perfect for high-performance bio-inspired components including batteries, supercapacitors, and fuel cells. Furthermore, intrinsic physical properties such as viscoelasticity and shear thinning allow bio-based polymers to be produced utilizing 3D printing techniques (Putri et al., 2024). Furthermore, some low-cost, naturally abundant cellulosic bio-based polymers like CMC show promise as rheological aids. In this thesis study, CMC was used as a rheological aid for ZnO NPs and calcinated broccoli-based ink to form a cross-linked network structure that improves the rheological properties of the ink, providing a solid foundation for the design of the 3D printing process and performance enhancement of printed electrodes (Zhang et al., 2023c).

4.1.5.4.PDMS for encapsulation

Encapsulating the electrode and electrolyte is critical for sensor applications because it provides maximal protection from external influences and damage. Another rationale for encapsulating is to improve measurement sensitivity. Polydimethylsiloxane (PDMS) encapsulation appears to be an appealing alternative because to the elastomer's acceptable temperature and flexibility. It is also biocompatible, meaning it is safe for both humans and the environment. The encapsulation system is applied to the PDMS, which is cured at a temperature (Liu et al., 2021). Under a study, PDMS resin and curing agent (10:1 weight ratio) were mixed for 5 minutes, degassed under vacuum for ~30 minutes, carefully applied to the device surface, and cured at room temperature for ~24 hours (Pu et al., 2018).

In light of all of the above knowledge, the third section of this thesis aim to produce flexible, lightweight, wearable, quasi-solid-state, symmetric micro-supercapacitor devices using an extrusion-based 3D printer. Using the green synthesis process and BE, ZnO NPs were synthesized, the carbon source was generated by calcining broccoli at high temperatures, and natural polymer ink was created and printed in the desired MSC shape. This thesis is expected to contribute to renewable energy production by using ecologically friendly, sustainable, and non-toxic materials instead of traditional hazardous ones. Due to the environmental damage caused by

batteries and supercapacitors, it is hoped that high-efficiency methods, such as 3D printers, will enable the widespread adoption of biodegradable materials.

4.2.Materials and Method

4.2.1. Materials

Zinc oxide nanoparticles were made using DW, BE, and zinc acetate dihydrate $(CH_3COO)_2$ $Zn.2H_2O$, CAS No. 5970-45-6, 250 G) from EMSURE®. To produce the plant extract with ZnO and electrode slurry, broccoli that was acquired from Istanbul greengrocers was employed. To prepare the slurry from Nanografi, three ingredients were used: N-methyl-2-pyrrolidone (NMP), conductive carbon black (C-nergy Super C65), and polyvinylidene fluoride (PVDF) binder for three electrode electrochemical analyses. The electrochemical characteristics of both ZnO nanoparticles and calcined broccoli powders were investigated using potassium hydroxide (KOH) pellets obtained from AFG Bioscience as the electrolyte. In MSC device production, CMC was used as binder and DW as solvent to prepare the ink. Poly (vinyl alcohol) (95.5-96.5% hydrolyzed, MW. approx. 85,000-124,000) from ACROS Organics and KOH were used as the electrolyte in MSC. Aluminum foil was chosen as the current collector and fabrics as the substrate. The PDMS used for encapsulation was purchased from DOW as Sylgard 184 Silicone Elastomer Kit.

4.2.2. Producing extracts from broccoli

Unlike the broccoli production technique shown in *Figure 4*, extract production was carried out at lower temperatures and without the use of a centrifuge machine.

Broccoli bought from the grocery store was washed thoroughly. Then, the broccoli was dried using an airfryer at 250° C for 6 hours. After that 5 g of dried broccoli was extracted in 50 ml DW at 60º C for 1 hour (Ersoy et al., 2024). After filtration process with Whatman filter paper (110 mm ⌀) the cooled BE was kept in the refrigerator at +4º C. Unlike the first section, in this section, the BE was filtered using only Whatmann filter paper without a centrifuge step. In addition, it was aimed to obtain optimum contribution from broccoli by obtaining extract at lower temperatures. The pH value of the BE was 5.21. In addition, the ORP value (direct measurement of electrons in transition during oxidation-reduction reactions) of BE was measured as 327 and 106 mV with AQUA SEARCHER/PH METER.

4.2.3. Synthesis of ZnO NPs with the help of Broccoli Extract

The synthesis of ZnO NPs was carried out differently than the first part in *Figure 5*. Since it will be used as an electrode, the sintering time was determined as 1 hour since it was thought that porosity would be beneficial. Zinc oxide nanoparticles were synthesized using the green synthesis method and BE. 10 ml of prepared BE were added dropwise to 90 ml of DW. The solution was then mixed with the magnetic stirrer at room temperature. 0.1 M zinc acetate dihydrate was then added to the beaker. The solution was agitated at 70º C for 3 hours. To remove the solvents, it was dried at 100° C for 24 hours in the oven. When it had dried, it was ground with a mortar into a fine powder. The last heat treatment, calcination, was performed at 500° C for 1 hour. After the calcination procedure, the powdered ZnO NPs were once again pulverized in a mortar before being placed within tubes.

4.2.4. Calcination of Dried Broccoli

Broccoli powders dried in the airfryer at 250º C for 6 hours were placed in the calcined oven in the crucible at 300, 350, 375, 400, 450 and 500º C, respectively. Broccoli powders sintered at different calcination temperatures were ground into fine powder with the help of a mortar. Analyses were performed to examine the

effect of temperature on broccoli powder, and broccoli powder calcined at the optimum temperature was selected for use in electrochemical analysis. According to the obtained characterization results, it was seen that the best performance was given to broccoli calcined at 400° C for 1 hour (B400). Detailed comments and results are shown in the results section (*Figure 37*).

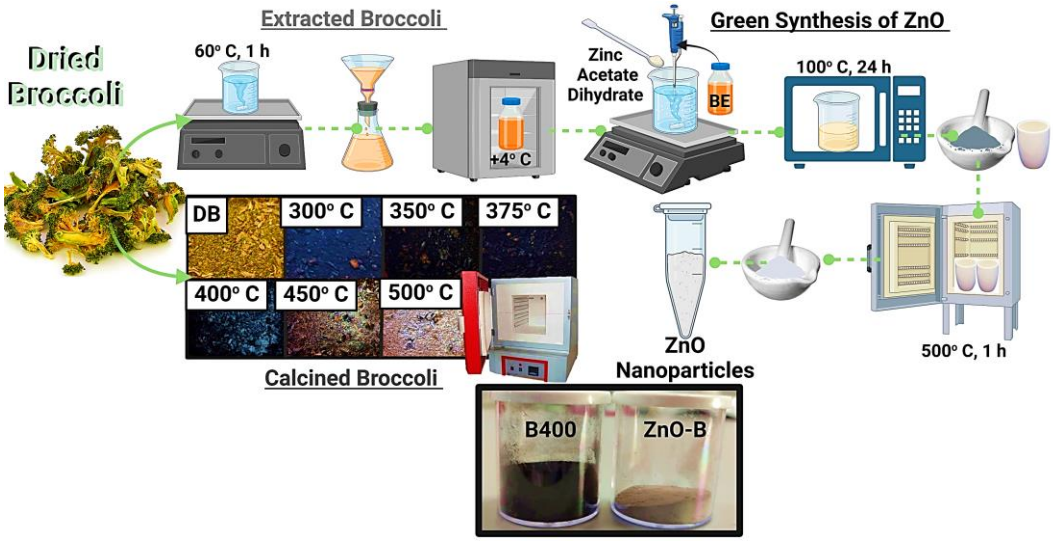


Figure 37: Production of ZnO NPs and broccoli carbon powders [BioRender].

4.2.5. Electrode Preparation

In this work, the potentials of produced ZnO NPs and calcined broccoli powders were first investigated in a three-electrode electrochemical system. Then, instead of conductive carbon black, a slurry was made using calcined broccoli (B400) and ZnO NPs active material. The purpose of this study was to test the idea that calcined broccoli may be utilized to boost the potential of ZnO NPs rather than conductive carbon black.

Slurry preparation for three-electrode system

The electrochemical analytical measurements of the powders were initiated by producing a slurry to be deposited on nickel foams in a three-electrode system. First, nickel foams were cut into 1x2 cm pieces, immersed in a 2 M HCl solution, then cleaned in an ultrasonic mixer for 1 minute. The nickel foams were then rinsed with pure water, followed by ethanol, and dried in a vacuum oven at 80° C. Meanwhile,

to prepare the slurry, 5% PVDF binder, 10% conductive carbon black and 85% active material were weighed and the powders were mixed. 0.5 ml NMP was added and the slurry was left to mix in a magnetic stirrer for 24 hours. The weight of the dried nickel foams before coating was weighed and then each was coated halfway with 30 µl of homogeneously mixed slurry. It was kept in a vacuum oven at 80° C until the three-electrode chemical analysis was performed. To prepare the electrolyte, 6 M KOH was dissolved in distilled water and stirred until it cooled. After all electrochemical materials were prepared, 1 drop of Triton-X, 6 M KOH solution and slurry coated nickel foam were placed in the same beaker and kept in a desiccator for 1 night to activate the surface before electrochemical analysis. Then, electrochemical analysis of the powders was carried out in a three-electrode system. Additionally, the same procedure was repeated with calcined broccoli powder (B400) instead of 10% conductive carbon black and 85% ZnO NPs as an active material *(Figure 38(a))*.

Ink preparation for two-electrode systems in printing micro-supercapacitor devices

Ink preparation optimizations were made for use in the printing of micro-supercapacitor devices. Concentrations were prepared in the ratios of CMC binder and active material added to adjust the viscosity and rheological analyzes were performed.

Table 4: Ink contents and material codes at six different concentrations for rheological analysis.

Exp.Code/Ingredients	**CMC (binder)**	**DW (solvent)**	**ZnO (active material)**	**Calcined Broccoli-B400 (carbon content)**
a	0.16 g	20 ml	0.2 g	1.75 g
b	0.16 g	20 ml	0.2 g	2.30 g
c	0.16 g	20 ml	0.03 g	2.30 g
d	0.16 g	20 ml	0.4 g	3.5 g
e	0.20 g	20 ml	0.4 g	3.5 g
f	0.24 g	20 ml	0.4 g	3.5 g

Inks were prepared in the ratios shown in *Table 4* and the rheological effects of both binder, active material and carbon source were observed. The experimental process was the same for six different ink solutions made in order to determine the most suitable ink viscosity. First, ZnO NPs and calcined broccoli (B400) were weighed in the specified ratios (Zhang et al., 2018). Two powders were mixed well in a beaker with the help of spoons. Then, CMC powder in different concentrations was mixed in pure water for at least one day until it was thoroughly dissolved. After adding 20 ml of CMC binder solution to the powder beaker, each ink was mixed with a magnetic stirrer for 6 hours. Although it was necessary to add less binder in order for the particles to exhibit optimum concentration, the binder ratio was also tested in order to provide sufficient viscosity (*Figure 38 (b)*).

4.2.6. Preparation of Electrolyte

Quasi-solid state gel polymer electrolyte was prepared for use during printing with an extrusion-based 3D printer. For this, first 2 g PVA and 20 ml DW were mixed at 80^{o} C for half an hour with a magnetic stirrer until homogeneously dissolved. When complete dissolution was achieved, 2 ml of 6M KOH solution was added drop by drop and mixed. Stirring continued until it cooled (Idrees et al., 2020, Sun et al., 2023). While the pH value of the 6 M KOH electrolyte solution was 15.45, 2 ml of KOH solution was added to the gel electrolyte to achieve a pH value between 13-14. The preparation steps of slurry and inks are shown in *Figure 38*.

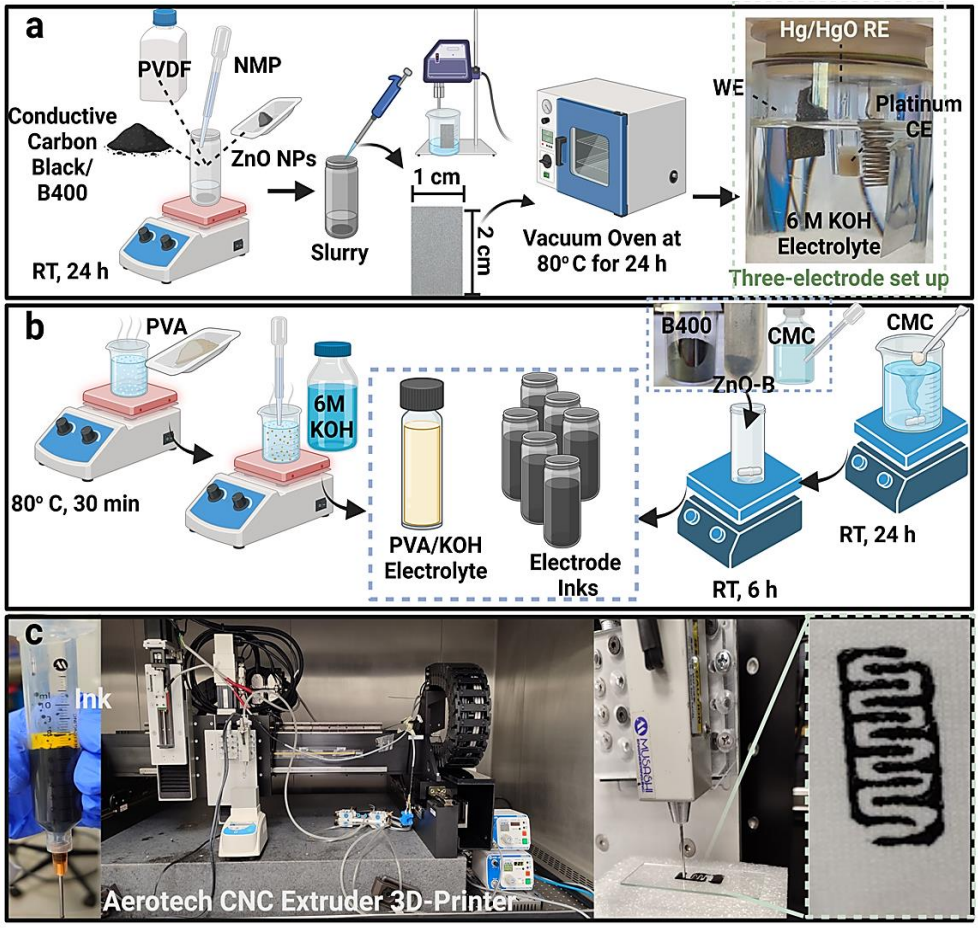


Figure 38: Three-electrode system analysis, ink preparation and ink printing steps: **a** Preparation of slurry using PVDF and NMP to coat ZnO NPs and B400 powders onto nickel foams and electrochemical analysis in the three-electrode system, **b** preparation of electrode ink using ZnO NPs, B400 and CMC for printing and preparation of gel polymer electrolyte, and **c** printing of the ink prepared with an extrusion-based 3D printer on 100% cotton fabric according to the design [BioRender].

4.2.7. Symmetric Micro-Supercapacitor Architecture

The MSC design was inspired by the drawing dimensions used in previous studies (Zhang et al., 2018). First, all drawings were drawn using AUTODESK Fusion 360 software. After saving the drawing in STL file type, the design divided into slices was converted to G-code and previewed with ULTIMAKER CURA program. The desired codes were edited with the NC simulator program and brought to a format suitable for the extrusion-based 3D printer device (*Figure 39*).

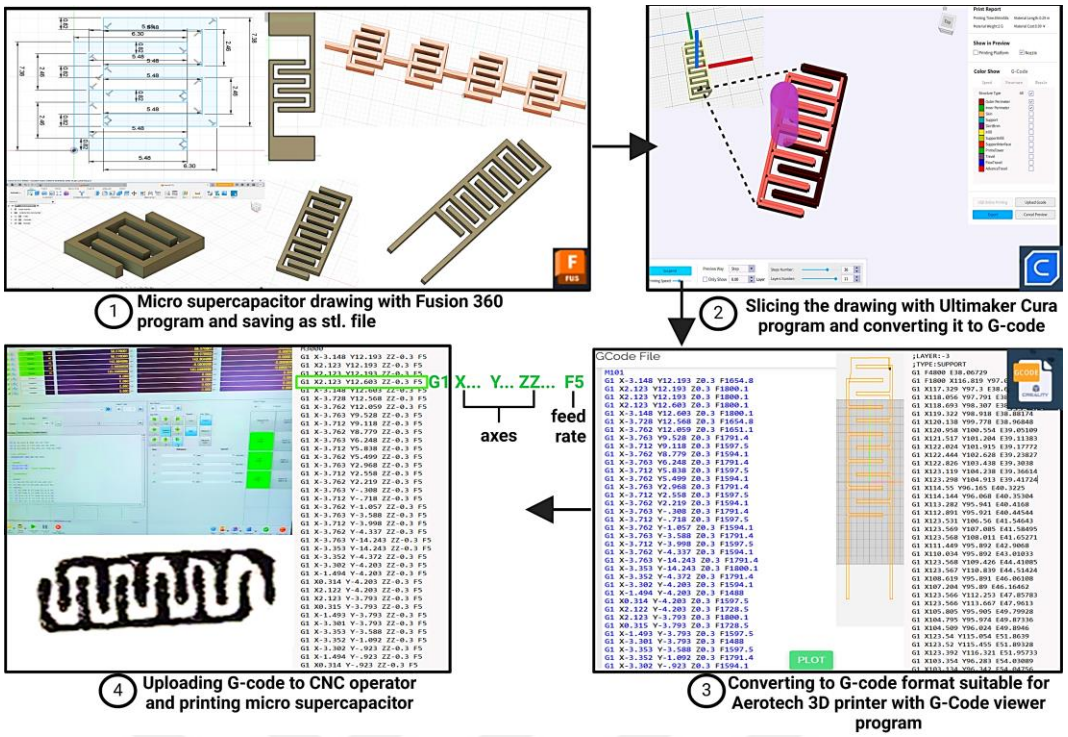


Figure 39: Micro-supercapacitor designs and steps to convert the file into G-code in a suitable format for Aerotech CNC based 3D printer [BioRender].

4.2.8. Printing of Flexible Micro-Supercapacitor Wearable Devices and Post-treatments

A custom 3D printer was used for the printing process. The produced CMC/ZnO/B400 ink was loaded into a syringe fitted with a double thread threaded polypropylene plastic needle tip with an inner diameter of 0.84 mm. The movement of the printing stage was computer-controlled with the developed codes. The distance between the nozzle and the substrate was set to 0.15 mm. The print speed and pressure were 5 mm/s and 0.1 mPa, respectively. The printed ink was then annealed at 60° C for 15 minutes to thoroughly eliminate the solvent. To finish the MSC production, the ion gel PVA/KOH solution was dripped onto the interlocking electrode region and dried at 60° C for 30 minutes to form a gel state (Wu et al., 2023). After drying, it was placed in a PDMS solution (1:10 wt%) for encapsulation and dried at 60° C for 1 hour.

The electrolyte is applied to the electrodes and the spaces between the electrode steps or fingers. The extremely narrow spacing between the electrode stages is intended to provide specific advantages, such as ionic transport. In addition, the printability of several designs was examined. In-plane designs are mostly used in micro-scale and small device applications, as well as wearable technologies in on-chip energy applications (Kamal K. Kar, 2023).

4.2.9. Characterizations

This work includes the characterization of ZnO NPs, BE, calcined broccoli, ink, three- and two-electrode electrochemical studies, as well as electrochemical tests for a flexible MSC wearable devices.

Scanning electron microscopy (SEM) and transmission electron microscopy (TEM) with energy-dispersive X-ray spectroscopy (EDS) analyses

SEM and TEM analyses were performed to interpret the morphology, size and elemental mapping of the produced ZnO NPs and calcined broccoli at different temperatures with EDS analysis. All particles were suspended in 1 ml of ethanol and air-dried on silicone surfaces. The observation was carried out with a nitrogen-cooled Zeiss Ultra 55 Gemini SEM outfitted with an EDAX detector with accelerating voltages of 10 kV. The particles' morphology was also investigated using a JEOL JEM-ARM200CFEG UHR-TEM (fitted with STEM and EDS). The particle size of the produced powders was determined from SEM and TEM pictures using the Image-j image analysis software, which is freely available in the public domain (Avcıoğlu et al., 2022).

X-ray diffraction (XRD) analysis

The ZnO and calcined broccoli particles' crystalline structures were studied using a Bruker D8 ADVANCE X-ray diffractometer (Bruker, Billerica, MA, USA) at 40 KV and 40 MA, using CuKa radiation at 1.5418 Å. The crystallinity values were determined, and the material's amorphous and crystalline properties were examined. XRD patterns of produced ZnO NPs and calcined broccoli were recorded

at room temperature (20-80° 2θ). The calculations were based on Debye-Scherrer's formula **(3)**:

$$\textbf{\textit{Crystallite Size}}\ (\boldsymbol{D}) = \frac{k\lambda}{(\beta \cos\theta)} \qquad \textbf{(3)}$$

where λ is the wavelength of light utilized (CuKα radiation, 1.54 Å), k is the Scherrer's constant (0.94), β is the entire width at half maximum of the selected diffraction peaks corresponding to planes, and θ is the Bragg's angle calculated from the 2θ values (Mousa et al., 2024).

Fourier transform infrared spectroscopy (FTIR) analysis

Fourier Transform Infrared Spectroscopy (IRAffinity-1S Shimadzu) was used to examine the chemical bonds of ZnO nanoparticles, broccoli juice, calcined broccoli, inks at various concentrations, and gel electrolyte in the 600-4000 cm^{-1} range (N. Funda AK AZEM, Işıl BİRLİK, 2018).

Thermogravimetry differential thermal (TG/DTA) analysis

To assess the thermal degradation of zinc oxide powder and dried broccoli powder before calcination, thermogravimetric analysis (TGA-Exstar 6300) was carried out in air at a heating rate of 5° C min^{-1}. In addition, differential thermal analysis (DTA-Netzsch STA 449C) was carried out on the same powders from room temperature to 800° C in an O_2 environment at a heating rate of 5° C min^{-1}. The optimal temperature for the calcination procedure was calculated based on thermal degradation evaluation (Avcioglu et al., 2020).

Brunauer-emmett-teller (BET) analysis

The effects of annealing temperature on surface area and porosity were examined using BET on a Micrometrics ASAP 2020 apparatus. The samples were degassed at 150° C for 24 hours under 0 to 950 mmHg pressure using the Micrometrics VacPrep061 Sample Degas System in N_2 atmosphere (L. Khezami, 2018). In order to investigate the effect of different calcination temperatures on porosity and surface area, BET analyses were performed on broccoli powders calcined at 300, 375 and 400° C and the temperature with the highest porosity and surface area was selected to be used in the electrode. BET analysis is very important for electrodes

since the passage of ions between the electrode and electrolyte in the electrochemical system is related to porosity and energy storage is directly proportional to the surface area.

Raman analysis

Raman spectroscopy is one of the most non-destructive and effective techniques for extracting structural information from particles (Ajayi et al., 2022). For Raman analysis, a hybrid Renishaw Raman apparatus was employed. The surface of the three different calcined broccoli powders were smoothed after they were added to the microscope section. 10% laser power was used for the Raman analysis, which covered the 100–3200 cm^{-1} range.

Rheology analysis

Rheology analyses were performed to understand the viscosity, and shear thinning values of inks with different concentrations prepared using ZnO NPs, calcined broccoli and natural polymer CMC for 3D printing at room temperature. For this purpose, MCR 92 EDU Anton Paar device was used.

Electrochemical analyses

In this thesis, two different measurement systems are used. The first, the three-electrode system, is typically used for identifying the electrochemical properties of powders for the electrodes which are ZnO NPs and calcined broccoli, and the two-electrode system is used to test the design of the prototyping device or the ultimate symmetric or asymmetric devices (Kamal K. Kar, 2023). In the three-electrode system, there is a working electrode (WE: ZnO and B400 powders), a reference electrode (RE: Hg/HgO), and a counter electrode (CE: Platinum), whereas the two-electrode system has positive and negative electrodes (Kamal K. Kar, 2023). Cyclic voltammetry (CV), Electrochemical Impedance Spectroscopy (EIS), Galvanostatic Charge/Discharge (GCD), energy density, power density, and specific capacitance values were used to study the electrochemical responses of ZnO NPs, calcined broccoli, and flexible symmetric MSC devices under aerobic circumstances (Kamal K. Kar, 2023). CV studies were carried out in in 6M KOH with a potential window range of -0.6 V to +0.6 V and scanned at different rates (5-200 mV/s). A Metrohm/Autolab potentiostat was used to acquire the voltammograms, which were

coupled inside the 6 M KOH electrolyte (Ajayi et al., 2022). Electrochemical analysis measurements were measured with Intello and NOVA software programs. Furthermore, measurements were conducted in a three-electrode system by covering nickel foams with the PC material ZnO NPs and using carbon source calcined broccoli powder as the EDCL material. The effect of a slurry produced with calcined broccoli rather than conductive carbon black was then investigated. ZnO NPs and calcined broccoli were also used in device analyses, both symmetric and asymmetric. Finally, two-electrode electrochemical evaluations of flexible, symmetric, quasi-solid state micro-supercapacitor wearable devices were carried out. Comprehensive electrochemical analyses were used to determine the potential of green synthesis, natural polymer binders, and carbon recovery from recyclable plant wastes for energy applications. All calculations were made with the formulas given below for three-electrode and two-electrode systems.

Three electrode system formulas:

The formula is used to calculate capacitance from CV analysis **(4):**

$$\boldsymbol{Cs}: \frac{1}{\boldsymbol{m} \times \boldsymbol{\upsilon} \times \boldsymbol{\Delta V}} \int_{Vi}^{Vf} \boldsymbol{idV} \quad (\mathbf{4})$$

$\int_{Vi}^{Vf} idV$ is the integrated area under the CV curve, υ is the scan rate (mVs^{-1}), ΔV is the voltage window (V), and m is the electrode's active mass (g). For three-electrode systems, only one electrode mass is considered, whereas for two-electrode configurations both electrode mass is taken into consideration to compute the appropriate capacitance. The capacitance of the electrode material is calculated using the following equations based on the GCD curves **(5)**:

$$\boldsymbol{Cs}: \frac{\boldsymbol{I} \times \boldsymbol{\Delta t}}{\boldsymbol{m} \times \boldsymbol{\Delta V}} \quad (\mathbf{5})$$

wherein I: applied constant current (A) and Δt: discharge duration (excluding iR drop). Energy density (E_d), power density (P_d), and Coulombic efficiency (η) values were also calculated from the GCD analysis **(6), (7)** and **(8),** respectively:

$$\boldsymbol{Ed}: \boldsymbol{Cs\ x}\ \frac{1}{2\boldsymbol{x}3.6}\ \boldsymbol{x}\ (\boldsymbol{\Delta V})^2 \quad (\mathbf{6})$$

$$\boldsymbol{Pd}: \frac{\boldsymbol{Ed\ x}\ 3600}{\boldsymbol{\Delta t}} \quad (7)$$

$$\boldsymbol{\eta}: \frac{\boldsymbol{td}}{\boldsymbol{tc}} \quad (8)$$

where td is the discharging time and the tc is charging time (Kamal K. Kar, 2023). Coulombic efficiency is commonly used to evaluate charge storage efficiency and cycle stability of devices and electrode materials. In addition, the capacitance values calculated from the GCD analysis were compared for the actual values of energy and power density, taking the current density difference as reference (Kamal K. Kar, 2023).

Two electrode system formulas:

In the two-electrode system, specific capacitance **(9),** energy **(10)** and power density **(11)** calculations for the devices are calculated with the following formulas, respectively. Ed and Pd are normally calculated only for two-electrode systems, i.e. devices (Kale et al., 2023).

$$\boldsymbol{Cs}: 4\text{x}\frac{\int \boldsymbol{I} \times \boldsymbol{\Delta t}}{\boldsymbol{m} \times \boldsymbol{\Delta V}} \quad (9)$$

$$\boldsymbol{Ed}: \boldsymbol{Cs\ x}\ \frac{1}{8}\ \boldsymbol{x}\ (\boldsymbol{\Delta V})^2 \quad (10)$$

$$\boldsymbol{Pd}: \frac{\boldsymbol{Ed}}{\boldsymbol{\Delta t}} \quad (11)$$

4.3.Results and Discussion

4.3.1. Characterizations of ZnO Nanoparticles

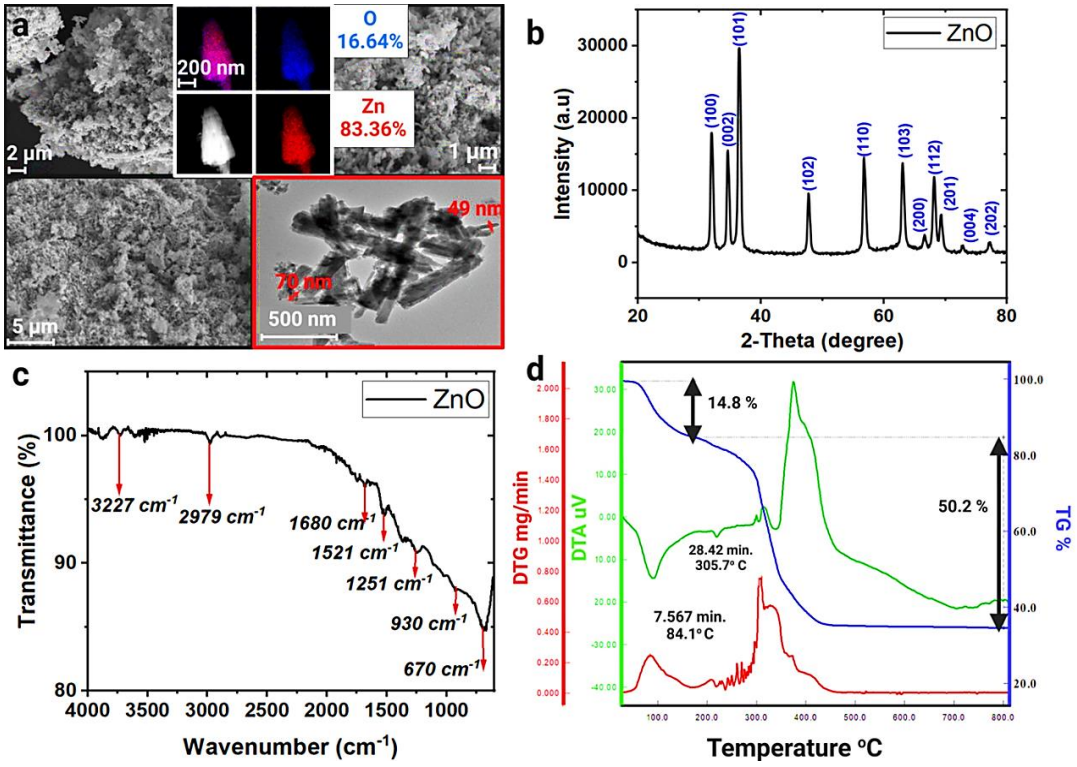


Figure 40: ZnO NPs characterizations: **a** SEM, TEM and EDS analyses at different magnifications, **b** XRD analysis in the (20-80) 2θ range, **c** FTIR analysis in the 4000-600 cm^{-1} band gap and d TG/DTA analysis showing mass loss with temperature [BioRender].

Since the production technique was different from the first part (*Figure 10*), the analyses were repeated for newly produced particles and more detailed analyses were performed, as the ZnO nanoparticle would give different characterization results. *Figure 40(a)* shows the SEM image of ZnO nanoparticles at 4.00, 10.00 and 20.00 kX magnifications, TEM image at 200 nm, and EDS analysis. SEM and TEM pictures revealed that ZnO NPs were generated in a uniformly distributed, conical-rod-like configuration. The ZnO NPs formed in this study had a rod-like structure, similar to the chemical technique, however those made via green synthesis were found to be spherical in comparison to other investigations. Even NPs between 5

and 20 nm could be synthesized using BE, according to a review of ZnO NPs made with BE and zinc chloride heptahydrate source in the literature (Osuntokun et al., 2019). Green synthesis produced nanoparticles that were at a more nano level than ZnO NPs made by chemical and physical methods (Mousa et al., 2024, Naiel et al., 2022). An average crystallite size of 17 nm was determined during this investigation. *Figure 40(b)* shows the XRD analysis of ZnO NPs (Naiel et al., 2022). At 2θ values of 31.96°, 34.59°, 36.49°, 47.81°, 56.73°, 63.02°, 66.6°, 68.11°, 69.38°, 72.81°, and 77.19°, ZnO patterns displayed distinct peaks that could be attributed to the (100), (002), (101), (102), (110), (103), (200), (112), (201), (004), and (202) planes of hexagonal wurtzite phase ZnO. The powder diffraction standard reported for the hexagonal phase of ZnO nanoparticles (JCPDS 36-1451) is in good agreement with the diffraction peaks (Kırkbınar et al., 2023). In addition, crystallinity ratio and ZnO NPs crystallite size were calculated with Debye–Scherrer's *Equation (3)*. It was observed that the particles were 84.86% crystalline and 15.14% amorphous (Osuntokun et al., 2019). Furthermore, *Figure 40(c)* displays the prepared ZnO NPs' FTIR spectra. The stretching frequency of the hydroxyl group (O–H) in the ZnO NPs made with BE was 3227 cm^{-1}. The alkene group's (C=C) asymmetric stretching frequency originated at 1680 cm^{-1}. At 1521 cm^{-1}, the N–H bending was detected. The Zn-O stretching bands are responsible for the peaks observed at about 600 cm^{-1}. Other peaks may show the existence of metabolites including alkaloids, flavonoids, polyphenols, and carboxylic acids, based on the FTIR data. Zinc ions were reduced to ZnO NPs with the aid of these substances, primarily flavonoids and other phenolics (Mousa et al., 2024). The presence of free amino and carboxylic groups interacting with the zinc surface is most likely what gives the produced ZnO NPs their stability. Furthermore, the medium's proteins stabilize ZnO NPs by covering them with a sheath that stops them from aggregating. Previous research on this topic suggests that the molecules' phenolic groups are responsible for the reduction process, while the durability of ZnO nanoparticles may be due to free amino and carboxylic groups (Mousa et al., 2024). As seen in *Figure 40(d),* a thermogravimetric examination was performed to ascertain the heat stability of green produced ZnO NPs. As the dried powder of ZnO NPs was heated from room temperature to 800° C, the weight loss was recorded. The heating process was conducted at a temperature scanning rate of 5° C/min in an oxygen atmosphere (Naiel et al., 2022). Using TGA analysis, it was

demonstrated that green produced ZnO NPs had excellent heat stability. In the temperature range between room temperature and 800° C, a progressive weight loss of about 14.8% of the actual weight was assumed to be caused by the loss of organic matter and moisture content. The degradation of organic groups involved in the production of ZnO NPs utilizing plant extract, on the other hand, was responsible for the notable weight loss (~50%) that was noted between 350 and 600° C, as demonstrated by the research in the literature (Naiel et al., 2022).

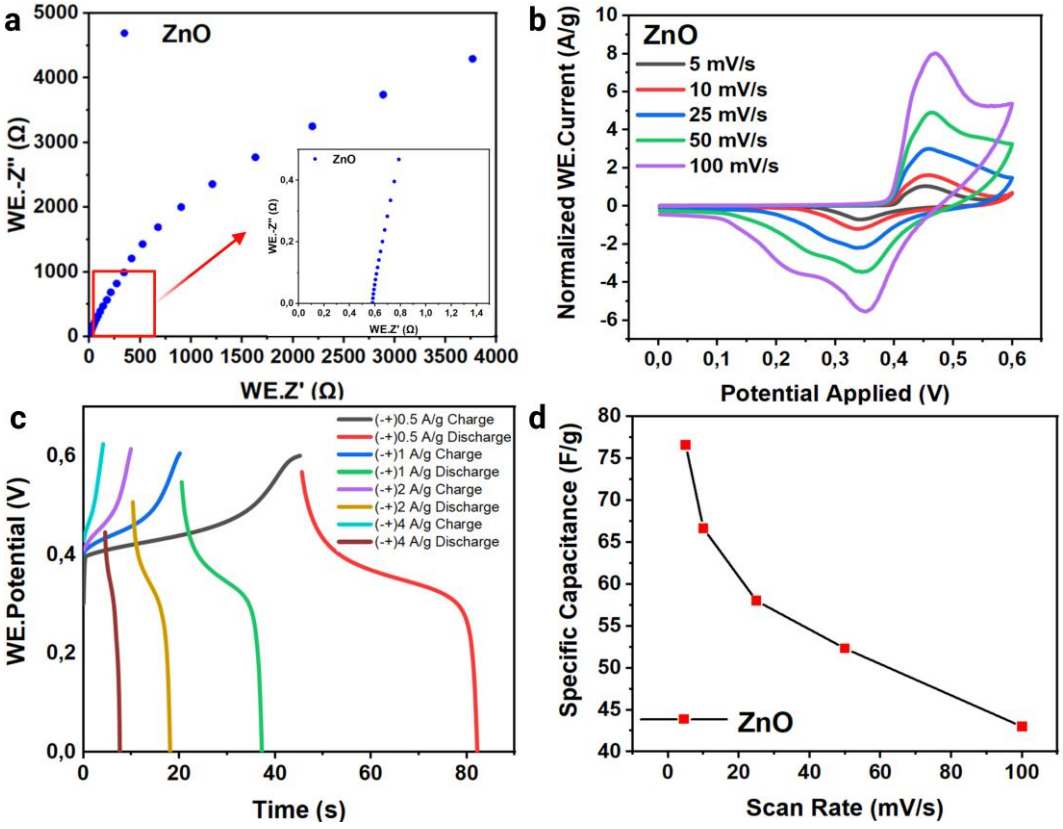


Figure 41: Electrochemical analysis of ZnO NPs powder in a three-electrode system: **a** EIS, **b** CV at different scan rates in the 0-0.6 voltage range, **c** GCD plots at 0.5, 1, 2, and 4 A/g current density values, and **d** specific capacitance values calculated from the CV plot [BioRender].

Additionally, endothermic and exothermic reactions and their temperatures in DTA analysis are shown in Figure d, respectively. DTG analysis is also included in the same table. The highest weight loss values of the material were shown in this analysis as 84.1° C at 7.56th minute and 305.7° C at 28.42nd minute. After characterization of ZnO nanoparticles, powders were added to slurry prepared with conductive carbon black, PVDF, and NMP and coated on nickel foams for electrochemical analysis in a three-electrode system. ZnO NPs measured in 6 M

KOH electrolyte were used as the working electrode, the platinum plate counter electrode, and the Hg/HgO reference electrode in a three-electrode system. In addition, nanoparticles were measured in the 0-0.6 voltage range. EIS, CV, and GCD analyses were performed, respectively, and specific capacitance, energy density, and power density values were calculated.

EIS is a frequency domain method for determining the impedance of voltage across a fixed potential. The measurement findings generate Bode and Nyquist charts, which depict the relationship between phase angle and frequency, as well as the imaginary and real components of the material impedances (Kamal K. Kar, 2023). The Nyquist plot for EIS of ZnO NPs is explained in *Figure 41(a)*. It showed a small semi arc at very high frequency and continued as a straight line like the pseudocapacitor materials at low frequency (Mahmood, Baig, 2024). The connecting point is on the Z-axis, which determines the electrochemical resistance (Rs). The semicircle diameter indicates the high-frequency range charge transfer resistance (Rct), whereas the linear line explains the Warburg impediment in the low frequency range (Mahmood, Baig, 2024). The Rs value for ZnO was found to be 0.002325 Ω. The Rs value describes the kinetics of the material and indicates faster charge transfer (Mahmood, Baig, 2024). CV analysis determines the potential window, which includes the electrode material's capacitance and voltage range (ΔV). For three-electrode systems, CV records the voltage between the reference and working electrodes, whereas for two-electrode systems, CV records the cathode and anode current between positive and negative. In supercapacitors, EDLC electrodes have a fully rectangular CV, whereas PC electrodes have a quasi-rectangular CV due to faradic responses (Kamal K. Kar, 2023). As specific capacitance (Csp) grows, Csp gradually declines as current density and scan rate increase; thus, at low current density and scan rate, electrolytic ions penetrate the electrode's entire surface more steadily. High scan rates hinder the movement of electrolytic ions, negatively impacting redox and energy storage capacity (Mahmood, Baig, 2024). *Figure 41(b)* adds the CV analysis at different scanning speeds for ZnO powder. In CV analysis, as the scan rate increases, the area under it increases, but the specific capacitance values decrease because the ions are not allowed to penetrate sufficiently. While the specific capacitance was found to be 75.176 F/g at 5 mV/s, it was calculated as 43.012 F/g at 100 mV/s scan rate (*Figure*

41(d)). For more accurate measurements, the GCD graph was used (Kale et al., 2023). In CV analysis, oxidation and reduction peaks were also seen. Oxidation (anodic) peaks increased as positive current as scan rate increased. Similarly, reduction (cathodic) peaks decreased as negative current as scan rate increased. GCD analysis uses factors such as capacitance, ohmic resistance (iR drop), and peak voltage (V0) of the working electrode to calculate the energy and power density of the devices (Kamal K. Kar, 2023). While the GCD graph in EDLC electrodes is in the shape of an inverted V, the graphs of PCs are more curved. In *Figure 41(c)*, mostly pseudocapacitor-battery type GCD graph is observed. The discharge time at 0.5 A/g current density value is found as 36.999 seconds. As the current density increases, the discharge time also starts to shorten.

4.3.2. Characterizations of Broccoli Extract and Biowaste Calcinated Broccoli

The BE used in the manufacture of ZnO NPs, as well as biowaste broccoli powders calcined at various temperatures (300, 350, 375, 400, 450, and 500^{o} C), were thoroughly described and studied. Since various chemicals must be used to activate carbon, biowaste is intended to obtain resources only by converting waste into carbon in terms of sustainability and eco-friendliness. First, when the powders' appearances were analyzed, as shown in Figure, it was discovered that powders calcined at 300, 375, and 400^{o} C produced the best results. The broccoli bits stayed green after low-temperature calcination, whereas high-temperature calcination resulted in oxidation and the material's removal as a gas or glassy structure. As a result, thorough analyses were performed on the powders calcined at 300, 375, and 400^{o} C. The table shows the BET analysis results for three different powders in *Table 5*.

Table 5: BET analysis results for B300, B375 and B400 powders.

Calcination temperature (^{o}C)	BET Surface Area (m^2/g)	Total Pore Volume (cm^3/g)	Average Pore Width (nm)	BJH Pore Diameter (nm)
300	0.4857	0.001163	15.9288	9.5811
375	1.4664	0.002531	16.3972	6.9042
400	3.3512	0.005760	18.0036	6.8745

Broccoli powder calcined at 400° C was used as a carbon source in electrode production because the powder calcined at this degree had the highest surface area and pore structure. However, other analyses were also performed for B300, B375 and B400 powders in order to make a better decision.

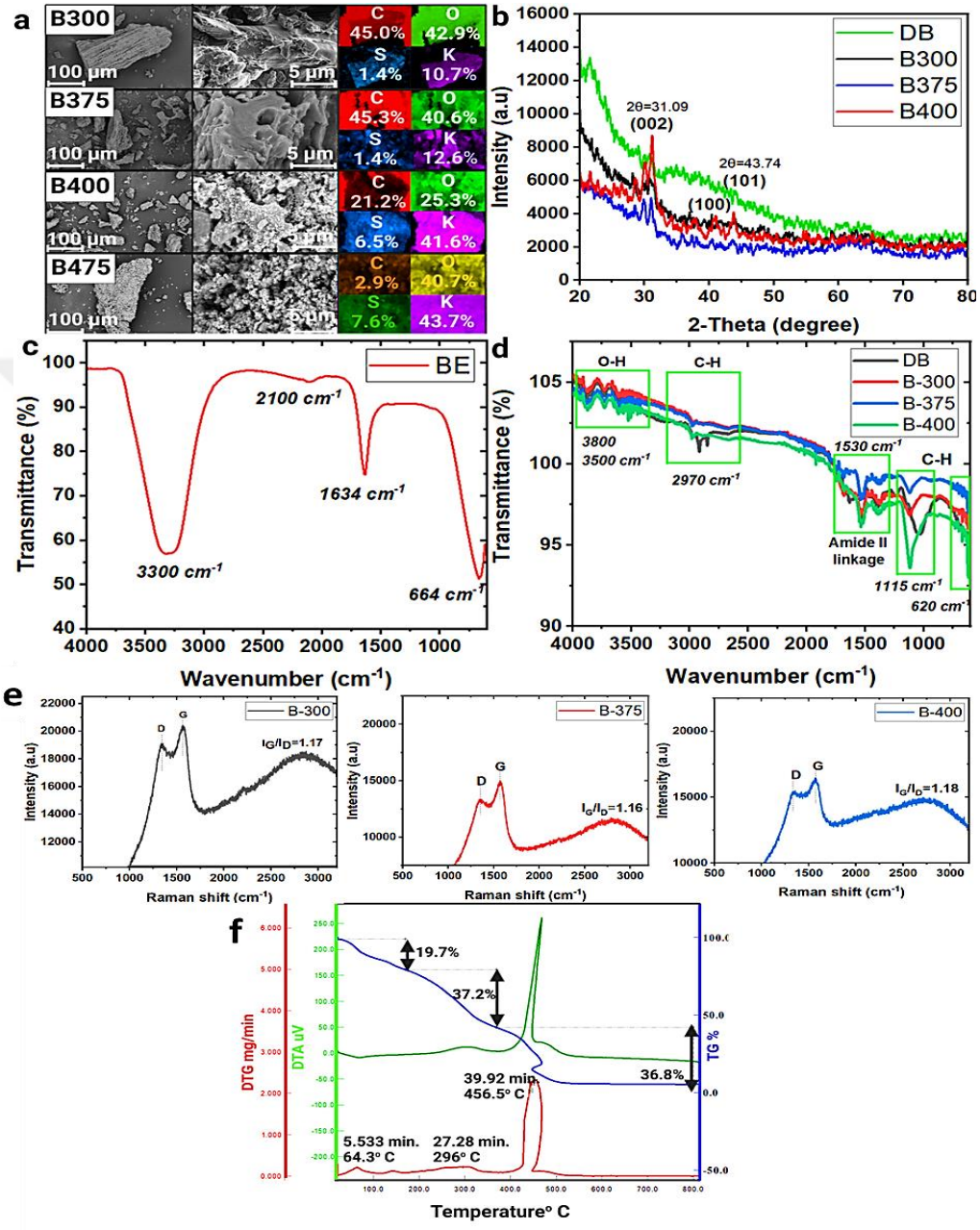


Figure 42: Morphological and chemical analyses of broccoli powders and BE calcined at different temperatures: **a** SEM and EDS analysis for four different powders, **b** XRD analysis of dried broccoli, B300, B375 and B400 powders in the 2θ: 20-80 range, **c** FTIR analysis of BE in the 4000-600 cm^{-1} band range, **d** FTIR analysis of calcined and non-calcined broccoli powders, **e** Raman analyses of powders, and **f** TG/DTA analysis of dried and non-calcined broccoli powder [BioRender].

In the literature, the characterization of biowaste broccoli calcined at various temperatures and its usage as a carbon source has never been mentioned or examined. As a result, studies on acquiring carbon sources from similar biowastes were considered while developing calcination. *Figure 42(a)* shows the SEM and EDS results of the powders. The EDS analysis results show that as the calcination temperature increases, the carbon and oxygen ratio in the structure decreases significantly. In addition, with the increase of calcination temperature, smaller particles were formed, and this increased the surface area. Since the increase in surface area would have high capacitance values in electrochemical terms (Minakshi et al., 2019). B400 powder was selected as the most suitable powder. In *Figure 42(b),* the XRD results of the powders are shown. From the XRD graph, crystallinity was calculated as approximately 1% for B300 powder, 6% for B375 powder and 16% for B400 powder. The diffraction patterns in the XRD result were found to be similar to the peaks corresponding to the standard JCPDS file (41–1487) for the (002), (100) and (101) crystal planes (Kalagatur et al., 2017). *Figure 42(c)* shows the FTIR analysis result of BE. The FTIR spectra of BE revealed bands at 3300 cm^{-1}, 2100 cm^{-1}, 1634 cm^{-1}, and 664 cm^{-1}. The 3300 band was assumed to represent a -NH stretching of the amide (II) band. Furthermore, the peak at 1634 cm^{-1} revealed the O-H stretching peaks of alcohols and phenols (Golli et al., 2023). Because of the bio-extract present in the sample, the C-Br-stretching vibration was assumed to constitute a chemical bond in the band gap seen at 664 cm^{-1} The C-C bond stretching of the alkene produced the peak at 2100 cm^{-1}. The plane bending vibration of aromatic primary amines was also seen to be generated by the C-H bond, according to literature (Piruthiviraj et al., 2016). *Figure 42(d)* also includes the FTIR analyses of dried (DB), and calcined B300, B375 and B400 powders, respectively. The graph, which matches well with the FTIR analysis of porous carbon in the literature, consists of hydroxyl group, aliphatic (-CH), aromatic and -CH bonds, respectively. Differences in calcination temperature were observed, especially in the fingerprint region. It was observed that the aromatic C-O bonds in the 1115 cm^{-1} band gave the most peak in B400 powder (Suresh Kumar Reddy et al., 2014). The Raman spectrum contains two strong peaks, D and G. The relative strengths of these vibrations vary according to crystallinity. The D and G intensities in the graphs correspond to the structure of activated carbon described in the literature (Dychalska et al., 2015, Su et al., 2017). The degree of graphitization of a

carbon material is often determined by the I_G/I_D value in Raman spectra, where I_G represents the sp^2-bonded carbon atoms in the hexagonal graphite ring and I_D represents the vibrations of the sp^3-bonded carbon atoms of defects and disorder. As demonstrated in *Figure 42(e),* the I_G/I_D ranking of carbon materials is B400>B300>B375, implying that B400 would have the highest adsorption selectivity coefficient and increase hydrogenation (Dychalska et al., 2015). *Figure 42(f)* shows the TG/DTA analysis of dried broccoli from room temperature to 800° C. The TG curve demonstrates three weight loss phases at 0∼200, 200∼400, and 400∼800° C. These indicate the loss of physically absorbed water and crystal water, the generation of CO_2, and the degradation of biomolecules into carbon. The DTA curve revealed three major endothermic peaks at 64.3, 296, and 456.5° C, which corresponded to the procedure outlined above. Weight loss becomes minimal above 450° C. However, because the carbon content reduced as the temperature climbed, it was assumed that the optimal calcination temperature would be 400° C (Su et al., 2017).

Figure 43 shows the three-electrode electrochemical analysis of B400 powder coated with PVDF and NMP as slurry on nickel foams in 6 M KOH electrolyte. First of all, the EIS graph is added in *Figure 43(a)*. It is observed that the straight line (Warburg resistance-diffusion resistance) in the low frequency region is steeper than the ZnO NPs EIS graph and more similar to the EDLC type (Kamal K. Kar, 2023). Additionally, the Rs value of B400 powder was 0.008015 Ω. In *Figure 43(b)*, CV analyses were performed for B400 powder at different scan rates in the 0-0.6 voltage range. It was observed that the oxidation peak was higher and the area was wider compared to ZnO NPs. For example, while the specific capacitance was found to be 143.67 F/g at 5 mV/s, it was calculated as 47 F/g at 100 mV/s. In addition, the positive and negative voltage ranges of B400 powder were tested separately. As seen in *Figure 43(c), (d)* and *(e)*, it was determined that the performance of B400 powder in the 0-0.6 positive voltage range was more efficient. In *Figure 43(f)*, GCD analysis was measured at different current density values. When compared to ZnO NPs, a discharge time of 19.999 seconds was measured at a current density value of 0.5 A/g and it was determined that it had a shorter discharge feature.

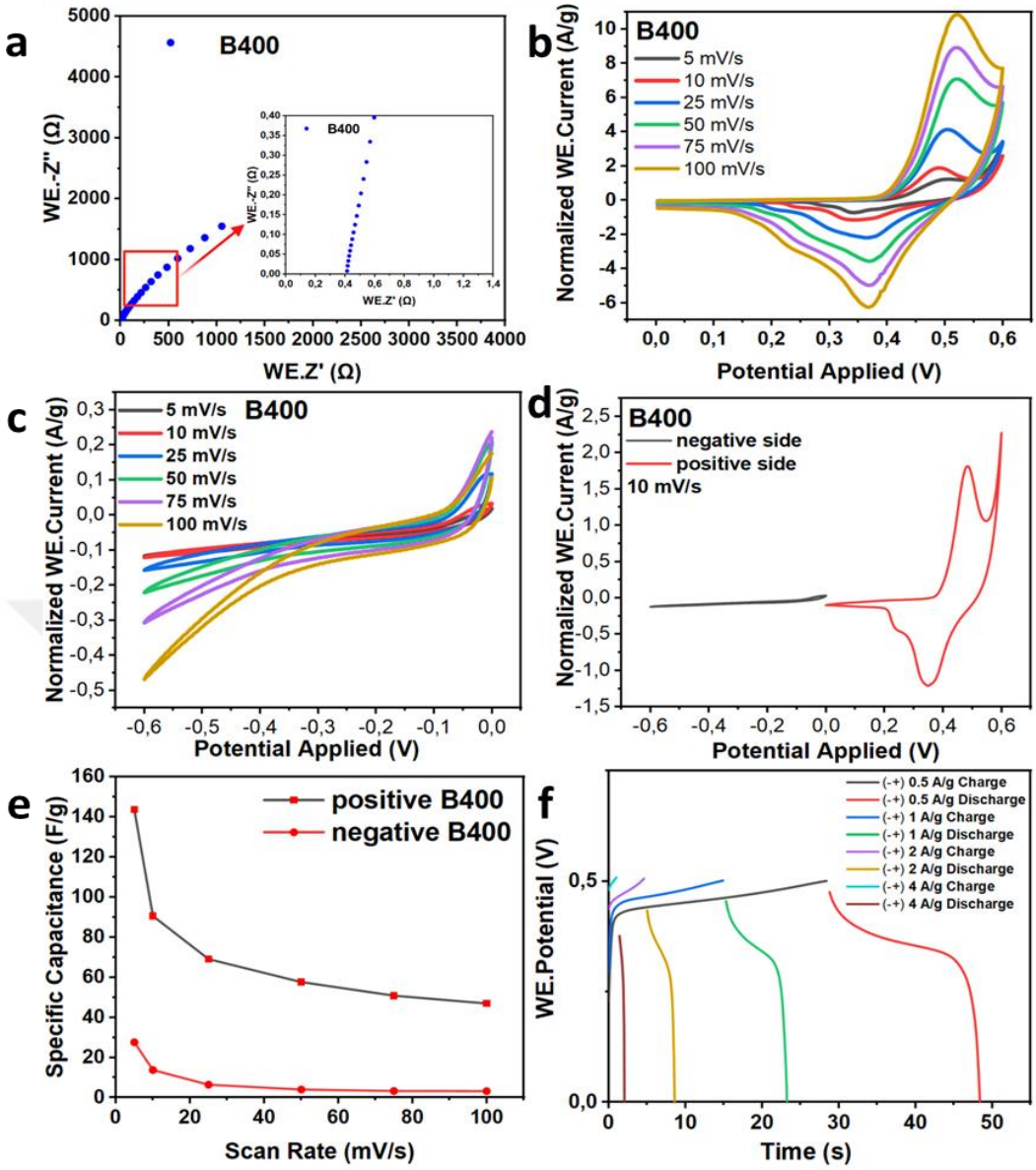


Figure 43: Electrochemical analysis of B400 powder in a three-electrode system: **a** EIS, **b** CV analysis at different scan rates in the voltage range of 0-0.6, **c** CV analysis at different scan rates in the voltage range of -0.6-0, **d** comparison of CV graphs at 10 mV/s scan rate in the positive and negative regions, **e** specific capacitance values calculated from CV graphs in different regions, and **f** GCD graphs at current densities of 0.5, 1, 2, and 4 A/g [BioRender].

In the continuation of the study, ZnO NPs shown in *Figure 41* were slurry prepared with PVDF and NMP using the synthesized B400 instead of conductive carbon black, and three-electrode electrochemical analyses were carried out by coating them on nickel foams at the same ratios. In *Figure 44*, the electrochemical analysis of ZnO and ZnO/B400 powders are compared. The Rs value was found as 0.00582 Ω from the EIS graph for ZnO/B400 powder. It was also calculated that the specific

capacitance value of ZnO/B400 powder increased from 64.37 F/g to 74.64 F/g by increasing the ZnO NPs property up to 10 mV/s scan rate value.

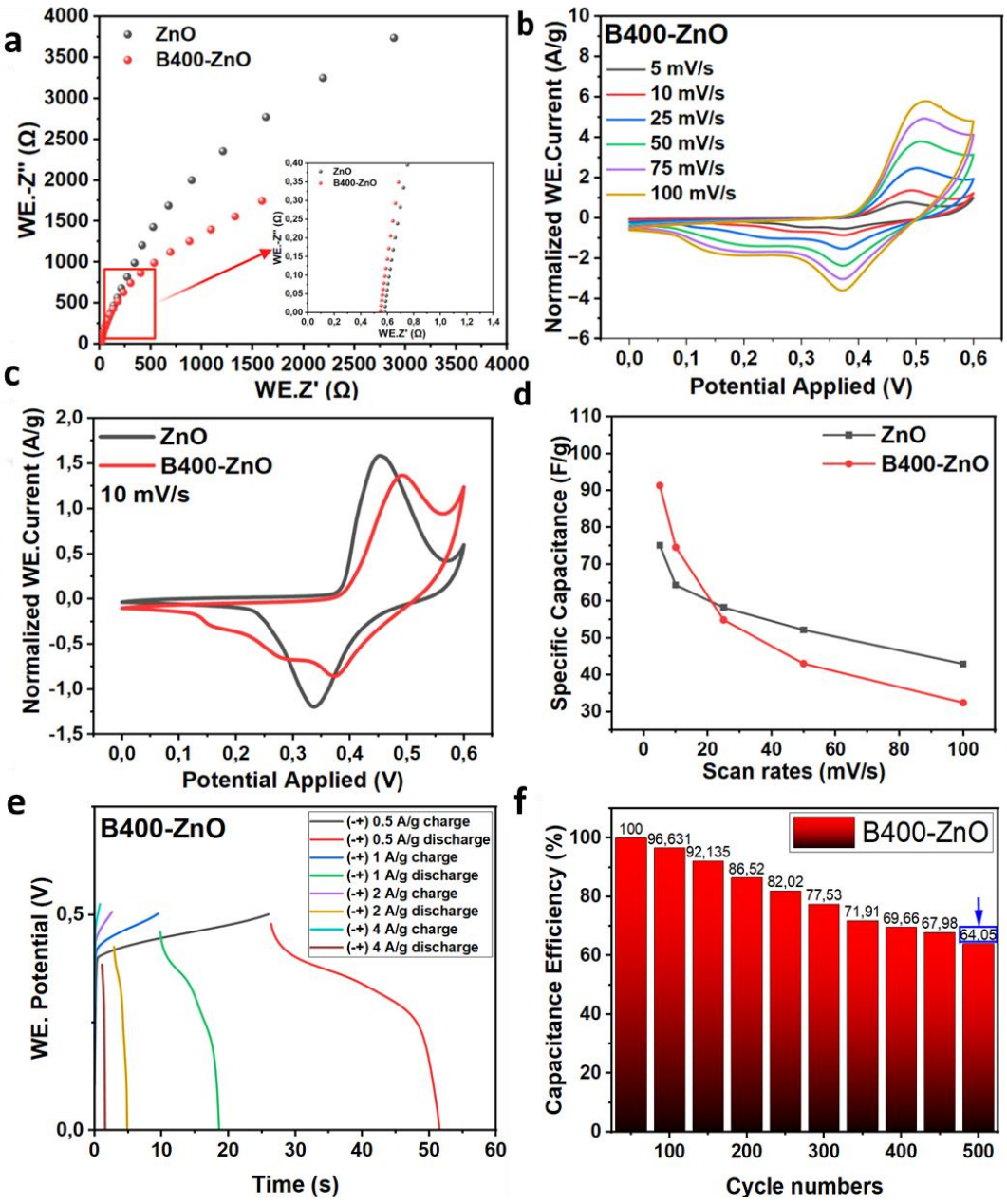


Figure 44: Electrochemical analysis results of nickel foams prepared and coated by adding B400 powder instead of conductive carbon black during the slurry preparation of ZnO NPs powder in the three-electrode system: **a** EIS comparison of ZnO and ZnO/B400 powders, **b** CV analysis of ZnO/B400 powder in the 0-0.6 voltage range at different scan rates, **c** CV comparison of ZnO and ZnO/B400 powders at 10 mV/s scan rate, **d** comparison of specific capacitance values of ZnO and ZnO/B400 powder, **e** GCD analysis at different current density values, and **f** calculation of efficiency according to specific capacitance values between 50-500 cycles [BioRender].

In addition, the CV study revealed that B400 powder increased the pseudocapacitor properties. According to the literature, employing B400 powder instead of conductive carbon black can result in electrodes with superior characteristics. Since ZnO/B400 powders will be used together in the printing of micro-supercapacitors, the analyses of the two powders are quite important. In the *Figure 44(e)* graph, GCD analysis was performed according to the 0-0.6 voltage range and 0.5, 1, 2, and 4 A/g current density values. In the *Figure 44(f)* graph, specific capacitances between 50-500 cycles were calculated according to the discharge time and the capacitance efficiency was added as a column chart according to these values. Stability test was performed up to 500 cycles at 1 A/g current density and 0.5 voltage window. In the 50th cycle, the capacitance of the powder with a discharge time of 8.9 seconds was found to be 17.8 F/g. In the 500th cycle, a capacitance of 11.4 F/g was calculated with a discharge time of 5.7 seconds. The fact that 64.05% efficiency was obtained at the end of 500 cycles revealed the potential of the powders. After analyzing the powders in the three-electrode setup, two-electrode electrochemical investigations were conducted.

Two-electrode device experiments were carried out symmetrically and asymmetrically in 6M KOH electrolyte. These analyzes, which show the direct performance of the powders without coating, measured the symmetrical movements of ZnO NPs powders and the asymmetric movements of ZnO NPs-B400 powders. The symmetric device of ZnO NPs was analyzed by selecting the voltage window 1V at a scan rate of 100 mV/s, and the specific capacitance was calculated to be 44.03589 F/g. At the same scan rate, asymmetric devices using B400 and ZnO powders produced a specific capacitance value of 28.18 F/g. The asymmetric device's specific capacitance value at a scan rate of 10 mV/s was calculated to be 56.16 F/g. In addition, asymmetric devices were created using B300 and B375 powder. The study found that B300 powder had higher capacitance values at high scan rates, but similar values at low scan rates (*Figure 45(c)*). *Figure 45* shows the device analysis results for the powders. In *Figure 45(a),* it is seen that B400 device has a more pronounced semicircle (transfer resistance due to electron transfer at electrode/electrolyte interface) at high frequencies, but B375 powder shows better pseudocapacitance properties at low frequencies. In *Figure 45(b),* the comparison of %capacity retention values are shown. It was noticed that the cycle stability of

the powder prepared with B400 was better. As the cycle number increased, the %capacity retention value remained almost constant for the device with B400 powder. Furthermore, asymmetric CV measurement of the device revealed typical quasi-rectangular CV profiles, indicating EDLC behavior with minor Faradaic contributions to charge storage in *Figure 45(c)* (Avcıoğlu et al., 2023).

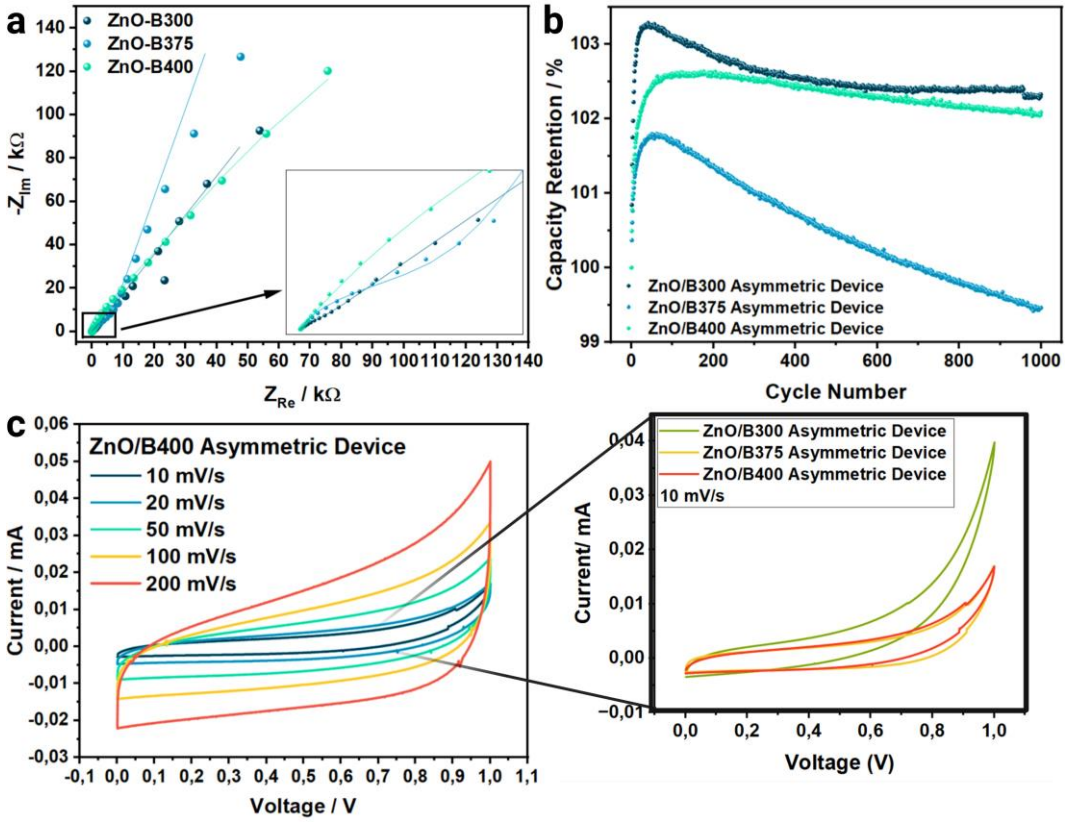


Figure 45: Electrochemical analyses of symmetric and asymmetric devices with ZnO NPs in two-electrode system: **a** EIS analyses of asymmetric devices made with B300, B375 and B400 powders, **b** %capacity retention values of asymmetric devices with ZnO NPs in broccoli powder calcined at different temperatures, and **c** CV analysis of ZnO/B400 asymmetric device at different scan rate values and comparison of CV analysis of three different devices at 10 mV/s scan rate [BioRender].

In addition, the energy and power density values of the devices were calculated. The specific capacitance values of 54, 58 and 56 F/g for B300, B375 and B400 powders at 10 mV/s scan rate were used, respectively, and the discharge times in the GCD analysis were 0.044, 0.052 and 0.072 seconds. It was found that the ZnO/B400 asymmetric device with the longest discharge time had the lowest power density value of 392.2 kW/kg. In addition, the device prepared with B400 had the second highest energy density value of 7.8 Wh/kg. After studying the powders'

three- and two-electrode electrochemical analyses, the two-electrode analyses of flexible, symmetric, quasi-solid-state, wearable micro-supercapacitor devices were measured and examined.

Table 6: Specific capacitance, energy and power density values calculated from GCD graphs according to current density values for powders.

Current Density(A/g)	ZnO NPs	B400	ZnO/B400
0.5	Csp: 33.635 F/g Ed: 1.68 Wh/kg Pd: 163.634 W/kg η: 0.819	Csp: 18.1812 F/g Ed: 0.9091 Wh/kg Pd: 163.643 W/kg η: 0.7092	Csp: 22.9085 F/g Ed: 1.1454 Wh/kg Pd: 171.098 W/kg η: 0.930
1	Csp: 31.0845 F/g Ed: 1.5542 Wh/kg Pd: 327.267 W/kg η: 0.85	Csp: 15.091 F/g Ed: 0.75455 Wh/kg Pd: 327.274 W/kg η: 0.5646	Csp: 15.636 F/g Ed: 0.7818 Wh/kg Pd: 327.646 W/kg η: 0.914
2	Csp: 29.46 F/g Ed: 1.473 Wh/kg Pd: 653.66 W/kg η: 0.818	Csp: 14.182 F/g Ed: 0.7091 Wh/kg Pd: 654.537 W/kg η: 0.8478	Csp: 7.2727 F/g Ed: 0.3636 Wh/kg Pd: 654.48 W/kg η: 0.769
4	Csp: 24.7035 F/g Ed: 1.235 Wh/kg Pd: 1308.91 W/kg η: 0.828	Csp: 7.272 F/g Ed: 0.3636 Wh/kg Pd: 1309.01 W/kg η: 0.99	Csp: 3.636 F/g Ed: 0.1818 Wh/kg Pd: 1308.96 W/kg η: 0.714

Table 6 shows the specific capacitance, energy-power density and Coulombic efficiency values calculated from the three-electrode system analyses of the powders from GCD analyses for ZnO NPs, B400 and ZnO/B400 powders. When the 0.5 A/g current density values were compared, the highest power density value was found in the ZnO/B400 powder, while the highest energy density value was found in the ZnO powder. Energy density is the ability to store energy by volume, while power density is the power to discharge energy, not by volume. While energy density is high in batteries, power density is calculated higher in supercapacitors. In *Figure 45*, higher power density and energy density were obtained in the two-electrode system in the experiments as asymmetric and symmetric devices. Furthermore, Coulombic efficiency, also known as Faradaic or current efficiency, refers to the charge efficiency with which electrons are transmitted in batteries (Kamal K. Kar, 2023). When *Table 6* is examined, it is seen that the efficiency of ZnO/B400 powder at 0.5 A/g according to the current density values is higher than ZnO and B400 alone.

4.3.3. Characterizations of Inks

Ink characterizations are shown in *Figure 46*. FTIR analysis of inks prepared with 0.16 g of different B400 and ZnO NPs ratios is shown in *Figure 46(a)*. Since ink b contains the highest ZnO and B400 powders compared to the others, the peak in the 1088 cm^{-1} and 1630 cm^{-1} band gap where C-O and C=C bonds are observed was the highest, respectively. In *Figure 46(b)*, FTIR graphs of inks with different CMC concentration ratios are compared. The highest water content is found in ink d (0.16 g CMC) and the highest CMC content is found in ink f (0.24 g CMC). For this reason, O-H bonds are mostly seen in ink d, while C-O bonds are observed in ink f. FTIR analysis of different CMC concentrations are shown in *Figure 46(c)*. As in other inks, as the CMC ratio increases, the peaks in C-O and C=C chemical bonds become sharper, while as the CMC ratio decreases, the O-H bonds become more pronounced as the pure water ratio increases. Also, FTIR analysis of PVA/KOH electrolyte was shown in *Figure 46(d).* Since 6 M KOH concentration was used in the analysis of powders, the same molar ratio was also used for the micro-

supercapacitor electrolyte. In *Figure 46(e)*, viscosity and rheology analyses of the inks are added. According to the obtained data and observations, increasing the CMC concentration increased the viscosity.

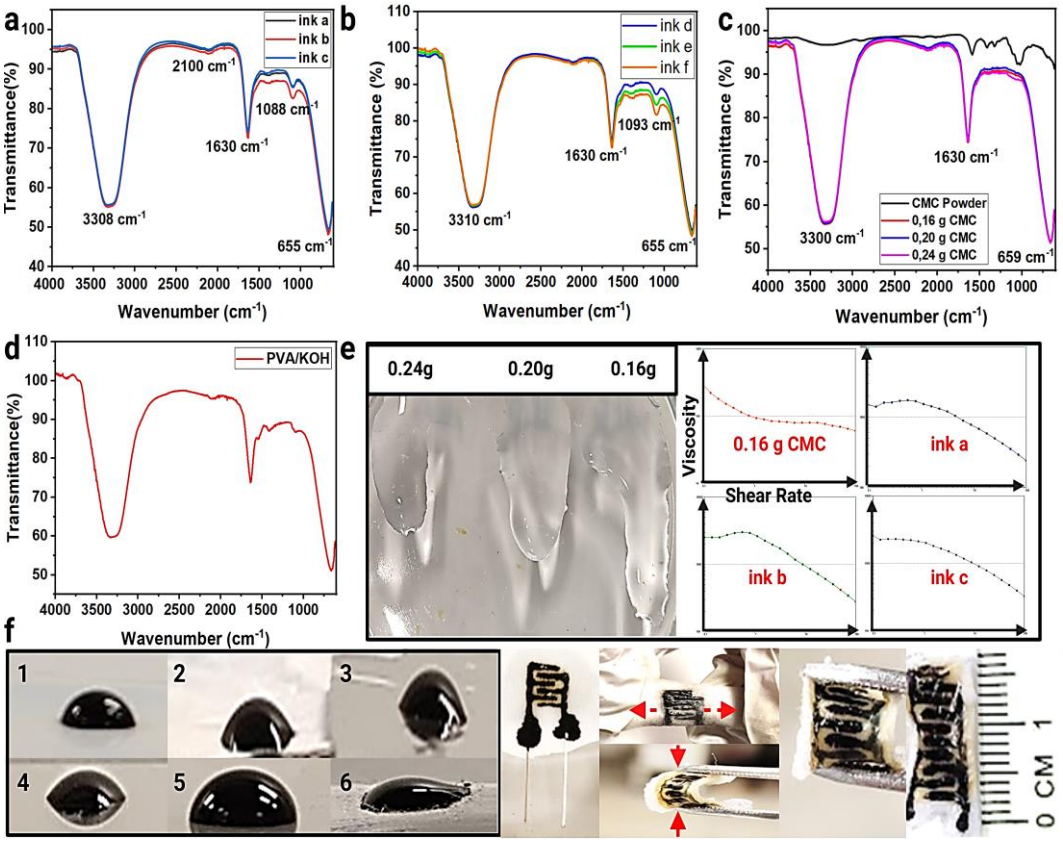


Figure 46: Concentration adjustment and characterization of the inks used in 3D printing: **a** FTIR analysis of three different inks prepared with 0.16 g of B400 and ZnO NPs powders in CMC solution at 4000-600 cm^{-1}, **b** FTIR analysis of inks prepared by adding the same amount of B400 and ZnO NPs powders in 0.16, 0.20 and 0.24 g of CMC solutions, **c** FTIR analysis of CMC concentration difference, **d** FTIR analysis of PVA/KOH electrolyte, **e** viscosity and rheological analysis of B400 and ZnO NPs powders, and **f** hydrophobic/hydrophilic properties of inks dropped onto different substrates and flexibility and dimensional analysis of printed micro-supercapacitors [BioRender].

In addition, when inks a, b, and c were compared, it was determined that the addition of ZnO NPs decreased the viscosity and the addition of B400 powder increased the viscosity. Firstly, the viscosity of the CMC solution prepared with 0.16 g as a reference was measured as 69.797 mPa.s. Then, the viscosity values of the inks to which ZnO NPs and B400 powders were added were determined. While 0.2 g of ZnO powder was found in ink a, 1.75 g of B400 powder was added and the viscosity value was found to be 354.26 mPa.s. Then, more B400 powder was added

to ink b and it was determined that the viscosity increased by 419.71 mPa.s. Then, the ZnO NPs powder ratio was reduced in ink c and the viscosity was measured as 477.69 mPa.s. From the results, it was determined that the viscosity decreased as ZnO NPs were added, but the viscosity increased as the B400 ratio increased. It has also been observed that increasing the amount of carbon in the ink increases the hydrophilicity. It has been observed that the ink with a high amount of zinc oxide and a low amount of carbon content is more hydrophobic.

Figure 46(f) includes images of ink d poured onto different substrates. Photographs 1, 2, 3, 4, 5, and 6 were taken from PET, electrospun aluminum foil, normal aluminum foil, glass, plastic, and 100% cotton fabrics, respectively. According to the hydrophobic and hydrophilic relationship, the ink could not adhere sufficiently on surfaces such as PDMS, PET, plastic, and foil because the contact angle was too high. However, printing was carried out with ink that adhered quite well to the fabric surface. The flexible test was performed by pulling the piece of fabric and applying force from above with the help of tweezers. The longest printed micro-supercapacitors of approximately 1.5 cm have shrunk to 0.5 cm. Ink d, which has the potential to be printed on very flexible and wearable fabric, will be examined in more detail in future studies.

4.3.4. Characterizations of Flexible Micro-Supercapacitor Devices

Measurements were performed in the two-electrode system for a three-pronged, flexible, symmetric, quasi-solid state, PDMS coated micro-supercapacitor device printed on 100% cotton fabric with a 0.84 mm nozzle needle tip with ink d which consisting of 0.4 g ZnO NPs powder, 3.5 g B400 powder and 20 ml 0.16 g CMC solution. The performance of micro-supercapacitors printed without a current collector was desired to be observed. For this purpose, metallic rods were placed at the ends of micro-supercapacitors and the positive and negative ends were connected to the cable. According to the analysis results, it was seen that it had high resistance because there was no current collector. However, the EIS analysis shown in *Figure 47(b)* was taken from the micro-supercapacitor device. It was thought that ion transfer could not be provided to the positive and negative parts during CV and

GCD analyses, and devices printed on platinum rods were placed by immersing them in 6M KOH electrolyte and CV and GCD analysis results were obtained in this way. The Rs value was found to be 0.513 ohm.

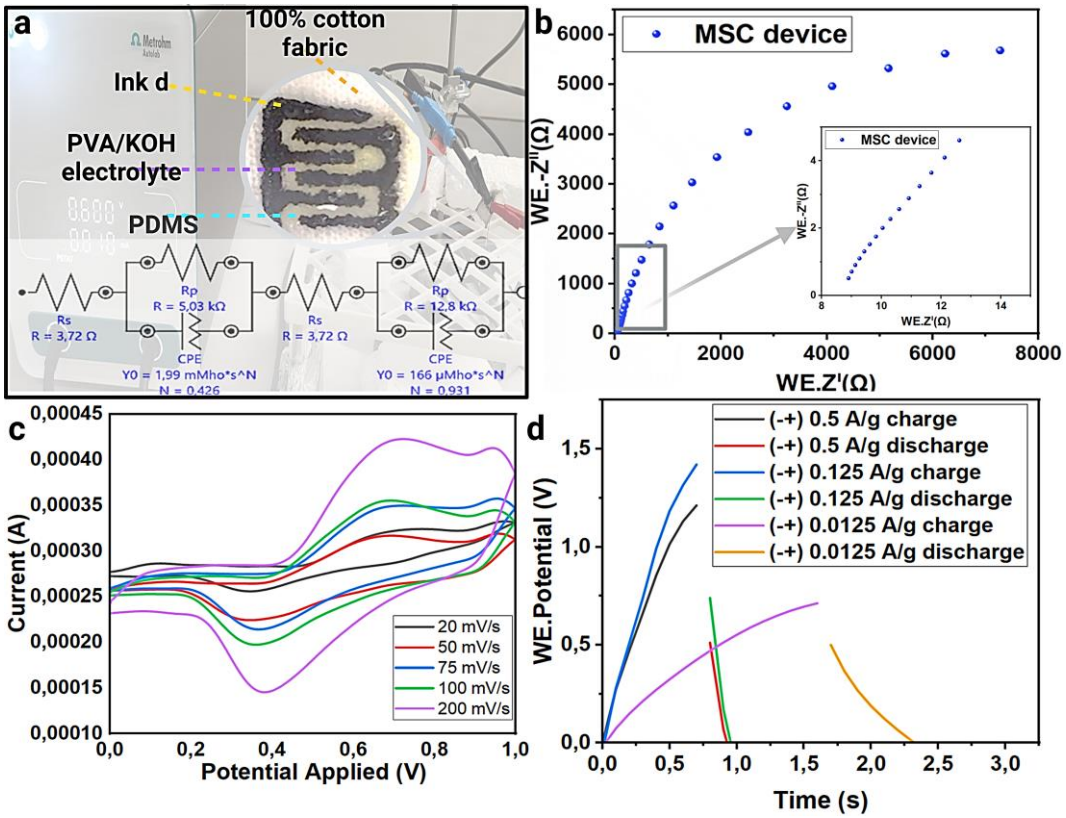


Figure 47: Electrochemical measurement trials of the MSC device: **a** taking the measurement of the printed MSC device in the two-electrode system, **b** EIS analysis result for the MSC device and circuit drawing with fitting of the result, **c** CV analysis between 0-1 V at different scan rates, and **d** GCD analysis between 0-0.6 V at different current density values [BioRender].

The high resistance value was explained by the absence of a current collector. It is also shown in *Figure 47(d)* that it charges and discharges very quickly. However, when printed with a current collector, it is thought that it can give better results than powders because the active material ratio is increased by printing three times on a small surface area.

Discussion

In this study, ZnO nanoparticles were produced from BE by the green synthesis method. Unlike Chapter 2, the calcination process was carried out at the same temperature but in a shorter time in order to increase porosity and reduce grain size.

Since 0.1 M zinc acetate dihydrate powder was synthesized as more porous, smaller grain size, and homogeneous in Chapter 2, ZnO nanoparticles were produced with the same concentration and raw material. In addition, in order to benefit more from broccoli, extract was obtained at lower temperatures, and the powders were not centrifuged. We subsequently carried out the characterizations of the ZnO nanoparticles synthesized for the study. Then, dried broccoli powder was converted into carbon source by burning at different calcination temperatures. Calcination was carried out starting from 300° C to 500° C, and the most optimum calcination temperature and powder were selected according to the analysis results. After the metal oxide and carbon source analyses, electrochemical properties were also tested. The promising results of slurry performance prepared with B400 powder instead of conductive carbon black were shown in the study. Again, symmetric and asymmetric device results of the synthesized powders were discussed. After the electrochemical characterizations of the powders, ink preparation optimizations for the 3D printer were performed. In order to prevent the use of toxic chemicals in the literature in electrochemical studies, CMC polymer and water were selected as solvents in this study. Different CMC, ZnO NPs, and B400 powder concentrations were tried to select the appropriate viscosity. It was observed that the viscosity increased with the addition of B400 powder and decreased with the addition of ZnO NPs. Then, flexible, quasi-solid-state, symmetric, wearable micro-supercapacitor printing was performed with an extrusion-based 3D printer. PVA/KOH gel electrolyte was dropped between micro-supercapacitors printed on 100% cotton fabric with a 0.84 mm inner diameter needle nozzle, 0.1 mPa pressure, and 1.5 cm size. After the heat treatment of the solid-state electrolyte, it was dropped onto PDMS for encapsulation. The aim of the study was to produce wearable devices by offering sustainability, recycling, harmlessness to human and environmental health, economical, and environmentally friendly solutions.

Nevertheless, it has been noted that this study does have drawbacks. First and foremost, B400 powder was chosen as the carbon source after conducting BET analysis. Because it was believed that the high surface area would allow for ion transfer and that porosity would facilitate current transmission between the electrode and electrolyte. However, the characterization assessments of B300 and B375 powders still needed to be compared. The findings of the SEM and EDS

investigation of B375 powder revealed greater carbon and oxygen ratios. In addition, electrochemical analyses of asymmetric devices were performed using B300 and B375 powders as the MSC was being manufactured. *Figure 45* depicts the greatest specific capacitance calculated in B375 powder, which was 58.05 F/g. Furthermore, B300 powder had the highest power density of 610.1 kW/kg and the highest energy density of 8.1 Wh/kg. However, the longest discharge time was observed in B400 powder. Although the potential of B400 powder was investigated in this thesis, it was proposed that carbon sources obtained from various plant extracts and calcination temperatures be studied and the performance improved. Additionally, in GCD analysis, charge and discharge could not start consecutively in the graphs due to iR drop on the y-axis. Another difficulty occurred while printing with a 3D printer. First and foremost, because electrode printing was performed on the current collector in the literature research, CV and GCD analyses were successfully measured. However, because no silver, aluminum, or copper inks were employed in this investigation, and it was not printed on a conductive substrate, micro-supercapacitors had difficulty measuring CV and GCD analyses. To avoid this, it was planned to use conductive polymers as binders or to create a conductive ink for the current collector. Even if a conductive wire was connected to the micro-supercapacitors, the CV and GCD analysis results could not be obtained due to the lack of a current collector. Furthermore, it was considered that the measurement could not be performed because the KOH ratio in the electrolyte between the electrodes was insufficient, preventing adequate ion transfer between the electrode and the electrolyte. *Figure 47* depicts the CV and GCD analyses of micro-supercapacitors printed on two distinct textiles as positive and negative electrodes and immersed in a 6 M KOH electrolyte. Despite being used as a conductive substrate, aluminum foil's hydrophobicity prevented ink from adhering to the surface. Although it was tested on plastic, glass, and PET substrates, 100% cotton fabric was chosen as a substrate because it attaches better to fabric, has greater flexibility, and is a wearable device. This section aims to demonstrate the possibilities of powders created by green synthesis and biowaste recycling. The goal is to demonstrate that supercapacitor applications could be created with 3D printers and manufactured as wearable devices using biodegradable polymers and non-toxic solvents.

A review of the literature revealed no studies in which green synthesis powder was manufactured using an extrusion-based 3D printer. Because the potential of electrodes produced from hybrid composites of metal oxides and carbon materials is higher, hybrid electrodes were also investigated in this study (Yan et al., 2022). In the literature, ZnO nanoparticles are typically doped with high conductivity metals like silver (Raza et al., 2024) and cobalt (Shaheen et al., 2020). As a result, their specific capacitance and energy density values were higher than previous research (Raza et al., 2024, Shaheen et al., 2020). In particular, powders containing compounds such as active carbon or reduced carbon were doped with ZnO nanoparticles during the manufacturing procedure (Haldorai et al., 2014). However, no studies have been found in the literature that investigate supercapacitors using ZnO nanoparticles produced with BE and 3D printer-printed carbon sources derived from biowaste.

In conclusion, this study investigated the production of wearable, flexible, quasi-solid state, symmetric, human and environmentally friendly, biocompatible micro-supercapacitors using ZnO nanoparticles and biowaste broccoli carbon powders as hybrid composite electrodes using green synthesis and 3D printing methods. It is anticipated that research on biodegradable, small-area, and high-performance supercapacitors will become more prevalent in the future, with recycling from biowastes potentially offering advantages in these studies.

4.4.Conclusions and Future Works

In the past few decades, advances in microelectronics have prompted greater research in this field. MSCs, with their microstructure, low weight, fast charge/discharge rate, and great flexibility, answer the growing demand for highly integrated and flexible electronics. Micro-supercapacitors are being used in a variety of applications, including energy storage systems, sensor integration, medical assistant examination, and alternating current (AC) line filtering. In

addition to the study fields stated, more research is needed to popularize both simple and inexpensive manufacturing techniques such as additive manufacturing and more expensive production techniques such as lithography, particularly in the field of micro-supercapacitors. There is a demand for electrode studies that demonstrate superior qualities in metrics such as capacitance, energy and power density, and columbic efficiency. Although the use of nanoparticles manufactured by chemical and physical processes in supercapacitor applications is popular, this work developed alternative methods eliminating excessively harmful substances. In this study, which is motivated by the notions of renewability and sustainability, green synthesis, carbon production from biowaste, and the usage of 3D printer technology were chosen to support this goal.

In this study, ZnO NPs produced from BE utilizing the green synthesis method were favored due to their high surface area of 10-20 nm. In addition, dried broccoli powder as biowaste was calcined at various temperatures and used as a carbon source. Electrochemical analyses of ZnO NPs and B400 powder, which was chosen as the most suited powder after characterization, were first conducted in a three-electrode setup. The poor capacitance value of B400 powder was enhanced by adding ZnO NPs, and it was discovered that it may be used to replace conductive carbon black. In addition, two-electrode electrochemical analyses of symmetric and asymmetric devices were carried out using ZnO NPs and B400 powder. Later, contrary in the literature, CMC, an alternative to the harmful compounds PVDF and NMP, and pure water as a solvent were preferred to make an ink binder solution. Concentration studies with CMC, B400, and ZnO NP powders were conducted, and the best ink for 3D printing and micro-supercapacitors were manufactured. It was found that increasing the ZnO nanoparticles powder reduced viscosity, while increasing the B400 powder increased viscosity based on the ink characterization. Electrode printing of 1.5 cm three-layer micro-supercapacitors was done at 0.1 mPa air pressure using 0.84 mm and 1.37 mm needle nozzle tips in various designs. PVA/KOH gel electrolyte was dropped between the electrodes, dried at 60^{o} C, then heat treated to form a gel at 60^{o} C. The micro-supercapacitor was successfully printed on 100% cotton fabric after the polymer cured with heat treatment and encapsulated with PDMS.

This study, motivated by goals such as carbon conversion from biowaste, sustainable and environmentally friendly production methods, and the replacement of toxic chemicals with alternative environmentally friendly materials in the field of electrochemistry, has developed alternative electrode materials. These materials have been printed with a 3D printer for the first time without using a current collector. For the future work, a conductive biocompatible polymer could be used on a more conductive substrate to increase hydrophilicity. In addition, 100% recycling of waste was achieved by using broccoli juice and all waste broccoli, and it was transformed into a product to be used in energy applications. The importance of micro-supercapacitors, which are smaller in size, have different designs, can store more active material, and use sustainable and cost-effective production techniques, could increase future use and become more prevalent in areas such as medicine, the defense industry, and the service sectors.

5. CHAPTER 5: CONCLUSIONS

5.1.Conclusions of Thesis

Because of the world's growing population, sustainability, waste recycling, energy conservation, and the development of alternatives to harmful chemicals and costly manufacturing techniques have become increasingly important in recent years. In this study, sustainable and environmentally friendly green synthesis and additive manufacturing technologies were developed for critical biological, thermal and energy applications.

First of all, nanotechnology has made its name known more due to its advantages, and its contribution to the development of smart, innovative materials has been a major factor in the production of the main materials in this study. Although nanomaterials have been synthesized with many conventional production techniques, green synthesis of nanoparticles have been carried out because of its low toxicity, cost, energy, and time savings. In Chapter 2, thorough study and characterization of nanoparticles are explained, and in subsequent chapters, how these synthesized nanoparticles are used and chosen for biological, thermal and energy applications are discussed in depth. BE, a biological plant waste, was used to produce gold, silver, zinc oxide, titanium dioxide, and iron oxide nanoparticles. BE, a stabilizing and reducing agent that reduces the metal source via the bioreduction method, was chosen as one of the primary method of this thesis study owing to its low cost, ease of use, high yield when dried, and lack of research in the literature. Each nanoparticle was analyzed and interpreted using XRD, UV-visible,

FTIR, SEM, and EDS, as well as TEM, VSM, cytotoxicity, and hyperthermia. Furthermore, concentration and raw material differences were investigated in gold and zinc oxide nanoparticle experiments. It was discovered that the most successful powders could be synthesized as particles using the optimal 0.4 mM $HAuCl_4.3H_2O$ gold source and 0.1 M zinc acetate dihydrate source. After detailed characterization, AuNPs synthesized at 0.4 mM were selected for use in photothermal therapy for Chapter 3 according to hyperthermia, cytotoxicity and UV-visibility analyses.

The second study sought to create novel material for photothermal therapy, which is a popular treatment strategy for cancer. To improve the hyperthermia effect, AuNPs were conjugated with PDA and RB after being produced using BE. To create pNIPAM hydrogel from NIPAM monomer with thermal sensitivity, the LIHAM material was prepared, and photocuring agents and additives such as AuNPs, AuNPs@PDA, AuNPs@RB, and AuNPs@PDA@RB were added to add optical sensitivity to the thermal sensitivity. The developed nanoparticles are printed using with another sustainable method of additive manufacturing or 3D printing. Here, hydrogel printing was done in kirigami pattern utilizing μSLA 3D printer, a combination of SLA and DLP techniques based on microstereolithography studies. For LIHAM hydrogel, optimum parameters were determined by applying photopolymerization to the solution at various light intensities and durations, and the influence of additions was investigated. Five different hydrogels were successfully printed, and their physicochemical, morphological, thermal and biological analyses were performed. According to the results obtained, the rheological and thermal analyzes of LIHAM@AuNPs@PDA@RB hydrogel gave the best results. It was shown that the hydrogel could be developed especially for use in hyperthermia analysis.

As the third investigation, a flexible, symmetric, quasi-solid-state, wearable micro-supercapacitor design was created by synthesizing ZnO NPs with BE and extracting carbon from broccoli powder as biowaste. When the materials utilized in the supercapacitor world were analyzed, it was discovered that pseudocapacitive and electric double-layer electrodes made by physical and chemical processes were created with hazardous binders and solvents such as PVDF and NMP. However, because sustainable, cost-effective, and ecologically friendly materials are required nowadays, CMC was used as the binder and pure water as the solvent in this thesis

study. The goal of this study, which used sustainable methodologies such as green synthesis and 3D printing technologies as manufacturing methods, was to investigate the potential use of synthesized powders for electrochemical applications. For this purpose, firstly the characterizations of ZnO NPs and calcined broccoli powders were examined in detail. The appropriate calcination temperature was selected using BET, SEM, EDS and TG/DTA analyses. According to the results, it was determined that broccoli powder calcined at 400º C (B400) showed high performance. Then, the electrochemical performance of ZnO NPs and B400 powders in the three-electrode system was investigated. In addition, B400 powder was added to the slurry prepared to be coated on nickel foams for the three-electrode analysis. The specific capacitances, energy-power densities, coulombic efficiency, and capacitive efficiency values of the powders for which EIS, CV, and GCD analyses were performed. It was found that ZnO/B400 powder with higher power density and coulombic efficiency values at 0.5 A/g current density gave better results when used as a hybrid of pseudocapacitive and EDLC two materials. According to the stability test performed for ZnO/B400 powder at 0.5 V at 1 A/g current density for up to 500 cycles, a stability of 64% was calculated. Symmetric and asymmetric device tests of the powders were also carried out in the two-electrode system. In the asymmetric devices, not only B400 powder but also B375 and B300 powders were used, and their electrochemical characterizations were compared. According to the capacitive efficiency analysis, B400 was the most stable powder, but the powder calcined at 375° C had a higher capacitance value due to its higher carbon and oxygen element concentration. Following the two- and three-electrode examinations of the powders, ink was produced for printing on an extrusion-based 3D printer. Instead of employing harmful compounds like PVDF and NMP to make ink, CMC was chosen. It was discovered that the solution made with 0.16 g of CMC powder gave appropriate viscosity for printing. After determining the binder concentration, rheology analysis was performed to determine the concentrations of B400 and ZnO NPs powders. According to the analysis, it was determined that the viscosity increased as the B400 powder ratio increased, and the viscosity decreased as the ZnO NPs ratio increased. The ink prepared with 0.4 g ZnO NPs, 3.5 g B400 and 20 ml CMC solution produced as ink was suitable for printing. Micro-supercapacitor printings were carried out in different designs on 100% cotton fabric, at 0.1 mPa air pressure, with 0.84 mm and

1.37 mm needle nozzle needle tip. After drying the electrodes at 60º C, PVA/KOH electrolyte was dropped between the electrodes. In order to obtain the gel electrolyte, heat treatment was applied at the same temperature for 10 minutes and micro-supercapacitors were encapsulated with PDMS. During printing, no current collector was used, only the printing was done. The developed wearable, flexible, 1.5 cm micro-supercapacitors were measured using EIS analysis. Due to high resistance and insufficient electrolyte, platinum rod and CV and GCD analyzes were measured by immersing it in the electrolyte.

Three main components of the thesis study were completed satisfactorily, and further research directions were identified. First and foremost, it was proposed that in order to achieve better outcomes in the sizes and morphological structures of the generated nanoparticles, BE optimization could be investigated, and nucleation could be regulated during nanoparticle production. In the second section, it was established that smaller quantities of additional AuNPs could be better distributed in LIHAM solution and that synthesis under 10 nm was necessary for usage in in vivo photothermal therapy trials. Although AuNPs@PDA@RB powders were injected to the hydrogel with a syringe during the hyperthermia analysis, the particle sizes were to be dispersed smaller in an ultrasonic sonicater for uniform distribution. The electrochemical analysis measurements of micro-supercapacitors were deemed to be more accurate when printed on fabric employing biocompatible conductive polymers or current collectors as binders while creating the ink. By identifying the advantages and disadvantages, it was possible to plan for future investigations, and it was believed that implementing the ideas would result in a more successful outcome.

In summary, 3D printing and green synthesis production processes are considered promising and are expected to play a significant role in future research. As the demand for sustainable, low-cost, simple, and environmentally friendly production methods increases, research in these areas will expand. Because these procedures are still developing and there is a lack of in-depth investigation and many unknowns, studies have the potential to achieve novelty and uniqueness. The work presented in this thesis has the potential to open up numerous applications for the green synthesis of nanoparticles and their processing through additive manufacturing.

6. REFERENCES

A. Venugopal. Immunotherapy vs Traditional Cancer Treatments: Pros and Cons: Traditional Cancer Treatments. https://www.pihealthcancerhospital.com/blog/immunotherapy-vs-traditional-cancer-treatments-pros-and-cons/ (accessed October 10, 2024).

Abdisattar, A.; Yeleuov, M.; Daulbayev, C.; Askaruly, K.; Tolynbekov, A.; Taurbekov, A.; Prikhodko, N. Recent advances and challenges of current collectors for supercapacitors. *Electrochemistry Communications* **2022,** *142*, 107373. DOI: 10.1016/j.elecom.2022.107373.

Abdulazeem, L.; Alasmari, A. F.; Alharbi, M.; Alshammari, A.; Muhseen, Z. T. Utilization of aqueous broccoli florets extract for green synthesis and characterization of silver nanoparticles, with potential biological applications. *Heliyon* **2023,** *9* (9), e19723. DOI: 10.1016/j.heliyon.2023.e19723.

Ahire, S. A.; Bachhav, A. A.; Pawar, T. B.; Jagdale, B. S.; Patil, A. V.; Koli, P. B. The Augmentation of nanotechnology era: A concise review on fundamental concepts of nanotechnology and applications in material science and technology. *Results in Chemistry* **2022,** *4*, 100633. DOI: 10.1016/j.rechem.2022.100633.

Ajayi, R. F.; Tshoko, S.; Franke, C.; Ngema, N.; Thipe, V.; Mulaudzi, T. Malus domestica and Solanum lycopersicum Mixtures for the Synthesis of Graphene Silver and Zinc Oxide Nanocomposites. *JSEMAT* **2022,** *12* (04), 61–81. DOI: 10.4236/jsemat.2022.124005.

Alagumira Meyyapan. One step synthesis of iron oxide nanoparticles via chemical and green route–an effective comparison [Online] **2014,** *7*, 70–74. https://journals.innovareacademics.in/index.php/ijpps/article/view/3995/6781.

Ali, A.; Zafar, H.; Zia, M.; Ul Haq, I.; Phull, A. R.; Ali, J. S.; Hussain, A. Synthesis, characterization, applications, and challenges of iron oxide nanoparticles. *Nanotechnology, science and applications* **2016,** *9*, 49–67. DOI: 10.2147/NSA.S99986.

Ali, I.; Peng, C.; Lin, D.; Saroj, D. P.; Naz, I.; Khan, Z. M.; Sultan, M.; Ali, M. Encapsulated green magnetic nanoparticles for the removal of toxic Pb2+ and Cd2+ from water: Development, characterization and application. *Journal of environmental management* **2019,** *234*, 273–289. DOI: 10.1016/j.jenvman.2018.12.112.

Amendola, V.; Meneghetti, M. Size Evaluation of Gold Nanoparticles by UV−vis Spectroscopy. *J. Phys. Chem. C* **2009,** *113* (11), 4277–4285. DOI: 10.1021/jp8082425.

Anbumani, D.; Dhandapani, K. v.; Manoharan, J.; Babujanarthanam, R.; Bashir, A.; Muthusamy, K.; Alfarhan, A.; Kanimozhi, K. Green synthesis and antimicrobial efficacy of titanium dioxide nanoparticles using Luffa acutangula leaf extract. *Journal of King Saud University - Science* **2022,** *34* (3), 101896. DOI: 10.1016/j.jksus.2022.101896.

ATEŞ, M.; YILMAZ, E.; KAR, B.; KARS DURUKAN, İ. Synthesis and Characterization of Silver Nanoparticles and Coating with Chitosan. *Politeknik Dergisi* **2021,** *24* (4), 1401–1408. DOI: 10.2339/politeknik.632079.

Avcıoğlu, S.; Ateş, Z. N.; Kam, E.; Kaya, C.; Kaya, F. The influence of polyelectrolyte on the synthesis of B4C/BN nanocomposite powders via sol-gel

method. *Ceramics International* **2022,** *48* (11), 15355–15363. DOI: 10.1016/j.ceramint.2022.02.069.

Avcıoğlu, S.; Buldu-Akturk, M.; Erdem, E.; Kaya, F.; Kaya, C. Boron Carbide as an Electrode Material: Tailoring Particle Morphology to Control Capacitive Behaviour. *Materials (Basel, Switzerland)* **2023,** *16* (2). DOI: 10.3390/ma16020861.

Avcioglu, S.; Kaya, F.; Kaya, C. Effect of elemental nano boron on the transformation and morphology of boron carbide (B4C) powders synthesized from polymeric precursors. *Ceramics International* **2020,** *46* (11), 17938–17950. DOI: 10.1016/j.ceramint.2020.04.104.

Bagheri, A.; Jin, J. Photopolymerization in 3D Printing. *ACS Appl. Polym. Mater.* **2019,** *1* (4), 593–611. DOI: 10.1021/acsapm.8b00165.

Baig, N.; Kammakakam, I.; Falath, W. Nanomaterials: a review of synthesis methods, properties, recent progress, and challenges. *Mater. Adv.* **2021,** *2* (6), 1821–1871. DOI: 10.1039/D0MA00807A.

Bhushan, B. *Springer handbook of nanotechnology*, 3rd ed., 2006.

Bilici, Ç.; Tatar, A. G.; Şentürk, E.; Dikyol, C.; Koç, B. Bisulfite-initiated crosslinking of gelatin methacryloyl hydrogels for embedded 3D bioprinting. *Biofabrication* **2022,** *14* (2). DOI: 10.1088/1758-5090/ac4dd9.

Charitidis, C. A.; Georgiou, P.; Koklioti, M. A.; Trompeta, A.-F.; Markakis, V. Manufacturing nanomaterials: from research to industry. *Manufacturing Rev.* **2014,** *1*, 11. DOI: 10.1051/mfreview/2014009.

Chen, L.; Duan, G.; Zhang, C.; Cheng, P.; Wang, Z. 3D printed hydrogel for soft thermo-responsive smart window. *Int. J. Extrem. Manuf.* **2022,** *4* (2), 25302. DOI: 10.1088/2631-7990/ac5ae3.

Cooperstein, M. A.; Canavan, H. E. Assessment of cytotoxicity of (N-isopropyl acrylamide) and poly(N-isopropyl acrylamide)-coated surfaces. *Biointerphases* **2013,** *8* (1), 19. DOI: 10.1186/1559-4106-8-19.

Cuadrado, C. F.; Lagos, K. J.; Stringasci, M. D.; Bagnato, V. S.; Romero, M. P. Clinical and pre-clinical advances in the PDT/PTT strategy for diagnosis and treatment of cancer. *Photodiagnosis and photodynamic therapy* **2024,** *50*, 104387. DOI: 10.1016/j.pdpdt.2024.104387.

Cytodiagnostics. Introduction to Gold Nanoparticle Characterization: Ultraviolet-Visible (UV-Vis) Spectroscopy. https://www.cytodiagnostics.com/pages/introduction-to-gold-nanoparticle-characterization (accessed October 5, 2024).

Dhanemozhi, A. C.; Rajeswari, V.; Sathyajothi, S. Green Synthesis of Zinc Oxide Nanoparticle Using Green Tea Leaf Extract for Supercapacitor Application. *Materials Today: Proceedings* **2017,** *4* (2), 660–667. DOI: 10.1016/j.matpr.2017.01.070.

Dhanraj, G.; Rajeshkumar, S. Anticariogenic Effect of Selenium Nanoparticles Synthesized Using Brassica oleracea. *Journal of Nanomaterials* **2021,** *2021*, 1–9. DOI: 10.1155/2021/8115585.

Ding, W.; Chechetka, S. A.; Masuda, M.; Shimizu, T.; Aoyagi, M.; Minamikawa, H.; Miyako, E. Lipid Nanotube Tailored Fabrication of Uniquely Shaped Polydopamine Nanofibers as Photothermal Converters. *Chemistry* **2016,** *22* (13), 4345–4350. DOI: 10.1002/chem.201504958.

Domínguez-Perles, R.; Martínez-Ballesta, M. C.; Carvajal, M.; García-Viguera, C.; Moreno, D. A. Broccoli-derived by-products--a promising source of bioactive ingredients. *Journal of food science* **2010,** *75* (4), C383-92. DOI: 10.1111/j.1750-3841.2010.01606.x.

Dychalska, A.; Popielarski, P.; Franków, W.; Fabisiak, K.; Paprocki, K.; Szybowicz, M. Study of CVD diamond layers with amorphous carbon admixture by Raman scattering spectroscopy. *Materials Science-Poland* **2015,** *33* (4), 799–805. DOI: 10.1515/msp-2015-0067.

Ersoy, S.; Yıldız, E.; Ren, Z.; Zhang, M.; Zhang, H.; Karaz, S.; Han, M.; Shiva, A.; Yunusa, M.; Kaya, C.; Koç, B.; Sitti, M. Fabrication of Gold Nanoflower-Coated Photosensitive Meta-Structures Using PμSL 3D Printing for Hyperthermia Applications. *ACS Appl. Polym. Mater.* **2024,** *6* (17), 10807–10823. DOI: 10.1021/acsapm.4c01951.

Estrada-Urbina, J.; Cruz-Alonso, A.; Santander-González, M.; Méndez-Albores, A.; Vázquez-Durán, A. Nanoscale Zinc Oxide Particles for Improving the Physiological and Sanitary Quality of a Mexican Landrace of Red Maize. *Nanomaterials (Basel, Switzerland)* **2018,** *8* (4). DOI: 10.3390/nano8040247.

Fang, J.; Chen, Y.-C. Nanomaterials for photohyperthermia: a review. *Current pharmaceutical design* **2013,** *19* (37), 6622–6634. DOI: 10.2174/1381612811319370006.

Galstyan, V.; Bhandari, M.; Sberveglieri, V.; Sberveglieri, G.; Comini, E. Metal Oxide Nanostructures in Food Applications: Quality Control and Packaging. *Chemosensors* **2018,** *6* (2), 16. DOI: 10.3390/chemosensors6020016.

Ganeshpurkar, A.; Saluja, A. K. The Pharmacological Potential of Rutin. *Saudi pharmaceutical journal : SPJ : the official publication of the Saudi Pharmaceutical Society* **2017,** *25* (2), 149–164. DOI: 10.1016/j.jsps.2016.04.025.

Gayathri Devi, K.; Clara Dhanemozhi, A.; Sathya Priya, L. Green synthesis of Zinc oxide nanoparticles using lemon extract for waste water treatment. *Materials Today: Proceedings* [Online] **2023**.

Ghodake, G. S.; Shinde, S. K.; Saratale, G. D.; Saratale, R. G.; Kim, M.; Jee, S.-C.; Kim, D.-Y.; Sung, J.-S.; Kadam, A. A. α-Cellulose Fibers of Paper-Waste Origin Surface-Modified with Fe3O4 and Thiolated-Chitosan for Efficacious Immobilization of Laccase. *Polymers* **2021,** *13* (4). DOI: 10.3390/polym13040581.

Golli, R.; Thummaneni, C.; Pabbathi, D. D.; Srungarapu, T.; Jayasri, G.; Vangalapati, M. Silver nanoparticles synthesized by Brassica oleracea (Broccoli) acting as antifungal agent against Candida albicans. *Materials Today: Proceedings* **2023,** *80*, 1495–1500. DOI: 10.1016/j.matpr.2023.01.284.

Graça, A.; Bom, S.; Martins, A. M.; Ribeiro, H. M.; Marto, J. Vat-based photopolymerization 3D printing: From materials to topical and transdermal applications. *Asian journal of pharmaceutical sciences* **2024,** *19* (4), 100940. DOI: 10.1016/j.ajps.2024.100940.

Green Synthesis of TiO 2 Nanoparticles Using Hibiscus Flower Extract; K. Ganapathi Rao, Ed., 2014.

Gurunathan, S.; Han, J.; Park, J. H.; Kim, J.-H. A green chemistry approach for synthesizing biocompatible gold nanoparticles. *Nanoscale research letters* **2014,** *9* (1), 248. DOI: 10.1186/1556-276X-9-248.

H. Levent Keskin. *What is nanotechnology?*, 2011 (3842790). https://dergipark.org.tr/tr/download/article-file/3842790 (accessed October 8, 2024).

Haldorai, Y.; Voit, W.; Shim, J.-J. Nano ZnO@reduced graphene oxide composite for high performance supercapacitor: Green synthesis in supercritical fluid. *Electrochimica Acta* **2014,** *120*, 65–72. DOI: 10.1016/j.electacta.2013.12.063.

Haq, M. A.; Su, Y.; Wang, D. Mechanical properties of PNIPAM based hydrogels: A review. *Materials science & engineering. C, Materials for biological applications* **2017,** *70* (Pt 1), 842–855. DOI: 10.1016/j.msec.2016.09.081.

Huang, Z.; Li, J.; Chen, X.; Yang, Q.; Zeng, X.; Bai, R.; Wang, L. Photothermal Sensitive 3D Printed Biodegradable Polyester Scaffolds with Polydopamine Coating for Bone Tissue Engineering. *Polymers* **2023,** *15* (2). DOI: 10.3390/polym15020381.

Idrees, M.; Ahmed, S.; Mohammed, Z.; Korivi, N. S.; Rangari, V. 3D printed supercapacitor using porous carbon derived from packaging waste. *Additive Manufacturing* **2020,** *36*, 101525. DOI: 10.1016/j.addma.2020.101525.

Iqbal, M. Z.; Zakar, S.; Haider, S. S. Role of aqueous electrolytes on the performance of electrochemical energy storage device. *Journal of Electroanalytical Chemistry* **2020,** *858*, 113793. DOI: 10.1016/j.jelechem.2019.113793.

Isik, Z.; Bouchareb, R.; Arslan, H.; Özdemir, S.; Gonca, S.; Dizge, N.; Balakrishnan, D.; Prasad, S. V. S. Green synthesis of iron oxide nanoparticles derived from water and methanol extract of Centaurea solstitialis leaves and tested for antimicrobial activity and dye decolorization capability. *Environmental research* **2023,** *219*, 115072. DOI: 10.1016/j.envres.2022.115072.

Jamkhande, P. G.; Ghule, N. W.; Bamer, A. H.; Kalaskar, M. G. Metal nanoparticles synthesis: An overview on methods of preparation, advantages and disadvantages, and applications. *Journal of Drug Delivery Science and Technology* **2019,** *53*, 101174. DOI: 10.1016/j.jddst.2019.101174.

Jeon, Y.; Ko, Y.; Lee, S.; Jeong, M.; Lee, K.; Kwon, G.; Kim, J.; You, J. PEDOT:PSS/regenerated cellulose composite microelectrode for high-performance micro-supercapacitor. *Applied Surface Science* **2023,** *636*, 157806. DOI: 10.1016/j.apsusc.2023.157806.

Jia, R.; Shen, G.; Qu, F.; Di Chen. Flexible on-chip micro-supercapacitors: Efficient power units for wearable electronics. *Energy Storage Materials* **2020,** *27*, 169–186. DOI: 10.1016/j.ensm.2020.01.030.

Jyoti, K.; Baunthiyal, M.; Singh, A. Characterization of silver nanoparticles synthesized using Urtica dioica Linn. leaves and their synergistic effects with antibiotics. *Journal of Radiation Research and Applied Sciences* **2016,** *9* (3), 217–227. DOI: 10.1016/j.jrras.2015.10.002.

Kalagatur, N. K.; Karthick, K.; Allen, J. A.; Nirmal Ghosh, O. S.; Chandranayaka, S.; Gupta, V. K.; Krishna, K.; Mudili, V. Application of Activated Carbon Derived from Seed Shells of Jatropha curcas for Decontamination of Zearalenone Mycotoxin. *Frontiers in pharmacology* **2017,** *8*, 760. DOI: 10.3389/fphar.2017.00760.

Kale, A. M.; Biradar, M. R.; Cho, W.-J.; Kaya, C.; Bhosale, S. V.; Bhosale, S. V.; Kim, B. C. Unveiling a cutting-edge bi-ligand nickel metal-organic framework as an electrode material for symmetric supercapacitors. *Journal of Energy Storage* **2023,** *73*, 109123. DOI: 10.1016/j.est.2023.109123.

Kamal K. Kar. *Handbook of Nanocomposite Supercapacitor Materials IV*. *Next generation supercapacitors* 331: Springer Nature Link, 2023.

Kanwal, Z.; Raza, M. A.; Riaz, S.; Manzoor, S.; Tayyeb, A.; Sajid, I.; Naseem, S. Synthesis and characterization of silver nanoparticle-decorated cobalt nanocomposites (Co@AgNPs) and their density-dependent antibacterial

activity. *Royal Society open science* **2019,** *6* (5), 182135. DOI: 10.1098/rsos.182135.

Khoobchandani, M.; Zambre, A.; Katti, K.; Lin, C.-H.; Katti, K. V. Green Nanotechnology from Brassicaceae. *International Journal of Green Nanotechnology* **2013,** *1. DOI:* 10.1177/1943089213509474.

Kırkbınar, M.; İbrahimoğlu, E.; Demir, A.; Çalışkan, F.; Altındal, Ş. Improvement of electric and photoelectric properties of the Al/n-ZnO/p-Si/Al photodiodes by green synthesis method using chamomille flower extract. *J Mater Sci: Mater Electron* **2023,** *34* (3). DOI: 10.1007/s10854-022-09515-9.

Kiwumulo, H. F.; Muwonge, H.; Ibingira, C.; Lubwama, M.; Kirabira, J. B.; Ssekitoleko, R. T. Green synthesis and characterization of iron-oxide nanoparticles using Moringa oleifera: a potential protocol for use in low and middle income countries. *BMC research notes* **2022,** *15* (1), 149. DOI: 10.1186/s13104-022-06039-7.

Korde, S. A.; Thombre, P. B.; Dipake, S. S.; Sangshetti, J. N.; Rajbhoj, A. S.; Gaikwad, S. T. Neem gum (Azadirachta indicia) facilitated green synthesis of TiO2 and ZrO2 nanoparticles as antimicrobial agents. *Inorganic Chemistry Communications* **2023,** *153*, 110777. DOI: 10.1016/j.inoche.2023.110777.

Kumar, V.; Kaushik, N. K.; Tiwari, S. K.; Singh, D.; Singh, B. Green synthesis of iron nanoparticles: Sources and multifarious biotechnological applications. *International journal of biological macromolecules* **2023,** *253* (Pt 4), 127017. DOI: 10.1016/j.ijbiomac.2023.127017.

Kurra, N.; Hota, M. K.; Alshareef, H. N. Conducting polymer micro-supercapacitors for flexible energy storage and Ac line-filtering. *Nano Energy* **2015,** *13*, 500–508. DOI: 10.1016/j.nanoen.2015.03.018.

L. Khezami. ZnO nanoparticles: Surface and X-ray profile analysis [Online] **2018,** *14*, 381–393. https://www.researchgate.net/publication/328026905 (accessed September 2018).

Lee, S. H.; Jun, B.-H. Silver Nanoparticles: Synthesis and Application for Nanomedicine. *International journal of molecular sciences* **2019,** *20* (4). DOI: 10.3390/ijms20040865.

Lee, Y.-W.; Kim, J.-K.; Bozuyuk, U.; Dogan, N. O.; Khan, M. T. A.; Shiva, A.; Wild, A.-M.; Sitti, M. Multifunctional 3D-Printed Pollen Grain-Inspired Hydrogel Microrobots for On-Demand Anchoring and Cargo Delivery. *Advanced materials (Deerfield Beach, Fla.)* **2023,** *35* (10), e2209812. DOI: 10.1002/adma.202209812.

Li, H.; He, E.; Wang, Y.; Fu, J.; Liu, T.; Gou, R.; Shi, S.; Gu, C. Albumin-stabilized polydopamine nanoparticles for chemo-photothermal synergistic therapy of melanoma. *Journal of Drug Delivery Science and Technology* **2023,** *87*, 104759. DOI: 10.1016/j.jddst.2023.104759.

Li, H.; Yin, D.; Li, W.; Tang, Q.; Zou, L.; Peng, Q. Polydopamine-based nanomaterials and their potentials in advanced drug delivery and therapy. *Colloids and surfaces. B, Biointerfaces* **2021a,** *199*, 111502. DOI: 10.1016/j.colsurfb.2020.111502.

Li, H.; Zhu, X.; Li, Z.; Yang, J.; Lan, H. Preparation of Nano Silver Paste and Applications in Transparent Electrodes via Electric-Field Driven Micro-Scale 3D Printing. *Nanomaterials (Basel, Switzerland)* **2020,** *10* (1). DOI: 10.3390/nano10010107.

Li, Y.; Wang, J.; Yang, Y.; Shi, J.; Zhang, H.; Yao, X.; Chen, W.; Zhang, X. A rose bengal/graphene oxide/PVA hybrid hydrogel with enhanced mechanical

properties and light-triggered antibacterial activity for wound treatment. *Materials science & engineering. C, Materials for biological applications* **2021b,** *118*, 111447. DOI: 10.1016/j.msec.2020.111447.

Liu, K.; Hu, N.; Yu, Z.; Zhang, X.; Ma, H.; Qu, H.; Ruan, C. 3D printing and bioprinting in urology. *IJB* **2023,** *9* (6), 969. DOI: 10.36922/ijb.0969.

Liu, W.; Lu, C.; Wang, X.; Tay, R. Y.; Tay, B. K. High-performance microsupercapacitors based on two-dimensional graphene/manganese dioxide/silver nanowire ternary hybrid film. *ACS nano* **2015,** *9* (2), 1528–1542. DOI: 10.1021/nn5060442.

Liu, Y.; Zheng, S.; Ma, J.; Zhu, Y.; Wang, J.; Feng, X.; Wu, Z.-S. Aqueous high-voltage all 3D-printed micro-supercapacitors with ultrahigh areal capacitance and energy density. *Journal of Energy Chemistry* **2021,** *63*, 514–520. DOI: 10.1016/j.jechem.2021.08.018.

Mahmood, T.; Baig, F. *A comparative study of ZnO, ZnO/GO and ZnO/RGO nanocomposites for the energy application*, 2024.

Mahmoud, N. N.; Aqabani, H.; Hikmat, S.; Abu-Dahab, R. Colloidal Stability and Cytotoxicity of Polydopamine-Conjugated Gold Nanorods against Prostate Cancer Cell Lines. *Molecules (Basel, Switzerland)* **2021,** *26* (5). DOI: 10.3390/molecules26051299.

Maria Guerra. What's the Difference Between Batteries & Supercapacitors? https://www.batterytechonline.com/components/what-s-the-difference-between-batteries-supercapacitors-.

Mehmet ATEŞ. *Nanoparçacıkların Ölçme ve İnceleme Teknikleri*, 2018 (608610). https://dergipark.org.tr/en/download/article-file/608610.

Michael F. Ashby, Paulo J. Ferreira and Daniel L. Schodek. *Nanomaterials, Nanotechnologies and Design;* Elsevier, 2009.

Minakshi, M.; Higley, S.; Baur, C.; Mitchell, D. R. G.; Jones, R. T.; Fichtner, M. Calcined chicken eggshell electrode for battery and supercapacitor applications. *RSC advances* **2019,** *9* (46), 26981–26995. DOI: 10.1039/C9RA04289J.

Moradi, S.; Najjar, R.; Hamishehkar, H.; Lotfi, A. Triple-responsive drug nanocarrier: Magnetic core-shell nanoparticles of Fe3O4@poly(N-isopropylacrylamide)-grafted-chitosan, synthesis and in vitro cytotoxicity evaluation against human lung and breast cancer cells. *Journal of Drug Delivery Science and Technology* **2022,** *72*, 103426. DOI: 10.1016/j.jddst.2022.103426.

Mousa, S. A.; Wissa, D. A.; Hassan, H. H.; Ebnalwaled, A. A.; Khairy, S. A. Enhanced photocatalytic activity of green synthesized zinc oxide nanoparticles using low-cost plant extracts. *Scientific reports* **2024,** *14* (1), 16713. DOI: 10.1038/s41598-024-66975-1.

MuthuKathija, M.; Sheik Muhideen Badhusha, M.; Rama, V. Green synthesis of zinc oxide nanoparticles using Pisonia Alba leaf extract and its antibacterial activity. *Applied Surface Science Advances* **2023,** *15*, 100400. DOI: 10.1016/j.apsadv.2023.100400.

N. Funda AK AZEM, Işıl BİRLİK. Sol-jel Yöntemi ile Hazırlanmış ZnO Nanopartiküllerin Optimizasyonu **2018,** *20* (58). DOI: 10.21205/deufmd.

Naiel, B.; Fawzy, M.; Halmy, M. W. A.; Mahmoud, A. E. D. Green synthesis of zinc oxide nanoparticles using Sea Lavender (Limonium pruinosum L. Chaz.) extract: characterization, evaluation of anti-skin cancer, antimicrobial and antioxidant potentials. *Scientific reports* **2022,** *12* (1), 20370. DOI: 10.1038/s41598-022-24805-2.

National Cancer Institute, Terese Winslow. Types of Cancer Treatment: Hyperthermia. https://www.cancer.gov/about-cancer/treatment/types/hyperthermia.

NicDaéid, N. Systematic Drug Identification ☆. *Reference Module in Chemistry, Molecular Sciences and Chemical Engineering*; Elsevier, 2018. DOI: 10.1016/B978-0-12-409547-2.14457-9.

Niraimathee, V. A.; Subha, V.; Ravindran, R. E.; Renganathan, S. Green synthesis of iron oxide nanoparticles from Mimosa pudica root extract. *IJESD* **2016,** *15* (3), 227. DOI: 10.1504/IJESD.2016.077370.

Osuntokun, J.; Onwudiwe, D. C.; Ebenso, E. E. Green synthesis of ZnO nanoparticles using aqueous Brassica oleracea L. var. italica and the photocatalytic activity. *Green Chemistry Letters and Reviews* **2019,** *12* (4), 444–457. DOI: 10.1080/17518253.2019.1687761.

Ovhal, M. M.; Kumar, N.; Kang, J.-W. 3D direct ink writing fabrication of high-performance all-solid-state micro-supercapacitors. *Molecular Crystals and Liquid Crystals* **2020,** *705* (1), 105–111. DOI: 10.1080/15421406.2020.1743426.

Park, S. H.; Goodall, G.; Kim, W. S. Perspective on 3D-designed micro-supercapacitors. *Materials & Design* **2020,** *193*, 108797. DOI: 10.1016/j.matdes.2020.108797.

Patil, D. J.; Behera, S. N. Synthesizing nanoparticles of zinc and copper ferrites and examining their potential to remove various organic dyes through comparative studies of kinetics, isotherms, and thermodynamics. *Environmental monitoring and assessment* **2023,** *195* (5), 591. DOI: 10.1007/s10661-023-11177-x.

Paunović, N.; Marbach, J.; Bao, Y.; Berger, V.; Klein, K.; Schleich, S.; Coulter, F. B.; Kleger, N.; Studart, A. R.; Franzen, D.; Luo, Z.; Leroux, J.-C. Digital Light 3D Printed Bioresorbable and NIR-Responsive Devices with Photothermal and Shape-Memory Functions. *Advanced science (Weinheim, Baden-Wurttemberg, Germany)* **2022,** *9* (27), e2200907. DOI: 10.1002/advs.202200907.

Pawar, O.; Deshpande, N.; Dagade, S.; Waghmode, S.; Nigam Joshi, P. Green synthesis of silver nanoparticles from purple acid phosphatase apoenzyme isolated from a new source Limonia acidissima. *Journal of Experimental Nanoscience* **2016,** *11* (1), 28–37. DOI: 10.1080/17458080.2015.1025300.

Peng, X.; Peng, L.; Wu, C.; Xie, Y. Two dimensional nanomaterials for flexible supercapacitors. *Chemical Society reviews* **2014,** *43* (10), 3303–3323. DOI: 10.1039/c3cs60407a.

Piruthiviraj, P.; Margret, A.; Krishnamurthy, P. P. Gold nanoparticles synthesized by Brassica oleracea (Broccoli) acting as antimicrobial agents against human pathogenic bacteria and fungi. *Appl Nanosci* **2016,** *6* (4), 467–473. DOI: 10.1007/s13204-015-0460-4.

Pu, J.; Wang, X.; Xu, R.; Xu, S.; Komvopoulos, K. Highly flexible, foldable, and rollable microsupercapacitors on an ultrathin polyimide substrate with high power density. *Microsystems & nanoengineering* **2018,** *4*, 16. DOI: 10.1038/s41378-018-0016-3.

Pugazhendhi, S. Synthesis of ipomoea staphylina plant extract mediated silver nanoparticles. *Materials Today: Proceedings* **2020,** *33*, 4626–4629. DOI: 10.1016/j.matpr.2020.08.287.

Putri, K. N. A.; Intasanta, V.; Hoven, V. P. Current significance and future perspective of 3D-printed bio-based polymers for applications in energy

conversion and storage system. *Heliyon* **2024,** *10* (4), e25873. DOI: 10.1016/j.heliyon.2024.e25873.

Qu, Y.; Lu, K.; Zheng, Y.; Huang, C.; Wang, G.; Zhang, Y.; Yu, Q. Photothermal scaffolds/surfaces for regulation of cell behaviors. *Bioactive materials* **2022,** *8*, 449–477. DOI: 10.1016/j.bioactmat.2021.05.052.

Ramani, A.; Taherabbas, S.; Saji, R.; Bumbadiya, M.; Gandhi, K.; Seth, R. Nanotechnology: An emerging trend in the dairy industry – Applications and future challenges. *Food and Humanity* **2024,** *3*, 100409. DOI: 10.1016/j.foohum.2024.100409.

Rapp, T. L.; DeForest, C. A. Visible Light-Responsive Dynamic Biomaterials: Going Deeper and Triggering More. *Advanced healthcare materials* **2020,** *9* (7), e1901553. DOI: 10.1002/adhm.201901553.

Raza, A.; Sayeed, K.; Naaz, A.; Muaz, M.; Islam, S. N.; Rahaman, S.; Sama, F.; Pandey, K.; Ahmad, A. Green Synthesis of ZnO Nanoparticles and Ag-Doped ZnO Nanocomposite Utilizing Sansevieria trifasciata for High-Performance Asymmetric Supercapacitors. *ACS omega* **2024,** *9* (30), 32444–32454. DOI: 10.1021/acsomega.3c10060.

Razack, S. A.; Suresh, A.; Sriram, S.; Ramakrishnan, G.; Sadanandham, S.; Veerasamy, M.; Nagalamadaka, R. B.; Sahadevan, R. Green synthesis of iron oxide nanoparticles using Hibiscus rosa-sinensis for fortifying wheat biscuits. *SN Appl. Sci.* **2020,** *2* (5). DOI: 10.1007/s42452-020-2477-x.

Reference Module in Chemistry, Molecular Sciences and Chemical Engineering; Elsevier, 2018.

Santhosh, P. B.; Genova, J.; Chamati, H. Green Synthesis of Gold Nanoparticles: An Eco-Friendly Approach. *Chemistry* **2022,** *4* (2), 345–369. DOI: 10.3390/chemistry4020026.

Santiago, M.; Rivera, D.; Torres, A. Green Synthesis of Titanium Oxide Nanoparticles Using Natural Extracts. *MSCE* **2023,** *11* (02), 29–40. DOI: 10.4236/msce.2023.112003.

Shaheen, I.; Ahmad, K. S.; Zequine, C.; Gupta, R. K.; Thomas, A. G.; Malik, M. A. Green synthesis of ZnO–Co 3 O 4 nanocomposite using facile foliar fuel and investigation of its electrochemical behaviour for supercapacitors. *New J. Chem.* **2020,** *44* (42), 18281–18292. DOI: 10.1039/D0NJ03430D.

Shanavas, S.; Priyadharsan, A.; Karthikeyan, S.; Dharmaboopathi, K.; Ragavan, I.; Vidya, C.; Acevedo, R.; Anbarasana, P. M. Green synthesis of titanium dioxide nanoparticles using Phyllanthus niruri leaf extract and study on its structural, optical and morphological properties. *Materials Today: Proceedings* **2020,** *26*, 3531–3534. DOI: 10.1016/j.matpr.2019.06.715.

Shen, K.; Ding, J.; Yang, S. 3D Printing Quasi-Solid-State Asymmetric Micro-Supercapacitors with Ultrahigh Areal Energy Density. *Advanced Energy Materials* **2018,** *8* (20). DOI: 10.1002/aenm.201800408.

Singh, P.; Kim, Y.-J.; Zhang, D.; Yang, D.-C. Biological Synthesis of Nanoparticles from Plants and Microorganisms. *Trends in biotechnology* **2016,** *34* (7), 588–599. DOI: 10.1016/j.tibtech.2016.02.006.

Singh, S.; Bharti, A.; Meena, V. K. Green synthesis of multi-shaped silver nanoparticles: optical, morphological and antibacterial properties. *J Mater Sci: Mater Electron* **2015,** *26* (6), 3638–3648. DOI: 10.1007/s10854-015-2881-y.

Soni, J.; Teli, P.; Agarwal, S. Recent Advances in the Green Reduction of Graphene Oxide and its Potential Applications. *CNANO* **2024,** *20* (2), 146–156. DOI: 10.2174/1573413719666230329104621.

Soon, R. H.; Ren, Z.; Hu, W.; Bozuyuk, U.; Yildiz, E.; Li, M.; Sitti, M. On-demand anchoring of wireless soft miniature robots on soft surfaces. *Proceedings of the National Academy of Sciences of the United States of America* **2022,** *119* (34), e2207767119. DOI: 10.1073/pnas.2207767119.

Sridhar, V.; Yildiz, E.; Rodríguez-Camargo, A.; Lyu, X.; Yao, L.; Wrede, P.; Aghakhani, A.; Akolpoglu, B. M.; Podjaski, F.; Lotsch, B. V.; Sitti, M. Designing Covalent Organic Framework-Based Light-Driven Microswimmers toward Therapeutic Applications. *Advanced materials (Deerfield Beach, Fla.)* **2023,** *35* (25), e2301126. DOI: 10.1002/adma.202301126.

Su, M.; Liu, Y.; Wan, H.; Dou, A.; Wang, Z.; Guo, H. High cycling performance Si/CNTs@C composite material prepared by spray–drying method. *Ionics* **2017,** *23* (2), 405–410. DOI: 10.1007/s11581-016-1867-y.

Sun, H.; Wang, Y.; Cheff, D. M.; Hall, M. D.; Shen, M. Predictive models for estimating cytotoxicity on the basis of chemical structures. *Bioorganic & medicinal chemistry* **2020,** *28* (10), 115422. DOI: 10.1016/j.bmc.2020.115422.

Sun, P.; Liu, J.; Liu, Q.; Yu, J.; Chen, R.; Zhu, J.; Sun, G.; Li, Y.; Liu, P.; Wang, J. An inkjet-printing ink based on porous NiS/N-MXene for high-performance asymmetric micro-supercapacitors and self-powered microelectronics. *Chemical Engineering Journal* **2023,** *474*, 145466. DOI: 10.1016/j.cej.2023.145466.

Suppiah, D. D.; Julkapli, N. M.; Sagadevan, S.; Johan, M. R. Eco-friendly green synthesis approach and evaluation of environmental and biological applications of iron oxide nanoparticles. *Inorganic Chemistry Communications* **2023,** *152*, 110700. DOI: 10.1016/j.inoche.2023.110700.

Suresh Kumar Reddy, K.; Kannan, P.; Al Shoaibi, A.; Srinivasakannan, C. KOH-based porous carbon from date palm seed: preparation, characterization, and application to phenol adsorption. *Water science and technology : a journal of the International Association on Water Pollution Research* **2014,** *70* (10), 1633–1640. DOI: 10.2166/wst.2014.419.

Tang, K.; Ma, H.; Tian, Y.; Liu, Z.; Jin, H.; Hou, S.; Zhou, K.; Tian, X. 3D printed hybrid-dimensional electrodes for flexible micro-supercapacitors with superior electrochemical behaviours. *Virtual and Physical Prototyping* **2020,** *15* (sup1), 511–519. DOI: 10.1080/17452759.2020.1842619.

Tang, Z.; Okano, T. Recent development of temperature-responsive surfaces and their application for cell sheet engineering. *Regenerative biomaterials* **2014,** *1* (1), 91–102. DOI: 10.1093/rb/rbu011.

Thakur, B. K.; Kumar, A.; Kumar, D. Green synthesis of titanium dioxide nanoparticles using Azadirachta indica leaf extract and evaluation of their antibacterial activity. *South African Journal of Botany* **2019,** *124*, 223–227. DOI: 10.1016/j.sajb.2019.05.024.

V T, T. S.; Chokkattu, J. J.; S, N.; Ramakrishnan, M.; Shanmugam, R. Green Synthesis of Titanium Oxide Nanoparticles With Rosemary and Ginger and Their Bactericidal Action Against Staphylococcus aureus. *Cureus* **2023,** *15* (9), e45892. DOI: 10.7759/cureus.45892.

Vandeginste, V. A Review of Fabrication Technologies for Carbon Electrode-Based Micro-Supercapacitors. *Applied Sciences* **2022,** *12* (2), 862. DOI: 10.3390/app12020862.

Wang, B.; Wang, J.-H.; Liu, Q.; Huang, H.; Chen, M.; Li, K.; Li, C.; Yu, X.-F.; Chu, P. K. Rose-bengal-conjugated gold nanorods for in vivo photodynamic and

photothermal oral cancer therapies. *Biomaterials* **2014,** *35* (6), 1954–1966. DOI: 10.1016/j.biomaterials.2013.11.066.

Wang, J.-H.; Wang, B.; Liu, Q.; Li, Q.; Huang, H.; Song, L.; Sun, T.-Y.; Wang, H.; Yu, X.-F.; Li, C.; Chu, P. K. Bimodal optical diagnostics of oral cancer based on Rose Bengal conjugated gold nanorod platform. *Biomaterials* **2013,** *34* (17), 4274–4283. DOI: 10.1016/j.biomaterials.2013.02.012.

Wu, K.; Kim, K.-W.; Kwon, J. H.; Kim, J. K.; Kim, S. H.; Moon, H. C. Direct ink writing of PEDOT:PSS inks for flexible micro-supercapacitors. *Journal of Industrial and Engineering Chemistry* **2023,** *123*, 272–277. DOI: 10.1016/j.jiec.2023.03.042.

Wu, X.; Wei, Y.; Lin, R.; Chen, P.; Hong, Z.; Zeng, R.; Xu, Q.; Li, T. Multi-responsive mesoporous polydopamine composite nanorods cooperate with nano-enzyme and photosensitiser for intensive immunotherapy of bladder cancer. *Immunology* **2022,** *167* (2), 247–262. DOI: 10.1111/imm.13534.

Xu, L.; Chen, Y.; Zhang, P.; Tang, J.; Xue, Y.; Luo, H.; Dai, R.; Jin, J.; Liu, J. 3D printed heterogeneous hybrid hydrogel scaffolds for sequential tumor photothermal-chemotherapy and wound healing. *Biomaterials science* **2022,** *10* (19), 5648–5661. DOI: 10.1039/d2bm00903j.

Xue, M.; Xie, Z.; Zhang, L.; Ma, X.; Wu, X.; Guo, Y.; Song, W.; Li, Z.; Cao, T. Microfluidic etching for fabrication of flexible and all-solid-state micro supercapacitor based on MnO2 nanoparticles. *Nanoscale* **2011,** *3* (7), 2703–2708. DOI: 10.1039/C0NR00990C.

Yan, X.; Tong, Y.; Wang, X.; Hou, F.; Liang, J. Extrusion-Based 3D-Printed Supercapacitors: Recent Progress and Challenges. *Energy & Environ Materials* **2022,** *5* (3), 800–822. DOI: 10.1002/eem2.12260.

Yao, M.; Gu, C.; Doyle, F. J.; Zhu, H.; Redmond, R. W.; Kochevar, I. E. Why is rose bengal more phototoxic to fibroblasts in vitro than in vivo? *Photochemistry and photobiology* **2014,** *90* (2), 297–305. DOI: 10.1111/php.12215.

Ying, S.; Guan, Z.; Ofoegbu, P. C.; Clubb, P.; Rico, C.; He, F.; Hong, J. Green synthesis of nanoparticles: Current developments and limitations. *Environmental Technology & Innovation* **2022,** *26*, 102336. DOI: 10.1016/j.eti.2022.102336.

Yontar, A. K.; Avcioğlu, S.; Çevik, S. Nature-based nanocomposites for adsorption and visible light photocatalytic degradation of methylene blue dye. *Journal of Cleaner Production* **2022,** *380*, 135070. DOI: 10.1016/j.jclepro.2022.135070.

Yu, C.; Schimelman, J.; Wang, P.; Miller, K. L.; Ma, X.; You, S.; Guan, J.; Sun, B.; Zhu, W.; Chen, S. Photopolymerizable Biomaterials and Light-Based 3D Printing Strategies for Biomedical Applications. *Chemical reviews* **2020,** *120* (19), 10695–10743. DOI: 10.1021/acs.chemrev.9b00810.

Yu, S.; Xia, G.; Yang, N.; Yuan, L.; Li, J.; Wang, Q.; Li, D.; Ding, L.; Fan, Z.; Li, J. Noble Metal Nanoparticle-Based Photothermal Therapy: Development and Application in Effective Cancer Therapy. *International journal of molecular sciences* **2024,** *25* (11). DOI: 10.3390/ijms25115632.

Zhang, M.; Lee, Y.; Zheng, Z.; Khan, M. T. A.; Lyu, X.; Byun, J.; Giessen, H.; Sitti, M. Micro- and nanofabrication of dynamic hydrogels with multichannel information. *Nature communications* **2023a,** *14* (1), 8208. DOI: 10.1038/s41467-023-43921-9.

Zhang, M.; Pal, A.; Lyu, X.; Wu, Y.; Sitti, M. Artificial-goosebump-driven microactuation. *Nature materials* **2024,** *23* (4), 560–569. DOI: 10.1038/s41563-024-01810-6.

Zhang, M.; Pal, A.; Zheng, Z.; Gardi, G.; Yildiz, E.; Sitti, M. Hydrogel muscles powering reconfigurable micro-metastructures with wide-spectrum programmability. *Nature materials* **2023b,** *22* (10), 1243–1252. DOI: 10.1038/s41563-023-01649-3.

Zhang, M.; Shahsavan, H.; Guo, Y.; Pena-Francesch, A.; Zhang, Y.; Sitti, M. Liquid-Crystal-Elastomer-Actuated Reconfigurable Microscale Kirigami Metastructures. *Advanced materials (Deerfield Beach, Fla.)* **2021,** *33* (25), e2008605. DOI: 10.1002/adma.202008605.

Zhang, M.; Sitti, M. Perspective on smart materials for empowering small-scale manipulation. *Science bulletin* **2024,** *69* (6), 718–721. DOI: 10.1016/j.scib.2024.01.017.

Zhang, Y.; Ji, T.; Hou, S.; Zhang, L.; Shi, Y.; Zhao, J.; Xu, X. All-printed solid-state substrate-versatile and high-performance micro-supercapacitors for in situ fabricated transferable and wearable energy storage via multi-material 3D printing. *Journal of Power Sources* **2018,** *403*, 109–117. DOI: 10.1016/j.jpowsour.2018.09.096.

Zhang, Y.; Peng, W.; Cao, Y.; Wang, W.; Teng, D.; Huang, Y.; Fan, G. 3D graphene-based active electrodes with large areal capacitance by modified direct ink writing method. *Colloids and Surfaces A: Physicochemical and Engineering Aspects* **2023c,** *671*, 131603. DOI: 10.1016/j.colsurfa.2023.131603.

Zhu, J.; Hu, W.; Ni, J.; Li, L. High areal energy zinc-ion micro-batteries enabled by 3D printing. *Journal of Materials Science & Technology* **2024,** *196*, 183–189. DOI: 10.1016/j.jmst.2024.01.053.